Technische Universität München

Physik Department

MPQ

Quantum Computing, Control & Communication

# Two-photon gateway and feedback control of a single atom in a cavity

**Alexander Kubanek**

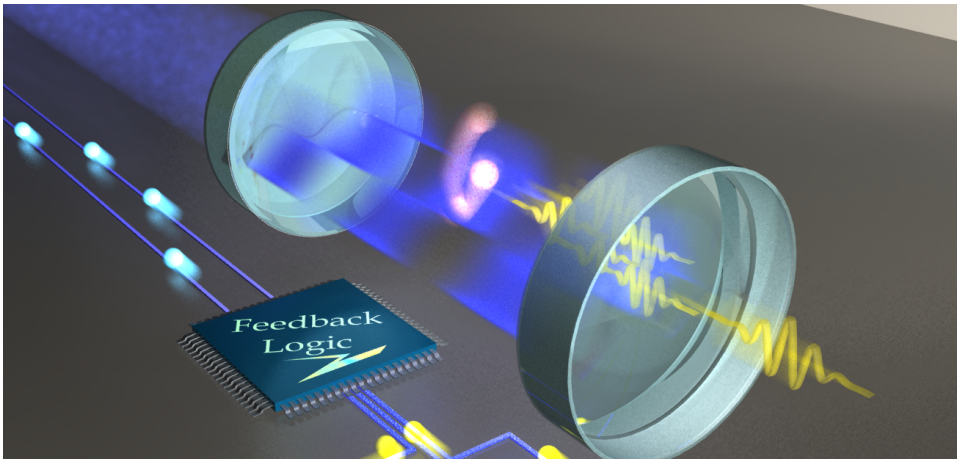


## Dissertation

Physik Department, Technische Universität München
and Max-Planck-Institut für Quantenoptik, Garching

October 2010

**Cover illustration:** On the title cover you can see an artist's view of the feedback loop that controls a single atom inside the cavity.

Technische Universität München
Max-Planck-Institut für Quantenoptik

# Two-photon gateway and feedback control of a single atom in a cavity

**Alexander Kubanek**

Vollständiger Abdruck der von der Fakultät für Physik
der Technischen Universität München
zur Erlangung des akademischen Grades eines

**Doktors der Naturwissenschaften (Dr. rer. nat.)**

genehmigten Dissertation.

| | | |
|---|---|---|
| Vorsitzender : | | Univ.-Prof. Dr. H. Friedrich |
| Prüfer der Dissertation : | 1. | Hon.-Prof. Dr. G. Rempe |
| | 2. | Univ.-Prof. Dr. P. Fierlinger |

Die Dissertation wurde am 30. 09. 2010
bei der Technischen Universität München eingereicht
und durch die Fakultät für Physik am 28. 10. 2010 angenommen.

# Abstract

This thesis reports on experiments with single atoms strongly coupled to a single mode of a high-finesse optical cavity. In the first part, it is shown that the motion of the atom in an intracavity dipole trap can be observed with high spatial and temporal resolution. Depending on the atom's current position, the dipole trap is switched to control the motion of the atom. The feedback acts in real time, faster than one oscillation period of the atom in the trap. In the second part the anharmonic energy level structure of the system is investigated. This anharmonicity allows one to selectively populate states containing two energy quanta in a two-photon process, resulting in a nonlinear response of the system with respect to the drive laser intensity. The photon statistics of the light transmitted through the cavity shows photon bunching and super-Poissonian fluctuations, indicating the transmission of photon pairs typical for a two-photon gateway.

# Zusammenfassung

Die vorliegende Arbeit berichtet von Experimenten mit einzelnen Atomen, die stark an die Mode eines optischen Resonators hoher Güte gekoppelt sind. Im ersten Teil wird gezeigt, wie die Bewegung des Atoms in der Dipolfalle mit hoher räumlicher und zeitlicher Auflösung beobachtet werden kann. Die Dipolfalle wird abhängig von der Position des Atoms geschaltet, um so die Bewegung zu kontrollieren. Die Rückkopplung agiert in Echtzeit, schneller als eine Oszillationsperiode des Atoms in der Falle. Im zweiten Teil wird die anharmonische Struktur der Energiezustände des Systems untersucht. Diese Anharmonizität erlaubt es Zustände, die zwei Energiequanten enthalten, selektiv in einem Zwei-Photonen Prozess anzuregen, was zu einer nicht-linearen Antwort des Systems bezüglich der treibenden Laserintensität führt. Die Photonstatistik des transmittierten Lichtes zeigt Photonbunching und super-Poissonische Fluktuationen, was eine Transmission von Photonenpaaren nahelegt und typisch für ein Zwei-Photonen Gateway ist.

# Contents

# 1 Introduction

At the beginning of the twentieth century quantum mechanics was born. When Max Planck described black-body radiation with a quantized energy transfer between matter and an electromagnetic field [Pla01], he intended to bridge the gap between two of the most important theories of the nineteenth century, namely electrodynamics and thermodynamics. However, his description opened a completely new field, the quantum theory, with the Planck constant as a new natural constant connecting energy and frequency. A few years later, Einstein finally started one of the biggest revolutions in physics with his interpretation of the photoelectric effect [Ein05]. Famous scientists like Feynman, Dirac, Pauli, Heisenberg, and Fermi developed the quantum theory describing matter-light interactions. Since then, the study of the interaction of light and matter has developed into an exciting research field, known as quantum electrodynamics (QED). Early experiments, like the measurement of the Lamb shift for the hydrogen atom [Lam47], confirmed the predictions of QED already in the 1950th. The beauty of the quantum theory arises, among other things, from its mathematical results explaining experiments with high accuracy that can not be explained with a classical theory. However, skepticism about the usefulness of quantum theory for describing single particles still remained. For example, Schrödinger doubted that it might ever be possible to do experiments with single particles. In [Sch52] he wrote: "In the first place it is fair to state that we are not *experimenting* with single particles, any more than we can raise Ichthyosauria in the zoo".
About half a century later we are still not able to raise Ichthyosauria in the zoo, but fortunately, the skepticism about experiments with single particles was unjustified. Today, experiments that were initially conceived as thought experiments are actually realized in the laboratory. As in a text book model, this thesis reports on a system where a single atom is strongly coupled to a single mode of the electromagnetic field. The light field can be considered as a single mode when it is confined by a high-finesse optical cavity (see [Vah03] for an overview of different cavity systems). This field, known as cavity QED, is ideal for the investigation of matter-light interactions.
Cavity QED experiments demonstrate remarkable properties for the observation of neutral atoms. The most natural way to determine the position of an atom is light scattering. In free space the photon flux for the observation of a single atom by light scattering is limited by the natural decay rate of the excited state and by photon emission in random directions. The rate of spon-

taneous emission into the cavity mode is enhanced by the Purcell effect [Pur46] and all the information about the atom is channeled into one mode of light. The exceptional observation properties have been used not only to detect single atoms in a very sensitive way [Hoo98, Mün99a] but also to continuously track the atomic motion inside the cavity mode [Pin00, Hoo00]. In combination with optical dipole traps [Gri99] cavity QED systems have been used to trap atoms inside the cavity mode [Ye99, McK03] with so-called intracavity dipole traps. In this thesis a new type of intracavity dipole trap is used. In contrast to a far red-detuned trap where the atom is trapped at maximum light intensity, it is confined to the dark trap center of a far blue-detuned trap [Pup07a]. In principle, it allows for the preservation of the free space properties of the atom while it is trapped.

A prerequisite for the observation and trapping of a single atom is a sufficiently slow velocity of the atom. While atoms at room temperature move with a velocity of typically a few hundred m/s, a number of different cooling techniques have been developed to reduce the velocity of the atoms. The most important invention for the advancement in the cooling of particles was the laser which celebrates its 50th anniversary this year [Mai60]. The development of the laser resulted in the invention of laser cooling [Hän75, Chu98, CT98, Phi98]. Transferred to cavity QED systems, the development of cavity cooling [Mau04] and the cooling to the ground state of motion by resolved sideband cooling [Boo06] demonstrated the remarkable control possibilities of an atom inside a cavity mode. However, these experiments cooled the atomic motion only in the direction along the cavity axis. Three-dimensional cavity cooling was demonstrated in [Nus05] and relies on an orthogonal arrangement of cavity and cooling lasers. One main focus of this work is the implementation of a new cooling technique that achieves three-dimensional control of the atom with a one-dimensional alignment of cavity and cooling laser. Furthermore, the atom is not only cooled but its trajectory can be controlled. The principle of the control mechanism is a closed feedback loop. Before describing the details of the experiment a review of feedback should motivate for the work. The overview starts in a broad context and ends with the specific implementation of feedback control of a single neutral atom.

In general, feedback is a powerful technique to control classical systems. Engineers have developed feedback concepts in a wide range of different fields. Just to mention one example, the rapid development of electrical circuits in the early 20th century profited a lot from the principle to feed an output signal back into the input, e.g., to develop high quality signal amplifiers.

Besides the enormous use of feedback applications it is a fascinating tool for scientists. The Nobel prize in physics in 1984 was awarded to Carlo Rubbia and Simon van der Meer for their contributions leading to the discovery of the elementary particles, W and Z bosons, which mediate the weak interaction. In particular they invented stochastic cooling for the experiments at CERN

[vdM85]. In order to increase phase-space density, a sensor acquires electrical signals from the particles (protons or antiprotons). The amplified signal is used at a later position in the storage ring to influence the particles. A so-called kicker is excited by the amplified pick-up signals and pushes the particles at the right time. A prerequisite is a good knowledge about the individual particle's position in phase-space.
The adaptability of feedback to a single quantum emitter is complicated by the limited rate of information about its position. In the work of [Bus06], a single trapped ion in front of a mirror is controlled via feedback. Here, the fact that the ion in a Paul trap is a high Q oscillator with constant oscillation properties (like the oscillation frequency) over a long time allows to compensate the limited signal in the observation process by a longer measurement time. To cool the ion a voltage is applied to the trap electrodes that is modulated according to the ion's oscillation frequency and with the right phase.
Feedback control is even more challenging for a single neutral atom. Here, the trapping potentials are typically much shallower than in an ion trap. The atom oscillates in the potential and is sensitive to forces with random character, like spontaneous absorption and emission of near-resonant photons or fluctuations of the trapping potential. The atomic motion becomes unpredictable on timescales as short as its oscillation period. This requires rapid measurements that, in combination with a limited rate of information, causes a vanishingly small signal. However, in cavity QED measurements are faster and more sensitive than in free space as a result of the increased rate of information exchange between the atom and the observed cavity field. This closes the loop of the overview of feedback and brings us back to the work of this thesis. With the atom coupled to the cavity field its motion can be monitored with high spatial and temporal resolution and its trajectory can be controlled by applying a force on the atom that depends on the outcome of the observation of its position [Kub09].
The advances in the control of the external degrees of freedom improve the possibilities to investigate the internal degrees of freedom of the strongly coupled system. The external dynamics typically influence the internal ones. For example, the motion of the atom inside the cavity mode changes the atom-field coupling strength. With a reasonably good control the internal degrees of freedom can be investigated, while the external degrees of freedom can, to a large extent, be decoupled. One cornerstone of experiments in cavity QED is the possibility of reaching the strong-coupling regime [Ber94]. Here, the atom-field coupling strength exceeds dissipative processes, in particular the coupling to the environment. This regime is characterized by a coherent exchange of energy between the atom and the light mode. The level structure of the energy eigenstates of the strongly-coupled system is described in the work of Jaynes and Cummings [Jay63]. While the eigenstates of a single mode of light form a harmonic energy ladder, the coupling of a two-level atom to the light field

leads to a splitting of each state (except the ground state) into a doublet. The splitting is proportional to the coupling strength and the square root of number of excitations in the system, where the square-root dependence results in an anharmonic energy ladder, known as Jaynes-Cummings ladder. The rate at which energy is exchanged between the atom and the field is determined by the level splitting. When the system contains one excitation the splitting is known as vacuum Rabi splitting or normal mode splitting .

The first experiments in the strong-coupling regime were done in the microwave domain with transient Rydberg atoms [Mes85]. Here, the cavities are made out of superconducting material and are operated at cryogenic temperatures, reaching field decay times as long as 100 ms. When the cavity is resonant with the atom, the field induces Rabi oscillations between the coupled levels of the atom (see [Rai01, Wal06] for an overview). The eigenstates of the coupled system were first observed via these Rabi oscillations in [Rem87, Bru96]. When the atom and cavity are far-detuned, the cavity field can be probed using transient Rydberg atoms. For example, non-demolition measurements of Fock states in the cavity have been demonstrated [Nog99, Gle07, Gue07].

Strong-coupling cavity QED in the optical domain forms a complementary system. While in the microwave domain photons can be trapped up to a tenth of a second inside the cavity, and atoms are used to provide information about the cavity field, in the optical domain it is the field escaping the cavity which reveals the evolution of the coupled system. Here, the timescales are much faster than in the microwave domain. For example, the field decay rate of optical cavities is on the order of megahertz. It is the optical domain where good single-photon detectors are available. The photons emitted from the cavity can be used to observe the conditioned evolution of such an open quantum system. In the optical domain the vacuum Rabi splitting was first observed with thermal atoms where the number of coupled atoms fluctuated around 1 [Zhu90, Tho92], and for many atoms [Chi96, Gri97]. Later the normal modes were measured with single trapped atoms [Boc04, Mau05b].

The higher-lying doublets of the eigenenergies of the strongly coupled system, the so-called higher-order "dressed states", were spectroscopically observed recently [Sch08c]. They cannot be explained by a classical or semiclassical theory but require a quantum mechanical treatment. The higher-order dressed states are of particular interest in this work. Part of this thesis discusses how to excite one of the dressed states via a two-photon transition demonstrating the anharmonic splitting of the eigenstates of a strongly coupled system. The multi-photon nature of these transitions causes a nonlinear intensity response on the single-atom two-photon level.

Photon correlations give additional insights into the internal dynamics of the coupled atom-cavity system. For example, the excitation of the normal modes is characterized by photon antibunching. Here, only single photons can excite the system, while multiple photons are blocked due to the anharmonic energy

level structure, known as photon blockade [Bir05]. Exciting a two-photon resonance leads to a complementary behavior. The coupled atom-cavity system preferentially transmits photons in pairs while single photons are blocked and acts as a two-photon gateway [Kub08].

This thesis is organized as follows. First, theoretical and technical basics of the coupled atom-cavity system are introduced. **Chapter 2** summarizes the relevant theoretical concepts of cavity QED. A fixed-atom theory using the master equation approach describes the system, and motional effects are included, e.g., by Monte Carlo simulations. Additional theory is provided in each chapter when needed. **Chapter 3** describes the experimental setup with the focus on new parts of the setup which are not yet presented in former theses.
Then, the control of external degrees of freedom is discussed. **Chapter 4** characterizes the motion of a single atom and explains how to control and influence it. The knowledge of the atomic motion is then used in **Chap. 5** to control the atom's trajectory via a feedback loop. The short coherence time of the atomic oscillation imposes high demands on the feedback, requiring a fast reaction time within a fraction of one atomic oscillation period.
Afterwards, the thesis concentrates on internal degrees of freedom of the coupled system. **Chapter 6** studies the excitation of a two-photon resonance. When the two-photon resonance is exclusively excited while avoiding the normal modes, the intensity response of the system shows a quantum nonlinearity. Detailed insights into the evolution of the state populations are obtained in **Chap. 7** using an analytical description of the coupled system in a four level model. The results are compared with the experiment via second-order intensity correlations. The two-photon resonance is used to manipulate photon statistics where the coupled system preferentially transmits photons in pairs. The enhanced rate of photon pairs is manifested in photon bunching and super-Poissonian light statistics. The multi-photon nature of the strongly coupled system is directly demonstrated by the results of transmission spectroscopy and photon-photon correlations.
Each main chapter has an introductory part and a summary or outlook section. A brief summary of the whole work is given in **Chap. 8** comparing the results with other systems and with a short outlook to potential applications.

# 2 Theory of a single atom coupled to a single mode of light

This chapter theoretically introduces cavity QED with single atoms. It starts with the description of a single mode of light in Sec. 2.1 and a single two-level atom in Sec. 2.2. The interaction between the light mode and the atom is described by the Jaynes-Cummings Hamiltonian in Sec. 2.3. The description of the closed atom-cavity system is then extended to an open system approach. The coupling to the environment allows us to do spectroscopy on the system. Motional effects are taken into account, e.g., by Monte-Carlo simulations at the end of this section. Section 2.4 treats theoretical aspects of two methods to access observables in the experiment, namely photon counting and photon-photon correlations. Beyond this introduction here, some later chapters provide additional specific theory.

## 2.1 Single mode of light

Quantizing the electromagnetic field requires the quantum mechanics of a harmonic oscillator. Let us constrain the electromagnetic field to a single mode of light by a cavity, simplifying the Hamiltonian of the light field to

$$\hat{H}_c = \hbar\omega_c(\hat{a}^\dagger\hat{a} + \frac{1}{2})\,, \tag{2.1}$$

where $\omega_c$ is the resonance frequency of the cavity. The creation and annihilation operators, as well as their commutation relations, are used to obtain predictions about the system. They satisfy

$$\hat{a}^\dagger|n\rangle = \sqrt{n+1}|n+1\rangle \tag{2.2}$$

and

$$\hat{a}|n\rangle = \sqrt{n}|n-1\rangle. \tag{2.3}$$

In the Fock-state basis $|n\rangle, n = 0, 1, 2, ...$ the eigenvalues are

$$\hat{N}|n\rangle \equiv (\hat{a}^\dagger\hat{a})|n\rangle = n|n\rangle\,, \tag{2.4}$$

with the photon number $n$. The eigenstates of this Hamiltonian form a ladder with equally spaced eigenenergies

$$E_n = (n + \frac{1}{2})\hbar\omega_c, \;\; n = 0, 1, 2, ... \tag{2.5}$$

Setting the ground state energy to zero we are left with

$$\hat{H}_c = \hbar\omega_c \hat{a}^\dagger \hat{a} \,. \tag{2.6}$$

## 2.2 Single two-level atom

We consider a two-level atom that can either be in the ground state $|g\rangle$ with energy $E_g$ or in the excited state $|e\rangle$ with energy $E_e$. Here, the atomic Hamiltonian reads

$$\hat{H}_a \;=\; E_g|g\rangle\langle g| + E_e|e\rangle\langle e| \,. \tag{2.7}$$

With the zero energy at $E_g$, Eq. (2.7) can be written as

$$\hat{H}_a \;=\; \hbar\omega_a \hat{\sigma}_+ \hat{\sigma}_- \,. \tag{2.8}$$

Here, $\omega_a$ is the atomic resonance frequency and the corresponding lowering and raising operators are

$$\hat{\sigma}_-|e\rangle = |g\rangle,\; \hat{\sigma}_+|g\rangle = |e\rangle \,. \tag{2.9}$$

## 2.3 Coupled atom-cavity system

### 2.3.1 Closed quantum system

When the electromagnetic interaction between a single atom and a single mode of light is strong enough, the atom-light system forms a new quantum system with a structure that is different from the sum of its parts. The new Hamiltonian includes an interaction term

$$\hat{H}_i = i\hbar g(\hat{a}^\dagger \hat{\sigma}_- - \hat{\sigma}_+ \hat{a}) \,, \tag{2.10}$$

describing the reversible exchange of excitation between the atom and the light mode. Here we have used the dipole approximation, assuming a constant amplitude of the field across the dimension of the atom, and the rotating-wave approximation neglecting terms of the form $\hat{\sigma}_-\hat{a}$ and $\hat{\sigma}_+\hat{a}^\dagger$. The coupling strength, $g$, between atom and light field is given by

$$g = \sqrt{\frac{\omega_c}{2\hbar\epsilon_0 V}} d_{ge} \,, \tag{2.11}$$

with the mode volume $V \approx \pi w_0^2 L/4$ where $L$ is the cavity length and $w_0$ is the beam waist which is assumed to be constant over $L$. The dipole matrix element $d_{ge}$ describes the transition strength between $|g\rangle$ and $|e\rangle$ and $\epsilon_0$ is the vacuum permittivity. The total Hamiltonian describing the coupled system is

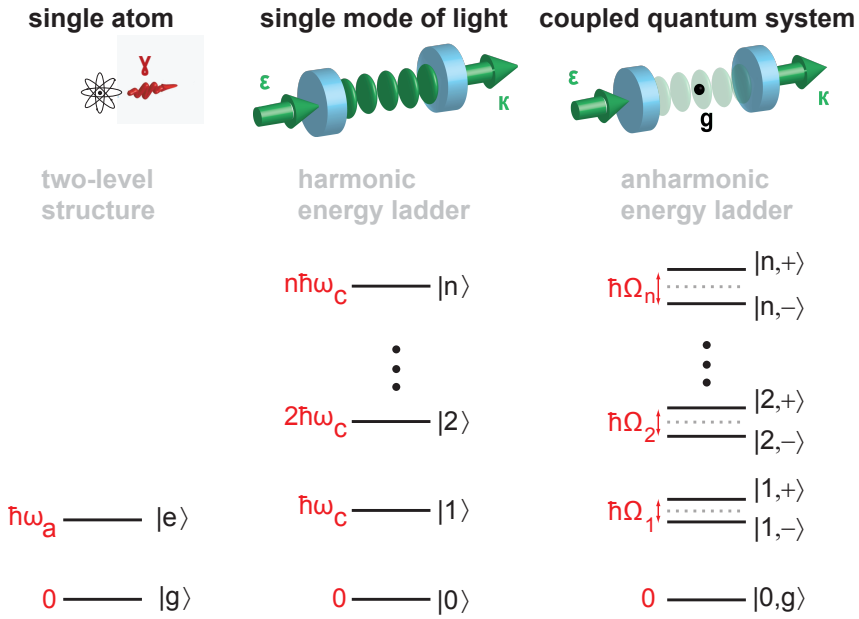


**Figure 2.1:** Jaynes-Cummings model of the strongly-coupled atom-cavity system. The model describes the interaction of a single two-level atom with a single mode of light. The eigenstates change from a harmonic energy ladder for the empty cavity to an anharmonic one where each state, except the ground state, is split into a doublet. The system's decay rates, $\kappa$ and $\gamma$, are not included in the Jaynes-Cummings model but are introduced in the open system approach.

$$\hat{H}_{JC} = \hat{H}_a + \hat{H}_c + \hat{H}_i \tag{2.12}$$

and is given by

$$\hat{H}_{JC}/\hbar = \omega_a \hat{\sigma}_+ \hat{\sigma}_- + \omega_c \hat{a}^\dagger \hat{a} + ig(\hat{a}^\dagger \hat{\sigma}_- - \hat{\sigma}_+ \hat{a}) \, . \tag{2.13}$$

The corresponding model is known as Jaynes-Cummings model [Jay63]. The new eigenstates of the coupled system, called dressed states, can be written as linear combinations of the bare states

$$|n,+\rangle = \sin\Theta_n |g,n\rangle + \cos\Theta_n |e,n-1\rangle \tag{2.14}$$

and

$$|n,-\rangle = \cos\Theta_n |g,n\rangle - \sin\Theta_n |e,n-1\rangle \tag{2.15}$$

where $n = 1, 2, 3...$ is the number of excitations in the system. The Hamiltonian $\hat{H}_{JC}$ only couples $|n,g\rangle$ with $|n-1,e\rangle$. The mixing angle $\Theta_n$ is given by

$$\sin\Theta_n = \frac{2g\sqrt{n}}{\sqrt{(\Omega_n - \Delta_{ac})^2 + 4g^2 n}} \tag{2.16}$$

and

$$\cos\Theta_n = \frac{\Omega_n - \Delta_{ac}}{\sqrt{(\Omega_n - \Delta_{ac})^2 + 4g^2 n}} \tag{2.17}$$

with the generalized Rabi frequency $\Omega_n = \sqrt{\Delta_{ac}^2 + 4g^2 n}$. The formalism allows for a frequency difference between $\omega_a$ and $\omega_c$, denoted as $\Delta_{ac} = \omega_a - \omega_c$. For a two-state atom coupled to an optical mode with successive photon number states, $|0\rangle$, $|1\rangle$, $|2\rangle$ ..., the quantum spectrum consists of a ground state, $|g, 0\rangle$, and a discrete ladder of pairs of the dressed states, $|1, \pm\rangle$, $|2, \pm\rangle$, as is depicted in Fig. 2.1. The anharmonic ladder of the eigenenergies is defined by

$$E_{n,\pm}/\hbar \;=\; n\omega_c \pm \frac{1}{2}\Omega_n \;. \tag{2.18}$$

Here the ground state energy $E_0$ is set to zero. Each state, except $E_0$, of the harmonic ladder of the bare cavity splits into a doublet with a energy difference of $\hbar\Omega_n$.

### 2.3.2 Open quantum system

The system also couples to the environment allowing for an observation of the system. The environment is coupled via the cavity field decay rate $\kappa$ and the atomic polarization decay rate $\gamma$. Both mechanisms enter as losses in the theory. The regime of strong coupling is achieved when the coupling strength, $g$, exceeds all losses. In our case this corresponds to

$$g \;>\; \gamma, \kappa \;. \tag{2.19}$$

A continuous driving of the cavity field leads to a balancing of creation and loss of the excitation. The driving term with amplitude $\varepsilon$ is accounted for in the Hamiltonian

$$\hat{H}/\hbar \;=\; \hat{H}_{JC}/\hbar + \varepsilon(\hat{a}^\dagger e^{-i\omega_l t} + \hat{a}e^{i\omega_l t}) \;, \tag{2.20}$$

where $\omega_l$ is the oscillation frequency of the driving field. By going into the rotating-wave approximation (RWA) in the interaction picture with respect to $\omega_l$, one obtains the time-independent Hamiltonian

$$\begin{aligned} \hat{H}'/\hbar &= \hat{H}'_{JC}/\hbar + \varepsilon(\hat{a}^\dagger + \hat{a}) \\ &= (\omega_a - \omega_l)\hat{\sigma}_+\hat{\sigma}_- + (\omega_c - \omega_l)\hat{a}^\dagger\hat{a} + ig(\hat{a}^\dagger\hat{\sigma}_- - \hat{\sigma}_+\hat{a}) + \varepsilon(\hat{a}^\dagger + \hat{a}) \;. \end{aligned} \tag{2.21}$$

In the following we define the atom- and cavity-detuning with respect to the driving frequency as

$$\Delta_a \;\equiv\; (\omega_l - \omega_a), \;\; \text{and} \;\; \Delta_c \;\equiv\; (\omega_l - \omega_c). \tag{2.22}$$

The driving field and the decay of the system leads to a perturbation, where the eigenstates deviate from the results of the Jaynes-Cummings model. The level shift $\Delta$ results from all dipole-coupled states and can be included in perturbation theory [Als92, Bri93].

Experiments carried out in this work are compared with the numerical solution of Eq. (2.21). For a realistic comparison the theory needs to account for attributes of the experiment. For example, the driving field strength is adjusted to imperfections in the coupling into the cavity as well as absorption in the mirrors.
There are a number of different approaches to describe the time dependence of an open system [Car93, Har06]. In this thesis we use the master equation approach describing the time evolution of the density matrix, $\rho$, with a coupling to the environment [Car99]. The general master equation reads

$$\begin{aligned}\frac{d\rho}{dt} &= \frac{1}{i\hbar}\{[H'_{JC} - i\hbar\Gamma, \rho] + \hbar\varepsilon[a + a^\dagger, \rho]\} \\ &\quad + 2\kappa a\rho a^\dagger + 2\gamma\sigma_-\rho\sigma_+.\end{aligned} \tag{2.23}$$

Here $[\Gamma, \rho]$ corresponds to $\kappa(a^\dagger a\rho+\rho a^\dagger a)+\gamma(\sigma_+\sigma_-\rho+\rho\sigma_+\sigma_-)$. In the Schrödinger equation $H'_{JC}$ becomes the energy part and $-\frac{i}{2}\Gamma$ the damping part, while the second line describes quantum jumps.
The master equation can be used, e.g., to derive the derivative of the expectation value of the intracavity photon number. In the absence of driving $\varepsilon = 0$ and for $g = 0$

$$\frac{d}{dt}\langle a^\dagger a\rangle \;=\; -2\kappa\langle a^\dagger a\rangle \tag{2.24}$$

mirrors the decay behavior of the cavity field intensity.

### 2.3.3 Position dependent theory

So far the theory assumes a fixed atom-field coupling strength. However, the light mode has a spatial field distribution $\psi(x, r)$ which is defined by the cavity. For example, the mode function of a $\mathrm{TEM}_{00}$-mode is given by $\psi(r, z) = \cos(kz)\exp(-r^2/\omega_0^2)$, with the mode waist $w_0$. Therefore, the coupling strength depends on the position of the atom relative to the field mode in the radial, $r$, and the axial, $z$, directions via

$$g = g_{max}\psi(r, z)\ . \tag{2.25}$$

The intracavity photon number and the transmitted light depends on the coupling strength and thus on the atomic position. To illustrate this influence of the atomic localization we use a classical model [Sch08b] to get the expectation value of the steady-state, intracavity photon number. From solving Heisenberg's equation of motion we obtain

$$\langle a^\dagger a\rangle_{ss} \;=\; \frac{\varepsilon^2}{\Delta_c^2 + \kappa^2}\frac{1}{|1 - \nu|^2}\,, \tag{2.26}$$

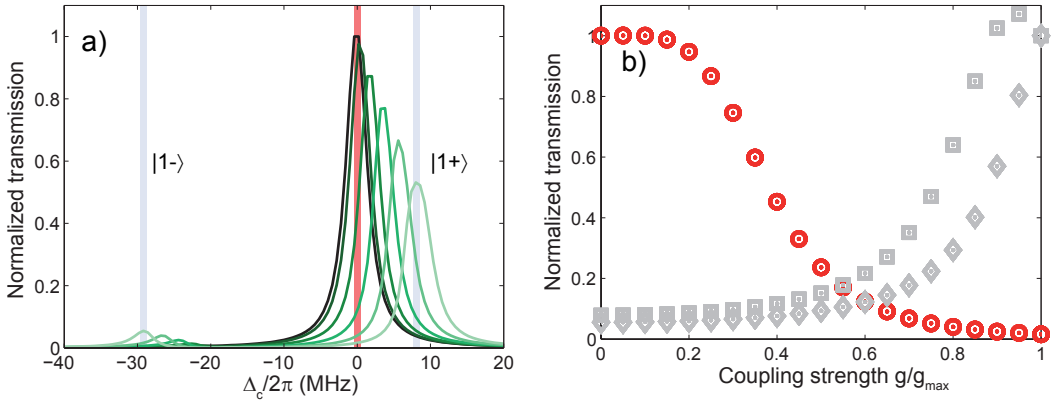


**Figure 2.2:** Position dependent transmission. a) Calculated transmission versus laser-cavity detuning $\Delta_c$ with $\Delta_a = 20$ MHz. The best contrast between a well coupled atom (light green line for $g/g_{max} = 1$) and a badly coupled atom (black line for $g/g_{max} = 0$) is achieved on resonance with the empty cavity, i.e. $\Delta_c = 0$, red area. A good contrast can also be realized on resonance with the normal modes (grey areas). b) Normalized transmission for the three possible observation regions with high contrast as a function of the coupling strength. On resonance with the empty cavity (red circles) the transmission drops when $g/g_{max}$ is increased from 0 to 1, with the best contrast obtained for $0.2 < g/g_{max} < 0.6$. When measuring on the normal-mode frequencies (grey squares for $|1,+\rangle$, grey diamonds for $|1,-\rangle$) the best contrast is achieved above 0.6.

with $\nu = g^2/[(\Delta_a + i\gamma)(\Delta_c + i\kappa)]$. For resonant probing, $\Delta_a = \Delta_c = 0$, and with weak driving the presence of an atom changes the transmitted photon flux corresponding to

$$\frac{I}{I_0} = \frac{1}{(1+2C_1)^2} \approx \frac{1}{4C_1^2}\,, \tag{2.27}$$

where $C_1 = g^2/(2\gamma\kappa) > 1$ is the cooperativity parameter and $I$ and $I_0$ is the photon flux with and without an atom present. Figure 2.2 illustrates the transmission spectrum for different coupling strengths, $g$. The probe laser is detuned from the Stark-shifted atomic resonance by $\Delta_a/2\pi = 20$ MHz matching the experiments performed in Chap. 4 and Chap. 5. The black curve corresponds to $g = 0$ while for the other curves the coupling strength is increased in steps of $0.2\,g_{max}$ up to a maximum coupling strength of $g_{max}/2\pi = 16$ MHz (light green line). The transmission spectrum shows a single Lorentzian-shaped resonance for $g = 0$, the empty cavity resonance. When $g$ is increased, two transmission lines appear, the so-called normal modes. The asymmetry of the spectrum arises from the atom-cavity detuning. It is straightforward to identify three frequency regions where the presence of an atom causes a large change in the transmission. One is to have the frequency of the probe laser on resonance with the empty cavity (red region). The other two are to have the laser on

resonance with one of the normal modes (two grey regions). The largest contrast is found on resonance with the empty cavity.
For an atom moving inside the cavity mode this means that the coupling strength $g$ is modulated. In the discussed regions a moving atom imprints its motion on the transmitted photon flux. The overall transmission is the highest on resonance with the empty cavity. An atom which attempts to leave the cavity increases the transmission by a factor of 70 when $g$ changes from $g_{max}$ to 0. In contrast, on resonance with the normal modes the transmission increases with increasing coupling strength by a factor of 18 on the lower-frequency normal mode (state $|1,-\rangle$ at a detuning of $\Delta_c/2\pi = -29$ MHz) and 14 on the higher-frequency normal mode (state $|1,+\rangle$ at a detuning of $\Delta_c/2\pi = 8$ MHz). For pump frequencies between the normal modes but away from the empty cavity resonance, the transmission signal is a non-monotonic function of the coupling strength and therefore not appropriate for observing the atomic motion.
To further analyze the two possible frequency regions for monitoring the atomic motion, the relative transmission is plotted as a function of $g/g_{max}$ in Fig. 2.2 b). On resonance with the empty cavity the best sensitivity is obtained for $0.2 < g/g_{max} < 0.6$, while the transmission is only marginally sensitive to changes of $g$ when the atom is very well localized. On resonance with the normal modes (grey squares and diamonds correspond to transitions to $|1,+\rangle$ and $|1,-\rangle$, respectively) the best contrast is achieved for $g/g_{max} > 0.6$. For these parameters the photon flux is more sensitive to well coupled atoms.
In the theory the fluctuation of the coupling strength, $g$, due to the atomic motion is considered by two methods.
1. A Gaussian probability distribution for the values of $g$ is included in the theory.
2. For a more detailed comparison between theory and experiment the motional dynamics of the system are modeled in numerical simulations. In the past, such simulations have shown very good agreement with the experiment where the spectrum of the coupled system was measured. Especially these measurements are sensitive to the (time-averaged) position of the atom in the cavity mode [Mau05b, Sch08c]. The simulations take into account the conservative trapping potential as well as free-space and cavity-induced dissipative forces, momentum diffusion and parametric heating due to intensity fluctuations of the dipole trap. For a detailed description of the Monte-Carlo simulations see ([Sch08b, Fuh08]).

## 2.4 Observation and characterization

In this work we observe the spectrum of an optical cavity QED system by counting photons transmitting the strongly coupled system. Information about

photon statistics is obtained by calculating second-order photon correlations. Both methods are explained in the following.

### 2.4.1 Photon counting

Experiments in the optical domain profit from the fact that detectors exist that count single photons. The physical process involved is the photoelectric effect transforming the incoming light energy into an electric signal. The intensity is obtained by recording the number of photoelectrons $n_{pe}$ produced in a counting time $t$ and converting it into the average transmitted intensity $I$ via

$$I = \frac{n_{pe}}{\eta t}\hbar\omega\,. \tag{2.28}$$

Here $\eta$ is the quantum efficiency of the detection setup. The obtained result is simply the mean value of the photon counting probability distribution.

### 2.4.2 Photon-photon correlations

For a coherent laser beam with constant intensity the photon statistics follows a Poissonian distribution. Deviations from a Poisson distribution of a given light field can be quantified by calculating the intensity correlation functions. In this thesis we concentrate on second-order intensity correlations. The normalized second-order correlation function is defined by

$$g^{(2)}(\tau) = \frac{\langle I(t)I(t+\tau)\rangle}{\langle I(t)\rangle^2} \tag{2.29}$$

or in terms of the photon annihilation and creation operators

$$g^{(2)}(\tau) = \frac{\langle \hat{a}^\dagger(t)\hat{a}^\dagger(t+\tau)\hat{a}(t+\tau)\hat{a}(t)\rangle}{\langle \hat{a}^\dagger(t)\hat{a}(t)\rangle^2} \tag{2.30}$$

When the system is excited with a weak driving field, $g^{(2)}(\tau)$ of the transmitted light has been shown to be independent of the laser intensity [Car91], [Bre99], [Got04]. For zero time delay, a Poissonian light statistics shows $g^{(2)}(0) = 1$. If the intensity fluctuations are broader than a Poissonian distribution, $g^{(2)}(0) > 1$, they are called super-Poissonian. If $g^{(2)}(0) < 1$, the light is called sub-Poissonian. For example thermal light shows $g^{(2)}(0) = 2$. Here, the photons tend to arrive on the detector in "bunches". Therefore, a photon emission characterized by $g^{(2)}(0) > g^{(2)}(\tau)$ is called bunched. When $g^{(2)}(0) < g^{(2)}(\tau)$, the light field is called antibunched. Antibunching was first observed in [Kim77] and can not be explained with light described as a classical electromagnetic wave. Instead it requires a quantization of the electromagnetic field. Second-order photon correlations are used to characterize single-photon

sources as they should show perfect antibunching and sub-Poissonian statistics [Gra04, Bir05, MO05, Hij07]. Lasing properties are also characterized by intensity correlations. A laser device undergoes a transition from a thermal light source with bunched light and a $g^{(2)}(0) = 2$ to coherent light, $g^{(2)}(0) = 1$, when the device starts lasing ([Ass09]).
Despite the importance of photon bunching and antibunching for the definition of different coherent and incoherent light sources, there exist a number of different definitions in the literature. Sometimes photon bunching is defined as $g^{(2)}(0) > g^{(2)}(\tau)$, where $(\tau) \to \infty$. When $g^{(2)}(\infty) = 1$ this definition is equivalent to super-Poissonian light statistics. A very restrictive definition is $g^{(2)}(0) > g^{(2)}(\tau)$ for all $(\tau)$. Here, we define photon bunching by $g^{(2)}(0) > g^{(2)}(0+)$, a correlation function which is initially decreasing. Similarly, antibunching corresponds to an initially increasing correlation function $g^{(2)}(0) < g^{(2)}(0+)$. Quantum mechanics allows for $g^{(2)}(0) > 1$ and, at the same time, $g^{(2)}(0) < g^{(2)}(0+)$. Such a rising correlation function corresponds to antibunching and super-Poissonian statistics. Alternatively, bunching could occur for sub-Poissonian light when $g^{(2)}(0) < 1$, as long as $g^{(2)}(0) > g^{(2)}(0+)$. The field of cavity QED requires an especially careful choice as here nonclassical features and dynamics of the atom-field interaction are revealed in second-order photon correlations [Rem91, Fos00a].

# 3 Technical realization of the experiment

This chapter describes the experimental setup which allows for the study of the interaction of a single mode of light with a single two level atom. After a brief overview of the experiment, Sec. 3.1 focusses on the description of those parts of the experiment which are of direct importance for this thesis. A more detailed description of other parts can be found in [Mau05a, Pup07b].
Section 3.2 explores two experimental possibilities to obtain information about the coupled system, namely photon counting (Sec. 3.2.1) and photon-photon correlations (Sec. 3.2.2). Section 3.3 focuses on the technical realization of controlling the coupled system in real time.

## 3.1 Preparation of a strongly-coupled atom-cavity system

A sketch of the setup is shown in Fig. 3.1. We capture and cool Rubidium 85 atoms (Sec. 3.1.1) in a magneto-optical trap (MOT) and inject them via an atomic fountain (Sec. 3.1.2) into the optical resonator (Sec. 3.1.3). Five different lasers are coupled into the cavity in order to observe and hold the atom inside the cavity (Sec. 3.1.4). The light transmitted through the atom-cavity system is detected (Sec. 3.1.5). To study the interaction between the single atom and a single mode of the cavity we probe the system with a light beam at 780 nm, close to the $D_2$-line of Rubidium, called the probe beam. After launching the atoms from the atomic fountain towards the cavity they are guided by different guiding modes into the region of strong coupling with the probe beam (Sec. 3.1.6). The presence of an atom in the cavity is detected by a sudden change in the probe beam transmission (Sec. 3.1.7). Then, a trigger is activated switching the intracavity modes from a guiding configuration to a trapping configuration. The trapping potential is created using three different laser beams (Sec. 3.1.8). With different measurement sequences we investigate the coupled atom-cavity system (Sec. 3.1.9). The influence of intense intracavity light on the resonance frequencies of the cavity is studied in Sec. 3.1.10.

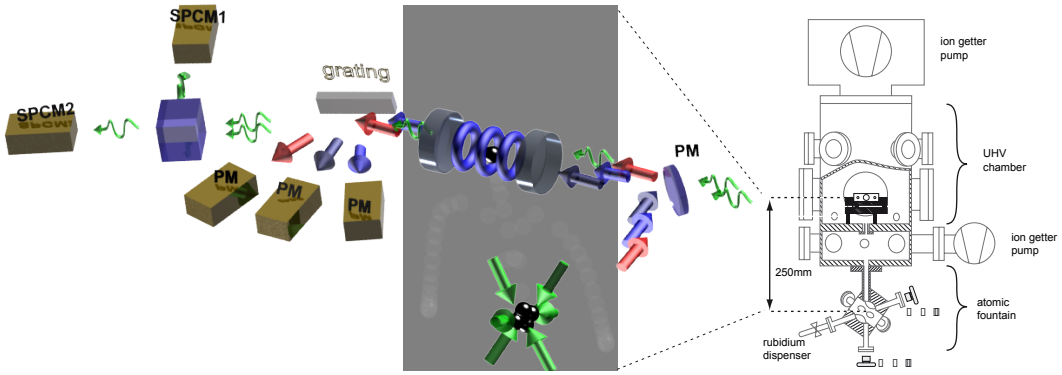


**Figure 3.1:** Schematic of the experimental setup. Cold atoms are injected into the cavity from an atomic fountain and are trapped with different intracavity dipole lasers (red and blue arrows). The coupled atom-cavity system is observed with near-resonant probe light (green photons). Dipole and probe light is separated by an optical grating behind the cavity. The vacuum chamber is sketched on the right.

### 3.1.1 $^{85}$Rb as a two-level system

We use $^{85}$Rb atoms since we can prepare them as an (almost) perfectly closed two-level system. The level scheme of the alkali metal with its one valence electron is shown in Fig. 3.2. The transition from $5S_{1/2}$ to $5P_{3/2}$ at a wavelength of 780.24 nm shows a large frequency separation from other transitions. At this wavelength optical equipment such as stable high power lasers, high quality mirrors and single-photon counting modules (SPCMs) with reasonable good detection efficiency are available. By choosing $\sigma^+$-polarization of the cavity probe mode ($\mathrm{TEM}_{00}$ mode) which is close to the cycling transition from $5S_{1/2}$, $F = 3$, $m_F = 3$ to $5P_{3/2}$, $F = 4$, $m_F = 4$, the system is pumped to these extreme Zeeman levels (see Fig. 3.3) and also probed on this closed transition. The atomic polarization decay rate is $\gamma/2\pi = 2.99$ MHz.

### 3.1.2 Atomic fountain

Rubidium atoms are released by electric heating of a rubidium dispenser (SAES Getter) into the background gas and are accumulated in a MOT. Here the detuning of the MOT beams is $\Delta/2\pi = 45$ MHz below the cycling transition of $^{85}$Rb from $5S_{1/2}, F = 3$ to $5P_{3/2}, F' = 4$. The atoms are then cooled via polarization gradient cooling in an optical molasses to temperatures of about $5\,\mu$K. To inject the atoms into the cavity, we afterwards detune the lower molasses beams to operate in an atomic fountain configuration. The atoms are launched towards the cavity, located 25 cm above the MOT. When ramping the three lower molasses beams continuously by $\approx 1$ MHz/ms to $\Delta/2\pi = 42$ MHz, the atomic molasses is cooled in a moving frame and the atoms are launched as soon as they leave the cross section of the molasses beams. The atoms follow a

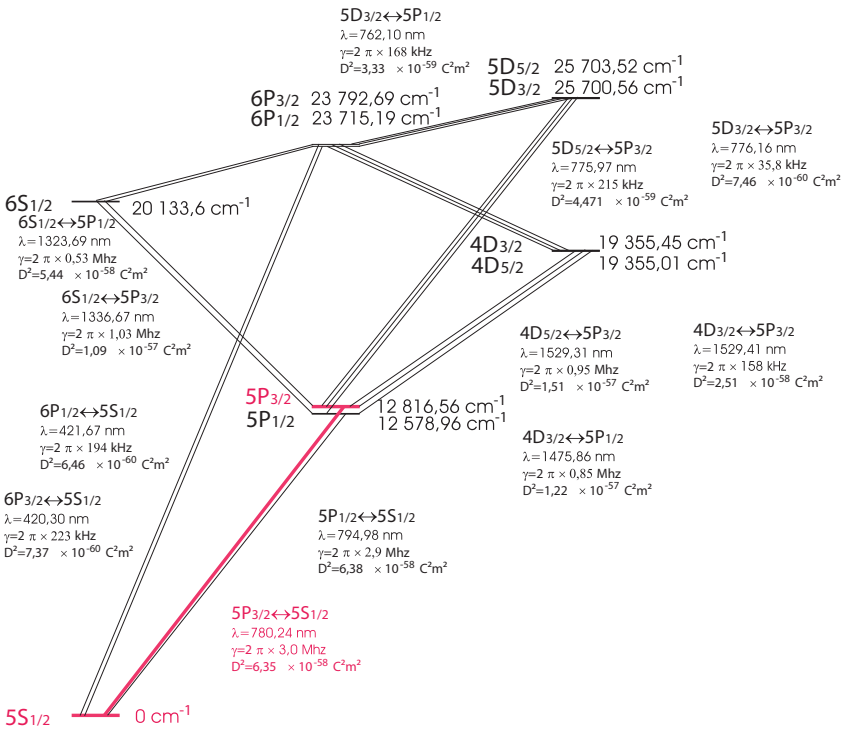


**Figure 3.2:** Level scheme of $^{85}$Rb. The transition from $^5S_{1/2}$ to $^5P_{3/2}$ with a frequency of 780.24 nm is well separated from all other transition frequencies.

ballistic flight such that the slowest atoms reach the cavity axis after $\approx 210$ ms and ideally have their turning point there. The large distance and moderate launching velocity allows for a large spread in the arrival times between fast and slow atoms. Single, initially cold atoms that arrive last can be trapped. In order to guarantee a low collision rate of the atoms with background gas they cross a differential pumping tube on their way to the cavity. In the main vacuum chamber a ultra high vacuum of about $3 \times 10^{-10}$ mbar is achieved by continuously pumping with an ion getter pump with 300 l/s.

### 3.1.3 High-finesse optical cavity

Two identical mirrors form an optical, near-planar cavity of high finesse ($F = 490000$). All relevant parameters are summarized in Tab. 3.1. The cavity length is set to $l = 123\,\mu$m and a fine adjustment of the length via piezo control matches the cavity resonance frequency to the atomic transition frequency. Due to the high finesse of the cavity one main challenge is to stabilize the cavity length and suppress thermal drifts and mechanical vibrations. Changes on the order of 1 pm shift the cavity already out of resonance. A passive isolation of the cavity from acoustic noise is achieved by a vibration isolation stage consisting of two copper stages separated by viton tubes. The active length

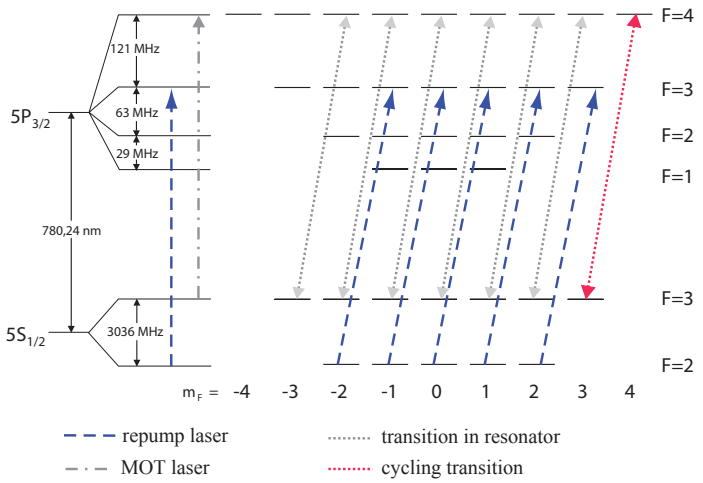


**Figure 3.3:** Hyperfine level scheme of the transition from ${}^5S_{1/2}$ to ${}^5P_{3/2}$ for ${}^{85}$Rb.

stabilization is done using a Pound-Drever-Hall technique and feedback onto the piezo tube controls the mirror distance [Pup07b]. We optimized the cavity lock, e.g., by an electronic noise reduction via band pass filters which allows us to stabilize the cavity with laser powers as low as 10 nW. As the stabilization beam also creates a dipole potential for the atoms (see in the next sections) it is important to be able to stabilize the cavity with very low power. The error signals for 40, 30, 20 and 10 nW are shown in Fig. 3.4 a)-d) and are obtained by scanning the cavity length while recording the transmitted intensity of the stabilization laser.

For given cavity parameters the intracavity photon number, $N$, can be converted into a transmitted intensity, $I$, by

$$I \approx T \times \frac{c}{2l} \times h\nu N\,, \tag{3.1}$$

where $l$ is the cavity length and $T$ is the transmission coefficient as depicted in Tab. 3.1. In this thesis we have assumed that for $N = 1$ the transmitted intensity is $I = 0.9$ pW.

### 3.1.4 Laser system

To observe and control the atom inside the cavity different modes can be excited. The relevant modes for our experiment are shown in Fig. 3.5.
A Titanium Sapphire laser (TiSa 780) excites a $\mathrm{TEM}_{00}$-mode at 780 nm which is close to the atomic transition in order to probe the coupled system.
All other cavity modes that are used are far detuned with respect to the atomic transition and are used to create different dipole potentials. An external cavity diode laser at 785 nm (ECDL 785) that is red-detuned from the atomic transition by two free-spectral ranges (FSR), excites a $\mathrm{TEM}_{00}$-mode and serves

| | | | |
|---|---|---|---|
| radius of curvature | 200 mm | diameter | 7.75 mm |
| transmission coefficient | $T = 2.8$ ppm | loss coefficient | $L = 4.5$ ppm |
| free spectral range | FSR$/2\pi$ = 1.21 THz | cavity length | l $= 2\pi c/2$FSR $= 123\mu$m |
| linewidth (HWHM) | $\kappa/2\pi = 1.25$ MHz | Finesse | $F =$FSR$/2\kappa =$ 490000 |
| mode waist | $w_0 = 29.1\,\mu$m | mode volume | $V = \pi\omega_0^2 L/4$ |
| spatial mode function ($TEM_{00}$) | $\psi(x,r) = \cos(kx)e^{-(y^2+z^2)/w_0^2}$ | atom-cavity dipole coupling strength | $g(x,r)=$ $g_{max} \times \psi(x,r)$ |
| maximum coupling strength | $g_{max} = \sqrt{\omega_c/2\hbar\epsilon_0 V}\,d_{ge} =$ $2\pi \times 16$ MHz | Transmission per intracavity photon | 0.9 pW |

**Table 3.1:** Parameters of the mirrors, the high-finesse cavity, and the coupled atom-cavity system.

as an attractive, red-detuned dipole trap in three dimensions. The antinodes coincide in the cavity center with the antinodes of the probe mode. A good mode matching is only present in the center of the cavity, while the different laser frequencies induce an increasing displacement between the modes with increasing distance from the cavity center.
An ECDL operates at 775 nm (ECDL 775) and excites a $TEM_{10}$ or $TEM_{01}$-mode, two FSR blue-detuned from the atomic transition. The $TEM_{01}$- and $TEM_{10}$-mode are individually addressable due to a 6 MHz frequency separation. Scanning the laser across both resonances rotates the excited $TEM_{01}$-mode. When simultaneously exciting a $TEM_{10}$- and $TEM_{01}$-mode results in a torus-shaped dipole trap [Pup07b]. By changing the intensity balance between the $TEM_{10}$- and $TEM_{01}$-mode a rotationally symmetric or asymmetric torus potential can be formed.
A TiSa laser at 772 nm (TiSa 772) excites a three FSR blue-detuned $TEM_{00}$-mode providing an additional axial confinement for the atom. Here, in the cavity center the modes of the 772 nm mode coincide with the antinodes of the probe mode.
In order to stabilize all lasers with respect to each other, a precise frequency reference is obtained by using a transfer cavity. In short, the locking procedure works as follows. The TiSa 780 laser is locked to a Rb line using Doppler-free saturation spectroscopy on a vapor cell. This laser is then used to stabilize the length of the transfer cavity (L=470 mm, FSR$/2\pi = 310$ MHz, $\kappa/2\pi = 150$ kHz). The transfer cavity serves as a frequency reference for all other lasers (ECDL 785, ECDL 775 and TiSa 772). They are stabilized

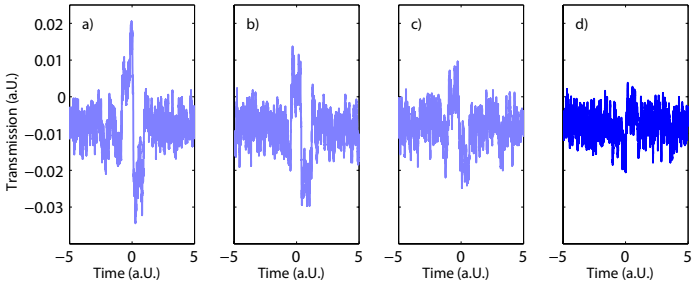


**Figure 3.4:** Optimized error signal for the length stabilization of the high-finesse cavity. The error signal is obtained by scanning the cavity frequency while recording the transmission of the locking laser through the cavity. a)-d) shows the error signal for a laser power of 40, 30, 20 and 10 nW. Even with the smallest error signal the cavity stabilization works. In d) the right side of the error signal is hidden in the noise.

using a Pound-Drever-Hall technique on a longitudinal mode of the transfer cavity which has a frequency close to the resonance frequency of the high-finesse cavity. Before coupled to the high-finesse cavity, all lasers pass through acousto-optic modulators (AOMs) in double-pass configuration (2x) which allow for fine tuning of the frequency and amplitude to match the resonance conditions. The ECDL 785 is in turn used to stabilize the length of the high-finesse cavity. The same laser also creates the red-detuned, intracavity dipole trap whose intensity is switched during some of the experiments, as discussed later. The intensity switching is compensated by an electronic divider in the stabilization loop. An overview of the laser system is given in Tab. 3.2.

### 3.1.5 Detection

An optical grating behind the cavity separates the probe beam and all dipole trap beams from each other. The holographic reflection grating (American Holographics) achieves a maximum efficiency of 90%. Remaining light with different frequency is filtered by a narrow band interference filter (Nanolayer) with a central frequency of 780 nm and a 1 nm band width. The maximum transmission of the filter is 80 %. Single photons of the probe light are directed towards single-photon counting modules (SPCM) fabricated by Perkin&Elmer (SPCM AQR-13) which allow for a quantum efficiency above 60%. We use two SPCMs, each seeing half of the transmitted light, in a Hanbury Brown and Twiss (HBT) configuration. This has two advantages. Firstly, it enables us to determine the photon-photon correlations of the transmitted light. Secondly, it reduces the losses of the detectors which are caused by their dead time after one photon has been detected. With dead times of $\approx 50$ ns per detector (correction factor 1.05 for a count rate of 1 MHz) this becomes important only for high probe powers. The detectors show a dark count rate of $\approx 300$ Hz.

| | model | wavelength (nm) | frequency stabilization | function in the experiment |
|---|---|---|---|---|
| TiSa 780 | Coherent MBR110 | 780.2 (near-resonant) | Doppler-free saturation spectroscopy | a) length stabilization of the transfer cavity<br>b) 2 beams for upper and lower MOT beams<br>c) near-resonant probe laser for the science cavity |
| ECDL 780 | Toptica DL100 | 780.2 (near-resonant) | Doppler-free saturation spectroscopy | a) repumping laser in the MOT<br>b) repumping laser perpendicular to the science cavity axis |
| ECDL 785 | Toptica DL100 | 785.2 (-2 FSR) | Pound-Drever-Hall to transfer cavity | a) red-detuned intracavity dipole trap<br>b) length stabilization of the high-finesse cavity |
| ECDL 775 | Toptica DL100 + Toptica Boosta (tapered amplifier) | 775.2 (+2 FSR) | Pound-Drever-Hall to transfer cavity | a) blue-detuned, torus-shaped intracavity dipoletrap |
| TiSa 772 | Coherent MBR110 | 772 (+3 FSR) | Pound-Drever-Hall to transfer cavity | blue-detuned axial trapping potential |

**Table 3.2:** Overview of the laser system and its functionality. All diode lasers are set up in Littrow configuration.

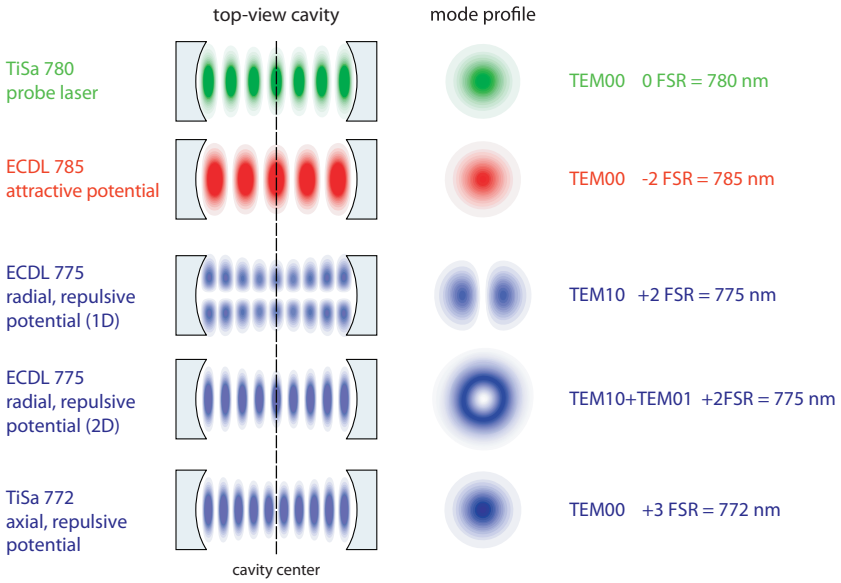


**Figure 3.5:** Employed cavity modes. The atom-cavity system is probed with light at 780 nm, close to the $D_2$-line of $^{85}$Rb. A far red-detuned laser at 785 nm (ECDL 785) resonantly excites a two free-spectral ranges (FSR) detuned $TEM_{00}$-mode supported by the cavity and a second laser (ECDL 775) at 775 nm excites a $TEM_{10}$- and $TEM_{01}$-mode two FSR blue-detuned with respect to the probe light. For an additional axial confinement, another blue-detuned TiSa laser at 772 nm is injected, three FSR apart.

The overall detection efficiency of a single probe photon inside the cavity amounts to $\eta = 0.067$. It is determined by the product of the extraction efficiency $\eta_c$ of a photon from inside the cavity into the right output mode and the detection efficiency $\eta_d$ of a photon in this mode by the two detectors. The efficiency decreases with the photon flux due to the finite dead time of the detectors. Here, we assume a low photon flux, well below 1 MHz. We determine an optimal cavity transmission of 0.175 which is slightly more than what we expect from $(T/(T+L))^2 = 0.147$, where $T$ and $L$ are the mirror transmission and loss coefficients (see Tab. 3.1). This yields $\eta_c = 0.21$ (expected $T/2(T+L) = 0.192$). $\eta_d$ is specified as 0.32.
During this work (see Chap. 7) the filtering of the probe light was changed. Due to the improvements in the production of optical, band-pass filters, the grating plus the Nanolayer filter is replaced by narrow band filters from Semrock at 780 nm. The filter achieves a transmission above 99 %. Tilting the filter by $\approx 5^o$ allows to separate light with a different wavelength, e.g. from dipole lasers while still keeping the high transmission for the probe light. Although the chosen wavelength of 780 nm is transmitted within a very narrow frequency band ($\approx 2$ nm), the filter transmits far-detuned light, e.g. at twice the central frequency. Multiple reflections on two mirror surfaces, which are

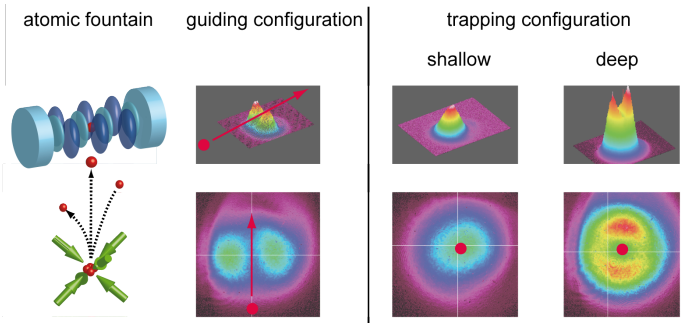


**Figure 3.6:** Intensity profile of typical guiding and trapping configurations. The atoms, launched from an atomic fountain, are guided into regions of strong coupling by a combination of red-detuned (ECDL 785, $TEM_{00}$) and blue-detuned (ECDL 775, $TEM_{10}$) intracavity light fields. Upon detection of a single atom in the cavity mode, the red-detuned dipole trap is switched from low power (80 nW) to higher power (170 nW). During the guiding process the intensity profile is dominated by the blue-detuned guiding-mode. In two possible trapping configurations the blue-detuned torus-shaped trap is switched to low power (50 nW) or high power (800 nW) when the atom is detected. The intensity profile is either dominated by the red-detuned trap in case of a low torus trap power (shallow), or it shows the overlap of both traps in case of a high torus trap power (deep). In the later case the light intensity in the center comes from the red-detuned trap only.

only reflective around 780 nm therefore enable a further suppression of the stray light. The overall detection efficiency improved with this method by about a factor of 2 to $\eta = 0.14$. While $\eta_c$ remains unchanged, $\eta_d$ improved to 0.68 with an optical transmission of 0.96 and intrinsic SPCM efficiencies of 0.7.
The various dipole lasers transmitted through the cavity are each detected with a photomultiplier (Hamamatsu, H6780-20) amplified with a low-noise transimpedance amplifier (Femto current amplifier, gain 500 kΩ, bandwidth 4 MHz). The transmission of the red-detuned dipole trap is recorded via a two-channel, transient recorder card (Spectrum PCI.248). Alternatively, if the blue-detuned dipole lasers are also used, a four-channel oscilloscope (LeCroy waverunner 6030) records the transmission of the dipole laser.

### 3.1.6 Guiding configurations

Different guiding configurations are used for the purpose of guiding the atoms efficiently into regions of strong coupling. The first guide is created by red-detuned dipole light (ECDL 785) which is superimposed with the probe laser in the center of the cavity (see Fig. 3.5) leading to an efficient guiding into the probe mode. For an additional radial guiding the blue-detuned dipole laser (ECDL 775) excites the $TEM_{10}$-mode. An example of a guiding configuration

is shown in Fig. 3.6, where the direction of the atomic injection is marked with a red arrow. Here, a red dipole trap of 80 nW is superimposed with the blue, radial guide of 600 nW. As discussed earlier, a good mode matching is only present in the center of the cavity. Therefore, only atoms which enter the cavity in the center are registered.
This technique of guiding the atoms into the cavity does not rely on a transport laser focussed through the side of the two cavity mirrors, as described in [Kuh01], [For07], [Nus05]. In our experiment the small slit of $\approx 60\,\mu$m between both mirrors makes such a guiding technique practically impossible (without scattering the dipole beam on the mirrors).

### 3.1.7 Atom detection

Near-resonant light (TiSa 780 laser) is tuned close to the cycling transition of the $D_2$ line of $^{85}$Rb. It impinges on the input mirror exciting the $\mathrm{TEM}_{00}$-mode of the cavity with the purpose of probing the atom-cavity system. As described in Sec. 2.3, the presence of the atom shifts the eigenenergies of the system. To detect single atoms the transmitted light through the cavity is continuously monitored. Each atom coupling to the cavity mode induces a sharp dip in the transmission when the probe laser is on resonance with the empty cavity. Typical transit times of the atoms are a few hundred microseconds [Mün99b]. To avoid 'artificial' atoms, which are created when the transmission drops due to instabilities in the stabilization laser, the data is disregarded when a drop in transmission of the probe laser is accompanied with a drop in transmission of the dipole lasers.

### 3.1.8 Trapping configurations

Once a slow atom is detected the dipole traps are rapidly switched from the guiding configuration to a trapping configuration (see Fig. 3.6). The starting trigger can only be enabled in a 50 ms time window 210 ms after the atoms are launched. During this time the main part of the cold atom cloud has already passed the resonator, and single slow atoms with a velocity below 0.1 m/sec enter. Three different trapping configurations are used in this thesis:
1. The red-detuned dipole trap. In order to trap the atom in a conservative potential, the trap depth is rapidly increased as the atom enters the mode. The red dipole trap is typically switched from 80 nW to 170 nW. This is already sufficient to trap the atom in three dimensions.
2. In order to change the trapping potential in the radial direction without modifying it in the axial direction, the red-detuned dipole trap is superimposed with the blue-detuned, torus trap, forming a repulsive, radial barrier. The torus asymmetry is used, for example, to enhance the confinement along the direction of the atomic injection.

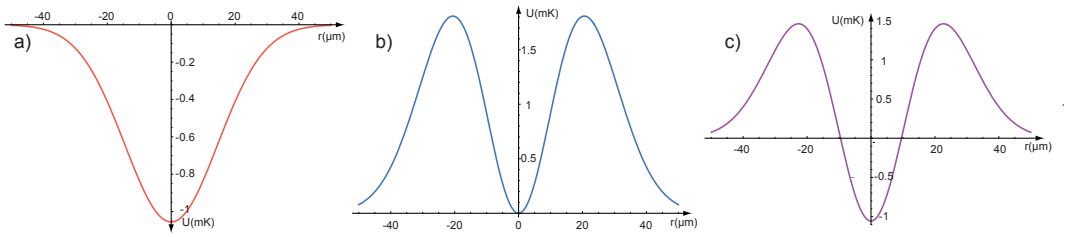


**Figure 3.7:** Trapping potential in the radial direction for different traps. a) A pure red-detuned $TEM_{00}$-mode with a power of 170 nW corresponds to an attractive, 1 mK deep trapping potential with a maximum in the center. b) A pure blue-detuned, torus-shaped trap with a power of 800 nW shows a trap depth of 1.8 mK with a dark center and maximal light intensity at $\approx 20\,\mu$m. c) The combined trap has an overall trap depth of 2.5 mK

3. Further control of the axial confinement can be achieved by adding a repulsive axial potential using the TiSa 772 laser. Here, the antinodes at the center of the cavity overlap with the nodes of the probe field, forming a repulsive axial potential.

In summary, the red trap is comparatively easy to handle, as there is only one trapping laser involved, and shows a high atom trigger rate. The combined trap (configuration 2) also shows a high atom trigger rate, but the data storage of the dipole laser intensities, here done with the oscilloscope, adds a few seconds of data acquisition time for each trapped atom. The corresponding increase in the measurement time is compensated by a reduced loss rate. The additional radial confinement repels the atoms towards the cavity axis, thereby favoring events where atoms are strongly coupled to the cavity and decreasing the losses of the atoms in the radial direction. Particularly, when measuring on resonance with the normal mode, the additional radial trap improves the storage time (see Sec. 3.1.9). In the experiments presented in this thesis, the atoms are either trapped in configuration 1 or 2. The mode pictures of two example configurations are shown in Fig. 3.6. Here, in one configuration the torus trap has a power of only 50 nW with a the red trap of 170 nW. In the second combination the torus potential is increased to 830 nW.

The third configuration with an additional axial trapping potential is only used for a few specific measurements in this thesis. The main disadvantage of this trap is the reduced trigger rate and the reduced average storage time, as all atoms that are not perfectly sitting in the cavity center are ejected.

The radial trapping potentials for different traps are shown in Fig. 3.7. They are obtained from the Stark shift as explained in detail in the appendix of [Sch08b]. The radial dependence of the trapping potential is obtained by multiplying with the mode profile, which is given by a gaussian distribution $e^{(-r^2/w_0^2)^2}$ for the $TEM_{00}$-mode and by $(\sqrt{2}/w_0 r e^{-r^2/w_0^2})^2$ for the torus-shaped potential corresponding to a $TEM_{10}$-mode. The oscillation frequency is estimated by

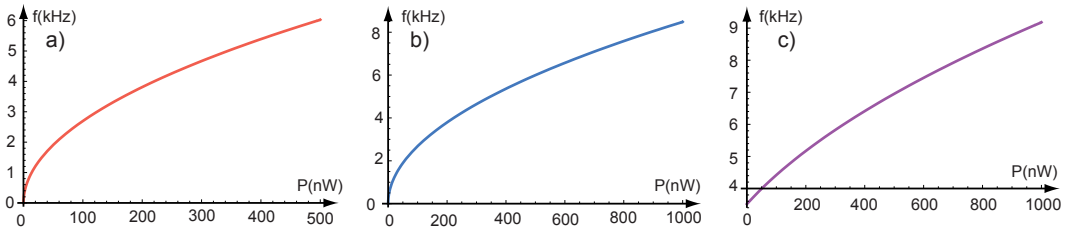


**Figure 3.8:** Oscillation frequency in the radial direction for different trapping potentials. a) The oscillation frequency f varies between 0 and 6 kHz in a pure red-detuned $TEM_{00}$-mode with a power between P= 0 and P= 500 nW. b) For a blue-detuned, torus-shaped trap with a power between 0 and 1$\mu$W the oscillation frequency lies between 0 and 8 kHz. c) The combined trap with a red-detuned potential of 170 nW and a blue-detuned potential between 0 and 1 $\mu$W results in an oscillation frequency between 3.6 and 9 kHz.

expanding the trapping potential into a power series around $r = 0$. Using $k = -F/r$ with $F = dU/dr$ gives the oscillation frequency $f = 1/(2\pi) \times \sqrt{k/m}$, where $m$ is the mass of $^{85}$Rb. The estimated oscillation frequencies for the different trapping configurations are plotted in Fig. 3.8.
In the experiment the Stark shift is averaged over different positions of the atom in the mode and therefore deviates from the theoretically obtained value. In this thesis the average Stark shift is obtained from fits to the normal mode spectrum.

### 3.1.9 Measurement sequence

After the atom is trapped, different measurement sequences control the parameters of the coupled system. In this thesis two sequences are used.
The first sequence, called 'single-shot' measurement, is used, e.g., to investigate the storage time of an atom in the trap with fixed parameters. When the atom is detected the probing and all trapping lasers are switched to a trapping configuration with constant frequency and power of the laser beams. The transmitted intensities of the probe and the dipole lasers are monitored and registered. A typical measurement of guiding and trapping a single atom with this sequence is shown in Fig. 3.9, where the probe beam transmission is plotted versus time. This measurement was performed with a power of only 10 nW for the stabilization light (=red trap). It shows three single atom transits causing three dips in transmission and one short trapping event of $\approx 1$ ms.
The second sequence, called 'switching measurement', allows us to change the probe beam detuning and to measure the spectrum of the coupled atom-cavity system. This method ensures a constant coupling strength via postselection. Therefore, the sequence alters between two interval types. During the 'probe interval' the transmission is acquired for different detunings of the probe laser and is used for data evaluation. Each probe interval is sandwiched by two

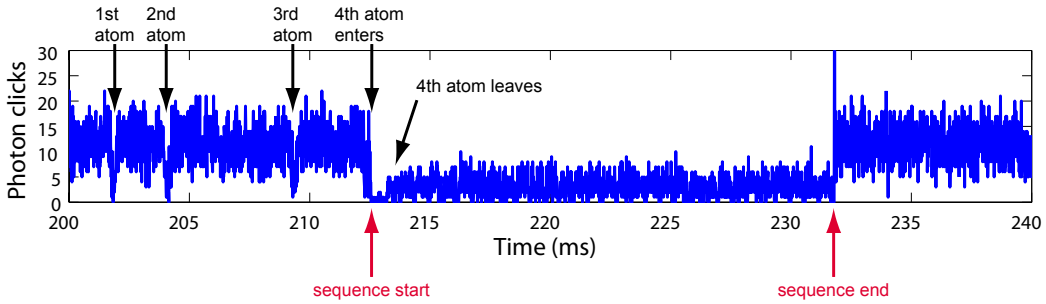


**Figure 3.9:** Example trace for a single shot measurement. Observing the transmitted probe light reveals 3 atom transits, while the fourth atom is trapped for a short time.

'qualification intervals'. Here, the probe laser is on resonance with the empty cavity, $\Delta_c = 0$, and the transmitted intensity allows for a determination of the effective atom-cavity coupling by comparison with the transmission of the empty cavity. The postselection ensures a certain coupling strength in the probe intervals by imposing limits on the average transmission in both neighboring qualification intervals. Probe intervals are only used for the evaluation if the transmission in both neighboring qualification intervals satisfies these limits. The limits are defined relative to the transmission of the empty cavity, called normalized transmission in the following. For example, a normalized transmission of 1 means that all probe intervals are taken into account. The normalized transmission can be translated into a coupling strength via

$$T = \frac{\kappa^2}{\Delta_c^2 + \kappa^2} \times \frac{1}{(1-\nu)^2}\,, \tag{3.2}$$

with $\nu = \frac{g^2}{(\Delta_a + i\gamma)(\Delta_c + i\kappa)}$ [Mur03]. In addition the qualification intervals are used to axially cool the atom by cavity cooling. This ensures a good coupling even when the probe interval involves axial heating. The cooling and heating regions are marked in Fig. 3.10 by blue and red regions, respectively. In this example, the friction coefficient was obtained for an atom averaged over a region from $-\lambda/4$ to $\lambda/4$ along the cavity axis (see [Mau05a] for a detailed description). To allow for a sufficient cooling, and for enough time to determine the coupling strength, the cooling periods are typically 500 $\mu$s long and the probing intervals are 100 $\mu$s long.
The $\Delta_a\Delta_c-$parameter plane of a typical experiment is depicted in Fig. 3.10. The experiment starts with an atomic detuning of $\Delta_{a,0}/2\pi = 35$ MHz without Stark shift and with $\Delta_c/2\pi = 0$ MHz. The probe light is 35 MHz blue-detuned from the atomic resonance to axially cool the atom as soon as it enters the cavity mode by cavity cooling [Mau04]. When the atom is trapped, the red dipole trap will induce a Stark shift on the atom depending on the laser power. In this case a laser power of 170 nW induces a shift of $S/2\pi = 24$ MHz (red

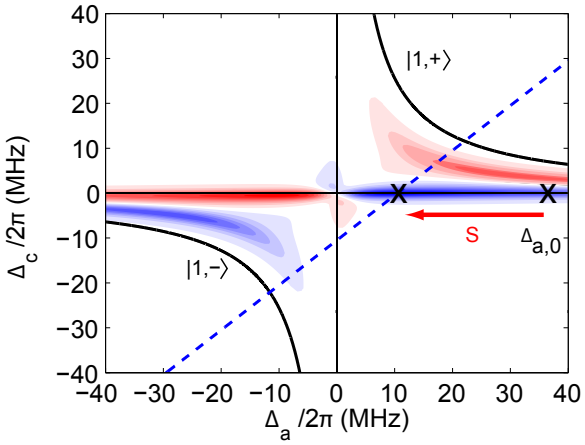


**Figure 3.10:** Schematic of a typical scanning procedure. Starting with an initial atom detuning of $\Delta_{a,0}/2\pi = 35$ MHz and $\Delta_c/2\pi = 0$ MHz the Stark shift (indicated by a red arrow) shifts $\Delta_a$ by $S/2\pi = 24.5$ MHz to $\Delta_a/2\pi = 10.5$ MHz. The scan is performed by switching the frequency and the power during the probe intervals to points along the diagonal, dashed, blue line crossing the resonance frequencies of the coupled system ($|1,-\rangle$ and $|1,+\rangle$). The coupling strength is set to $g/2\pi = 16$ MHz in the calculation. Cooling and heating regions are marked by underlying blue and red areas, respectively.

arrow), resulting in an effective laser-atom detuning of $\Delta_a/2\pi = 11$ MHz. To measure the spectrum the probe laser is switched to a predefined frequency and intensity during the probe interval. This changes $\Delta_a$ and $\Delta_c$ simultaneously where each shot (atom) will measure one point of the spectrum (blue dashed line). The average over all probe intervals then gives the final spectrum. The qualification intervals at $\Delta_c = 0$ typically operate at probe powers of 0.3 pW. The spectrum of the transmitted probe light is shown in Fig. 3.11 a) for two different traps. The red data corresponds to a red dipole trap of 170 nW. The blue data is obtained for the same parameters, but with an additional 250 nW of the blue-detuned torus trap. For both measurements the probe power is set to 1.5 pW, and the coupling strength is restricted to 0.05 of the empty cavity transmission. The spectra show the normal mode peak $|1,-\rangle$ with a slight frequency shift due to a changed Stark shift. The corresponding loss rates are shown in Fig. 3.11 b). The additional torus potential improves the loss rate. Particularly when operating in a heating region, like on resonance with one of the normal modes, the loss rates are reduced due to the additional axial confinement.

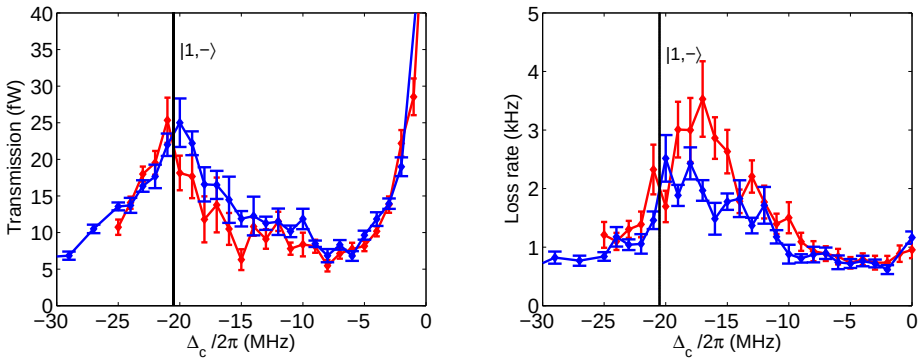


**Figure 3.11:** Normal mode scan for two different traps, a red dipole trap of 170 nW (red data) and the same trap superimposed with a blue, torus-shaped radial confinement of 250 nW (blue data). a) The transmitted power is recorded while the probe laser frequency is scanned. The normal mode ($|1,-\rangle$) is observed in both cases with a slight frequency shift. b) The loss rates clearly show reduced losses when the torus trap is superimposed, especially when measuring in a heating region on the right side of the normal mode.

### 3.1.10 High power effects

When coupling light into a high-finesse cavity the resonance frequencies drift due to thermalization effects. To study the influence of laser light inside the cavity on the resonance frequencies we monitor the transmission of all lasers while significantly changing the excitation power of the TiSa 772 laser. While all $TEM_{00}$-modes show stable resonance frequencies (not shown), the high intracavity laser power shifts the resonance frequencies of the higher-order modes. As shown in Fig. 3.12 the $TEM_{10}$-mode a), $TEM_{01}$-mode b) and the guiding mode c) shift by up to 350 kHz when the power of the TiSa 772 laser is increased from 0 nW to 1 $\mu$W. The measurement is confirmed by two independent measurements on different days (blue and black data).

## 3.2 Observation and characterization

To characterize the coupled atom-cavity system we mainly rely on two methods. Counting the transmitted photons allows for the evaluation of the transmitted intensity necessary to do spectroscopy. Light statistics are obtained by calculating photon-photon correlations.

### 3.2.1 Photon counting

Each photon detected by a SPCM creates an avalanche of electrons in the detector. The rising edges of the emitted digital pulses ($\approx$ 30 ns) correspond to the photon arrival times which is registered with a two-channel time-digitizer

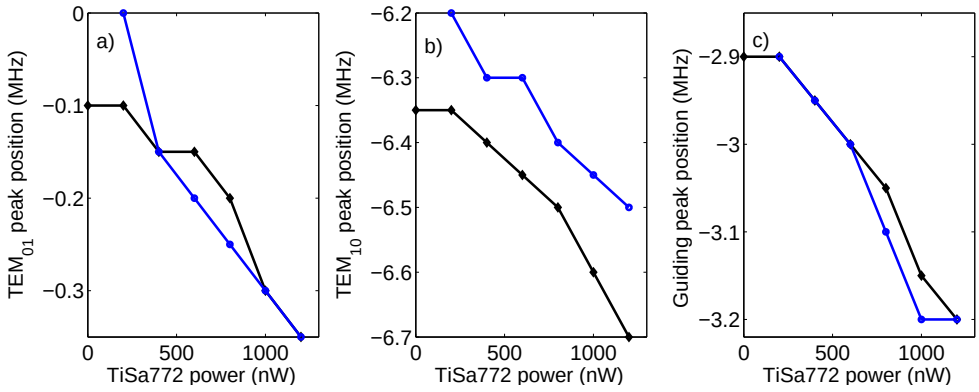


**Figure 3.12:** Shift of the resonance frequencies in the presence of strong cavity excitation. The resonance frequencies of the higher-order modes $TEM_{01}$-mode a), $TEM_{10}$-mode b) and the guiding mode c) shift depending on the excitation strength of the TiSa 772 laser. Blue and black data are obtained on different days.

computer card (P7888, FASTComptech) with a resolution of 1 ns. The number of photons per time bin, the count rate $\Re$, refers to the averaged transmitted intensity, $I$, via

$$I \;=\; \Re \,\frac{1}{\eta}\, h\nu \, 10^{12}\,(\mathrm{pW/Hz})\,, \tag{3.3}$$

where $\eta$ includes all losses in the detection. For example, a count rate of 1 MHz on the detectors corresponds to an average transmission of 1 pW. After realigning the detection setup (see Sec. 3.1.5) this number improved to 1.2 MHz.

### 3.2.2 Photon-photon correlations

Installing the two SPCMs in Hanbury Brown and Twiss (HBT) configuration allows us to detect two photons at the same time and to calculate the normalized, second-order correlation function $g^{(2)}(\tau)$, as introduced in Sec. 2.4.2. To obtain $g^{(2)}(\tau)$ we first evaluate the correlation term $\Re_{coinc}(\tau)$ which displays the count rate of photons detected within a time difference of $\tau$. Therefore, we divide the probe interval, $t_{probe}$, of a switching measurement in short intervals of length $\Delta t_i$ which defines the minimal time bin (10 ns in the experiment). For each interval $\Delta t_i$ from SPCM1 that contains a photon click we count the coincident photon clicks from SPCM2 in the interval $\Delta t_i + \tau$. The time difference between both intervals is the so-called correlation time $\tau$. The overall coincidence count rate is obtained by adding the number of coincidences for each correlation time bin $N_{coinc}(\tau, \Delta t_i)$ for all start time bins as well as for all probe intervals, #, and normalizing it to the total number of time bins in all

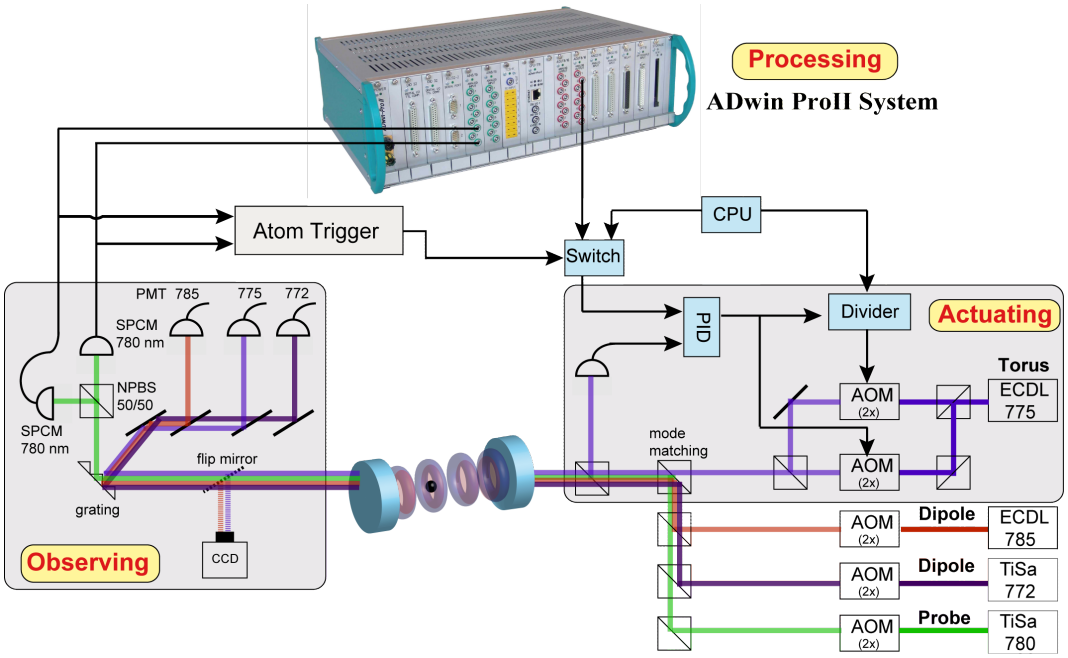


**Figure 3.13:** Scheme of the real-time control setup. For simplicity only the real-time computing system and the connected devices are displayed.

probe intervals,

$$\Re_{coinc}(\tau, \Delta t) = x(\tau) \times \frac{\sum_{\#} \sum_i N_{coinc}(\tau, \Delta t_i)}{\sum_{\#} t_{probe}/\Delta t} \,. \tag{3.4}$$

Here, the weighting factor $x(\tau) = t_{probe}/(t_{probe} - |\tau|)$ compensates for the finite length of the probe interval $t_{probe}$. To normalize the correlations to the intensity, we calculate the count rates of each detector, $\Re_1$ and $\Re_2$, by adding the clicks of each detector $n_{1/2}(\tau, \Delta t)$ via

$$\Re_{1/2}(\Delta t) = \frac{\sum_{\#} \sum_i n_{1/2}(\tau, \Delta t_i)}{\sum_{\#} t_{probe}/\Delta t} \,, \tag{3.5}$$

and derive $g^{(2)}(\tau)$ by

$$g^{(2)}(\tau) = \frac{\Re_{coinc}(\tau, \Delta t)}{\Re_1(\Delta t)\Re_2(\Delta t)} \,. \tag{3.6}$$

## 3.3 Real-time system control

A main part of this thesis concentrates on the real-time control of the coupled system. By switching the trapping potential in an appropriate way, the atomic motion is either influenced and locked to an external actuator (see Sec. 4.4) or a feedback algorithm is used to control the atomic motion in the cavity mode

(see Chap. 5). Here, we present the technical implementation of this real-time control. A schematic of the control loop is shown in Fig. 3.13. The loop can be divided into three steps: observing, processing and actuating.
The probe laser transmitted through the cavity holds information about the atomic position. Therefore the observation of the atomic motion is done by monitoring the transmitted probe beam intensity, as explained in Sec. 2.3.3.
The next step in the control loop is the processing of the acquired information. The routine is triggered upon detection of a single atom, which switches (Switch) the control of the blue-detuned torus power from the computer controlled measurement sequence (CPU) to the real-time processor (ADwin ProII-System). Both SPCM signals are directly processed in the real-time system, and, based on the count rate, a decision of how to act on the atom via a change in the potential depth of the blue-detuned torus-shaped dipole trap is made. The specific algorithms are discussed in the corresponding sections (Sec. 4.4 and Sec. 5.2.3).
The final part of the feedback loop is the actuation. The output voltage of the real-time computer controls the intensity of the light of the torus potential, which is the blue detuned ECDL 775 laser. The symmetry of the torus potential is adjusted by balancing the intensities of the $TEM_{01}$ and $TEM_{10}$ modes. Here, the intensity ratio is set by the CPU, controlling a divider before one of the AOMs. A CCD camera imaging the mode profile verifies the symmetry.

# 4 Characterization and control of the motion of a single atom

## 4.1 Motivation

The coupled atom-cavity system has proven to be an ideal system to monitor the motion of a single atom inside an intracavity dipole trap [Pin00, Hoo00]. Here, we want to show that we can not only observe and analyze the atomic motion, but also manipulate and control it.
In general the atomic motion is influenced by two types of forces. The first is a Newtonian-type of force which is determined by the gradient of the trapping potential as well as the near-resonant probing potential. It results in a deterministic oscillation of the atom in the trap. The second is a force of a random nature [Mur06b] caused, e.g., by spontaneous emission from the atom or the cavity. It results in a Brownian motion of the atom in the trap. When using probe light close to resonance with the atom or the cavity, this random force becomes significant and disturbs the Newtonian motion. This makes the atom an oscillator with a very low quality factor (Q-factor), which means the coherence time of the oscillation is very short. Nonetheless, when using an adequate actuator the oscillation of the atom in the trap can be controlled by an external driving field.
In this chapter we will first introduce the parameter regime we are working in (see Sec. 4.2). The atomic motion in the trap in the axial and the radial direction is analyzed in Sec. 4.3, and the possibility to engineer it by modifying the trapping potential is discussed. In Sec. 4.4 different strategies are investigated to drive the atomic oscillation by modulating the depth of the trapping potential periodically in time. A conclusion in Sec. 4.5 summarizes the possibilities and limits for the control of the atomic motion.

## 4.2 Parameters for observing the atomic motion

The motion of the atom inside the cavity is monitored by the transmission of the probe beam through the coupled system. Intracavity dynamics are revealed from the change of the transmitted photon flux due to the presence of an atom (see Fig. 2.2). The most natural choice of atom, cavity, and laser detunings for observing the motion of an atom inside the cavity is to have the

laser on resonance with both the cavity and the atom.
Before choosing suitable detunings, however, one has to consider cavity heating and cooling regions. The axial motion of the atom is affected by cavity-assisted light forces which, depending on the chosen detunings, can lead to cooling or heating (see Sec. 3.1.9). A probe laser frequency similar to the empty cavity resonance allows for fluctuations in the detunings without entering a strong heating region. Even more importantly, a laser on resonance with the empty cavity provides a very strong axial cooling of the atom for $\omega_l > \omega_a$. In contrast, near the normal modes heating regions are in close proximity. Hence, a stable atom-cavity detuning is crucial when measuring on resonance with the normal modes. This is difficult to achieve due to the position dependent Stark shift of the atomic transition inside the dipole trap. In Chap. 4 and Chap. 5 we chose to operate the probe laser close to resonance with the empty cavity at $\Delta_c/2\pi = 100$ kHz and detuned from the Stark-shifted atomic resonance by $\Delta_a/2\pi = 20$ MHz. The almost resonant probing with the empty cavity shows a high contrast in the transmission signal between a well- and a badly-coupled atom (see Sec. 2.3.3 for a brief review), and therefore a large signal-to-noise ratio suitable to observe the atomic motion within a short measurement time. The atom-cavity detuning ensures a reasonable separation from heating regions. If not otherwise stated, all measurements are performed at a probe power of 1 pW. The driving amplitude, $\varepsilon$, is chosen low enough to neglect excitations to the higher-order dressed states.

## 4.3 Axial and radial motion

A detailed investigation of the motion for a single-atom trace can be found in [Mau05a]. Using a trapping potential with a tight axial confinement of $\approx \lambda/2$ and a wide radial confinement of $\approx \omega_0$, as discussed in Sec. 3.1.8, results in a fast axial trapping frequency of a few hundred kHz and a radial frequency that is a hundred times slower. The atomic motion is revealed by a continuous monitoring of the transmitted photons and is further analyzed by calculating photon-photon correlations. As the photon flux can drop below one photon per microsecond for well coupled atoms, fast oscillations are hard to resolve in transmission with a reasonably good signal-to-noise. Therefore, the axial motion is only visible in correlations averaged over an ensemble of single-atom traces. In addition, photon correlations give insight into the coherence properties of the oscillation.

### 4.3.1 Characteristics of the trapping potential

To start with the characterization of the atomic motion let us summarize the results obtained in reference [Mau05a]. For a single atom trapped in a red-

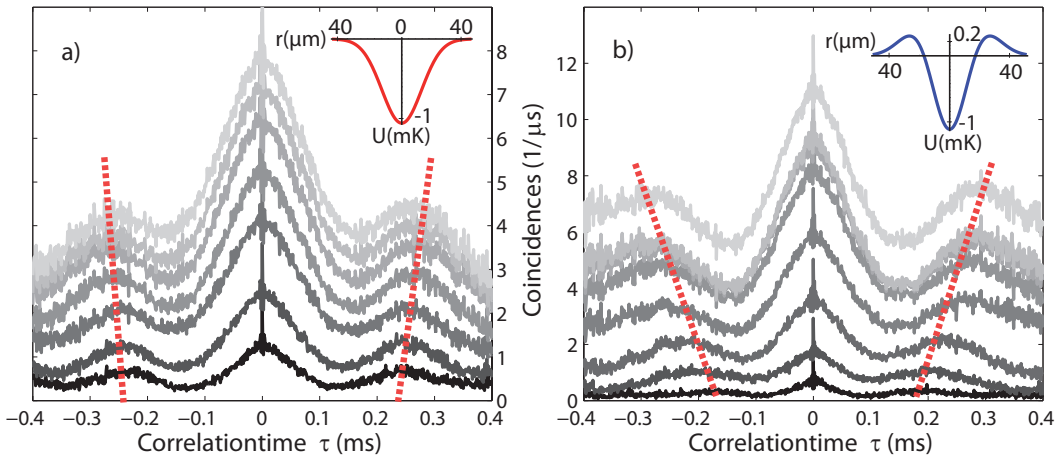


**Figure 4.1:** Anharmonicity of the trapping potential. a) Cross-correlated coincidences show typical oscillations due to the atomic motion. Here, the transmission is restricted to 0.1 of the empty cavity transmission (black curve) and lowered in steps of 0.1 up to 0.7 (light grey curve). In the case of a red-detuned dipole trap of 170 nW (1 mK) the oscillation frequency changes from $\approx 4.1$ kHz to $\approx 3.7$ kHz, revealing a marginally anharmonic potential. b) When the red-detuned dipole trap is superimposed by a blue-detuned torus trap of 250 nW the anharmonicity is more pronounced and the oscillation frequency changes from $\approx 5.5$ kHz to $\approx 3.4$ kHz for a normalized transmission of 0.05 to 0.7. The trapping potentials are shown in the upper right part of each figure.

detuned dipole trap:
1. There is a radial, atomic oscillation at 4 kHz.
2. The signature of the radial motion vanishes when the average transmission drops below a critical value for very well coupled atoms.
3. The axial oscillation frequency depends on the radial position of the atom. A dephasing of the axial oscillation and a lower oscillation frequency is observed for larger radial excursions.
4. The harmonic approximation in the trap center becomes invalid for sufficiently large oscillation amplitudes due to the Gaussian transverse profile of the trap.

In contrast to [Mau05a] we study the atomic motion averaged over an ensemble of $\approx 100$ single-atom traces. In particular, we are interested in the influence of different trapping potentials on the atomic motion. The oscillation frequency of the atom in the trapping potential depends on the oscillation amplitude. To characterize the trapping potential by this dependence we restrict the coupling strength $g$ and with it the atomic oscillation amplitude to certain limits, as described in Sec. 3.1.9. Photon-photon correlations of the transmitted probe light then reveal the atomic oscillation frequency for each oscillation amplitude. The fluctuations in the coupling strength due to the atomic motion

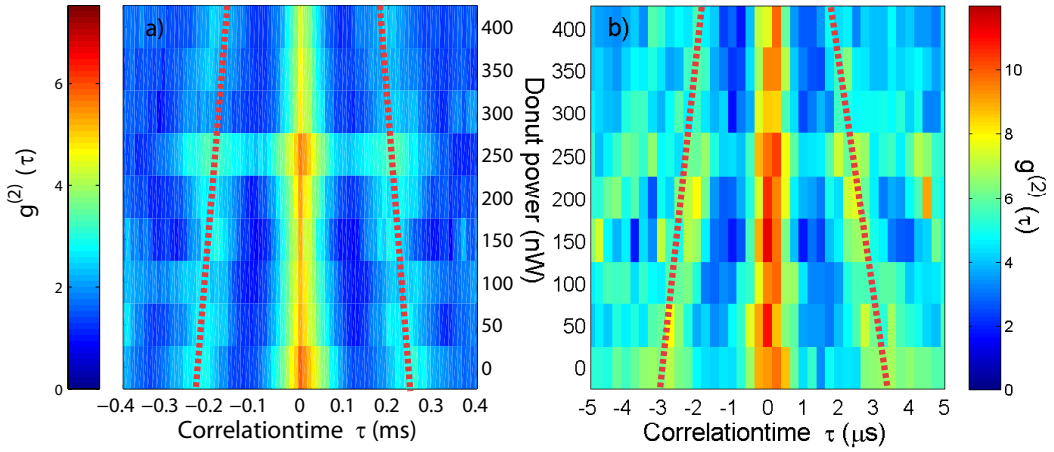


**Figure 4.2:** Influence of the torus power on the oscillation frequency. a) Changing the torus power from 0 to 400 nW shifts the oscillation frequency from 4.4 kHz to 5.5 kHz for a normalized transmission of 0.1. b) In the same measurement the axial oscillation frequency changes from ≈ 330 kHz to ≈ 500 kHz.

creates an oscillation in the correlation function, where the characteristic oscillation frequencies are directly visible. Figure 4.1 shows the dependence of the oscillation frequency on the oscillation amplitude for two different traps. In Fig. 4.1, a), a red-detuned dipole trap of 170 nW, corresponding to a 1 mK deep trapping potential, creates a Gaussian profile in the radial direction with a mode waist of $w_0 \approx 29\,\mu$m. The trap is slightly anharmonic, owing to the Gaussian profile indicated by a small change of the oscillation frequency with changing oscillation amplitude (for a harmonic oscillator the oscillation frequency should be constant with changing amplitude). The radial oscillation frequency changes from ≈ 4.1 kHz to ≈ 3.7 kHz for a normalized transmission below 0.1 up to 0.7. With decreasing coupling strength the number of coincidences increases (from black to light grey) due to the larger transmission when the cavity is empty.
When superimposing the red-detuned dipole trap with an additional blue-detuned torus trap of 250 nW, corresponding to an additional 0.5 mK radial trapping potential, the trap becomes more anharmonic. As shown in Fig. 4.1, b), the oscillation frequency changes from ≈ 5.5 kHz to ≈ 3.4 kHz when relaxing the restriction on the transmission from 0.05 to 0.7 of the empty cavity transmission. The obtained frequencies for both traps are consistent with the estimated trap frequencies of Fig. 3.8.

### 4.3.2 Engineering the atomic oscillation

The different trapping potentials of blue- and red-detuned dipole traps enable us to individually influence the radial and the axial atomic motion. In

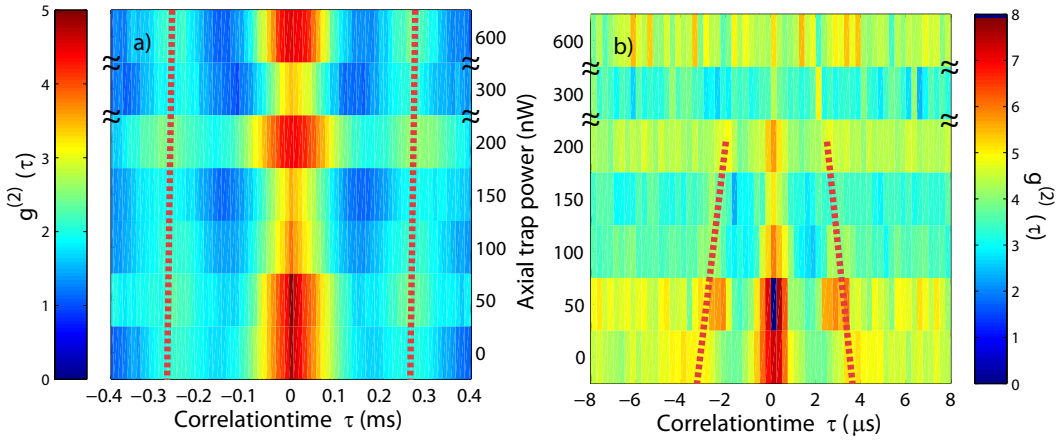


**Figure 4.3:** Influence of the axial trapping potential on the atomic oscillation. a) The radial oscillation frequency is not affected by a changing axial confinement. No shift of the radial oscillation frequency is visible when changing the additional axial trapping power from 0 to 600 nW. The normalized transmission is 0.1 and the probe power is 1.5 pW. b) In the same measurement the axial oscillation frequency changes from ≈ 300 kHz (0 nW additional axial confinement) to ≈ 440 kHz (200 nW additional axial confinement). An additional axial trapping potential above 200 nW results in a disappearance of the axial oscillation in $g^{(2)}(\tau)$.

the setup, as presented in Sec. 3.1.4, the radial potential can be manipulated using the blue-detuned torus mode while only marginally changing the Stark shift. For the following measurements the red-detuned dipole trap is set to 170 nW. Figure 4.2 shows the dependence of the oscillation frequency on the radial trapping potential for an ensemble of ≈ 100 single-atom traces for each configuration. Here the coupling strength is strong corresponding to a normalized transmission of 0.1, but the results remain qualitatively unchanged for all different coupling strengths. The radial oscillation frequency changes from ≈ 4.4 kHz to ≈ 5.5 kHz (see Fig. 4.2 a)) when the torus power increases from 0 nW to 400 nW. As the atomic oscillation amplitude is restricted by the postselection process (see Sec. 3.1.9) the change of the oscillation frequency comes from an oscillation with the same amplitude but in a changed trapping potential.
The interpretation is not straightforward, as the oscillation depends on the radial and the axial position as well as the overlap of the probe mode with the dipole trap modes (see Fig. 3.5). For example, Fig. 4.2 b) shows the axial oscillation frequency changing from ≈ 330 kHz to ≈ 500 kHz when the torus power is increased from 0 to 400 nW. The faster oscillation for higher powers of the torus trap indicates an axial oscillation closer to the cavity axis. Therefore, the atom oscillates in a region with a deeper axial trapping potential. These experiments are repeated at a probe power of 1.5 pW (not shown) with the same qualitative results.

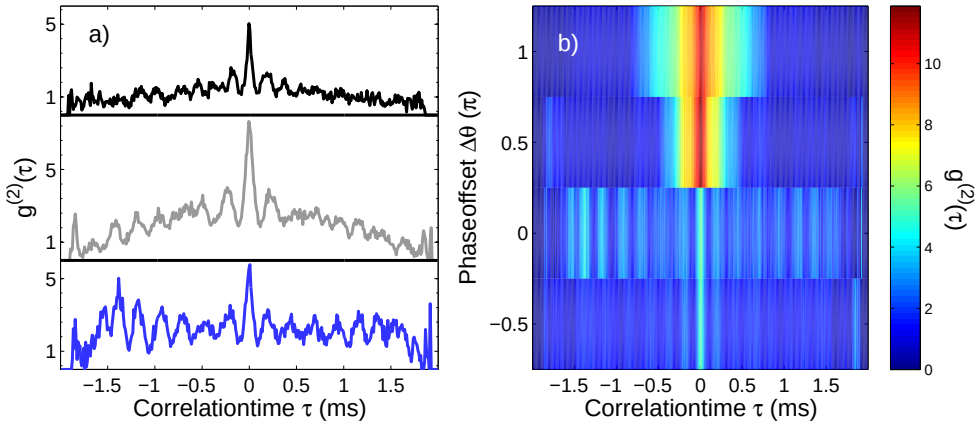


**Figure 4.4:** Locking the phase of the atomic motion to an external driving field. a) The radial atomic motion is observed for 3 milliseconds. For a torus potential constantly on a high level (black line) only one oscillation is clearly visible before the oscillation is washed-out. The atomic motion can be driven externally such that the oscillation becomes more stable (grey line). The bending of the correlation function indicates heating of the atom which is accompanied with an increased photon flux. When the external driving is phase-locked to the atomic motion (blue data) the coherence of the oscillation is significantly enhanced oscillating over the full recording time. b) The coherence of the oscillation increases only when the phase is adjusted correctly ($\Delta\Theta = 0$). For a wrong phase adjustment large photon bunching indicates heating of the atom on a timescale of $\approx 1$ ms.

A complementary way to manipulate the atom's oscillation frequency is to change only the axial trapping potential. For this purpose the blue-detuned $TEM_{00}$-mode at 772 nm, 3 FSR apart, is used. Measured at 1.5 pW probe intensity and for a normalized transmission of 0.1, Fig. 4.3 b) demonstrates how the axial frequency shifts from $\approx 300$ kHz to $\approx 440$ kHz for increasing axial laser power from 0 to 200 nW. Above 200 nW of additional axial trapping power the axial motion is no longer visible in $g^{(2)}(\tau)$. The radial frequency remains unaffected, as depicted in Fig. 4.3 a).

## 4.4 Externally driving the atomic oscillation

The coherence properties of the atomic oscillation are of interest to determine the quality factor of the atomic oscillator. This is encoded in the disappearance of the modulation of $g^{(2)}(\tau)$. The radial oscillation frequency of a single atom can be constant for milliseconds as shown in [Mau05a]. However, this is only true for parts of a single-atom trapping event. In general, the average of one hundred single-atom traces shows a coherence time on the order of only one oscillation period. In Fig. 4.4 a) (black curve) $g^{(2)}(\tau)$ is evaluated

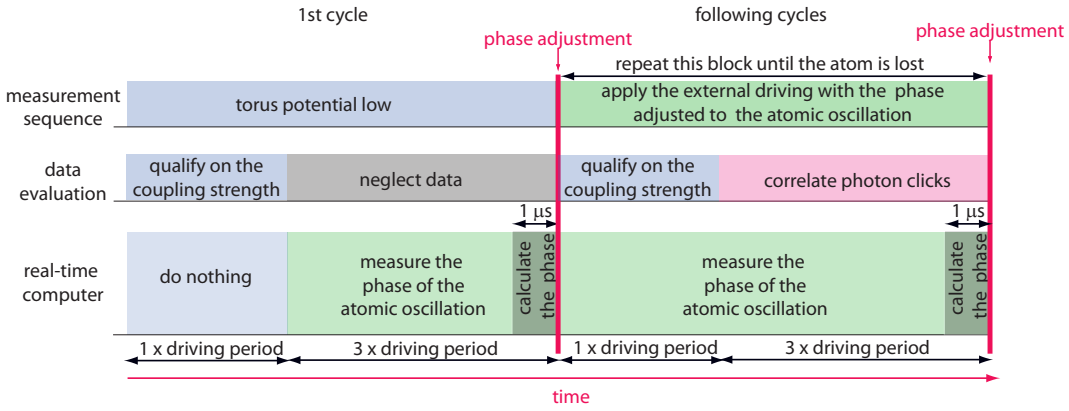


**Figure 4.5:** Scheme to lock the phase of an external driving with a predefined frequency to the atomic oscillation. The protocol is composed in cycles where each cycle has the length of four driving periods. During the first driving period the system evolves and the recorded transmission is used in the postselection process to ensure a certain coupling strength. In the next 3 periods (the probe intervals) the data is recorded to reveal the atomic trajectory from cross correlations. During the whole process the phase is measured and in the last $\mu$s of each probing interval the phase is calculated and readjusted. When the cycle starts for the first time after capturing an atom, the trapping potential is kept constant and the external driving begins after the phase is adjusted for the first time.

for a 1 mK deep, red-detuned dipole trap (170 nW) superimposed with a 0.5 mK deep, blue-detuned torus potential (250 nW). It shows a damping of the periodic modulation of $g^{(2)}(\tau)$ within one oscillation period. This is a direct consequence of the anharmonic trapping potential accounting for different oscillation frequencies as well as the Brownian nature of the motion which makes the oscillations to a large extent erratic.

In this section we show that the atomic oscillation properties can be controlled by modulating the intensity of the trapping potential periodically in time. Figure 4.4 a) (grey data) shows $g^{(2)}(\tau)$ when the intensity of the trapping potential is modulated with a sinusoidal frequency of 1.55 kHz. Switching the blue-detuned torus trap from 50 nW to 250 nW corresponds to an additional radial potential of 0.1 mK and 0.5 mK, respectively. It is superimposed with the 1 mK deep, red-detuned dipole trap. With respect to a constant torus trap of 0.5 mK (black data) the damping time of the radial oscillation increases and the oscillation is visible after three oscillations. However, the increase of $g^{(2)}(\tau)$ for small $\tau$ ($-1.5$ ms $\leq \tau \leq 1.5$ ms) is accompanied with an increased photon flux (not shown). It indicates heating of the atom where the atom's distance to the cavity center changes on a timescale of 3 ms.

To control the atomic oscillation without pushing the atom away from the region of strong coupling, the external modulation is kept at a fixed frequency and the phase of the driving field is locked to the atomic oscillation. A

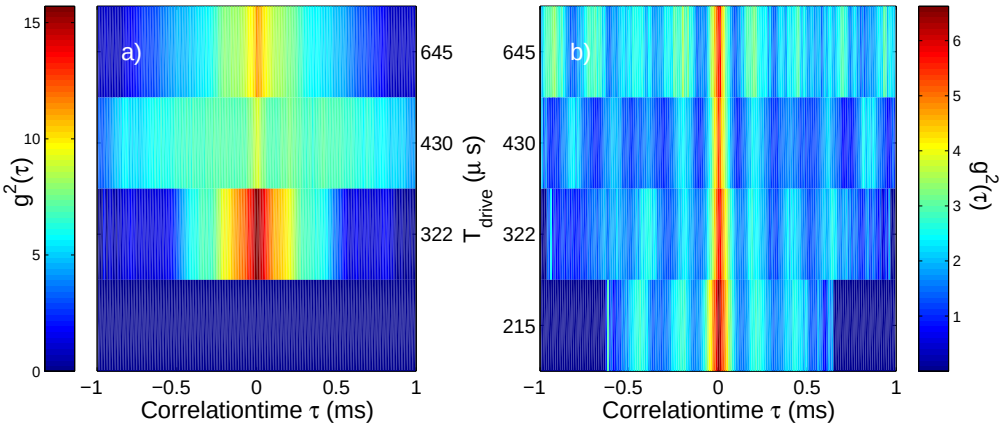


**Figure 4.6:** Phase locking for different driving frequencies ($1/T_{drive}$). a) A bad phase relation entails large photon bunching on timescales on the order of a millisecond. $g^{(2)}(0)$ can reach values of 16. b) For a well adjusted phase the atom is driven over the whole observation time. For a large correlation time the atomic oscillation frequency approaches the external driving frequency.

schematic of the procedure is depicted in Fig. 4.5. The sequence is separated in driving periods which are integer multiples of the typical atomic oscillation period. Each measurement cycle consists of four periods. The first period is used to ensure a certain coupling strength by postselection of the transmitted intensity (see Sec. 3.1.9). The data is recorded for evaluation only during the following 3 periods. During the first cycle the trapping potential is constantly at a low power and the atom is cooled in the axial direction via cavity cooling. The real-time computer (AdwinProII-technology) starts to calculate the phase of the atomic oscillation after the first period and continuously updates it until the end of the sequence. At the end of each cycle the phase relation between the external driving and the atomic oscillation is calculated and the driving is adapted to the new phase. This takes 1 $\mu$s where the real-time computer matches two sinusoidal functions ($90^o$ out-of-phase) to the arrival times of the single-photon events. The phase relation between atomic oscillation and driving, $\Theta$, is determined by the overlap of the detection events with the two sine-functions. In the following the phase of the driving field is matched to the atomic oscillation and a phase offset of $\Delta\Theta$ is added.
The blue line in Fig. 4.4 a) shows $g^{(2)}(\tau)$ where the phase of the external intensity modulation is adjusted to be in phase ($\Delta\Theta = 0$) with the atomic motion. No damping of the oscillation in $g^{(2)}(\tau)$ is visible during the complete time of the data collection. In addition the photon flux is not significantly enhanced (not shown) which would indicate a reduced localization as for the grey data. Fig. 4.4 b) shows the relation of the correlation function and the phase offset of the external driving. The oscillation is well driven only if $\Delta\Theta = 0$ (cor-

responding to the blue line in Fig. 4.4 a)). For a mismatch of the phase like $\Delta\Theta = \pi/2$ or $\Delta\Theta = \pi$, the atom is heated, causing large bunching peaks with $g^{(2)}(0) = 10$.
The experiment is repeated for sinusoidal driving pulses with different driving frequencies of 4.5, 3.1, 2.3 and 1.5 kHz. In Fig. 4.6 two cases for sinusoidal driving with bad (a) and good (b) phase adjustment demonstrate the influence of different driving frequencies. A bad phase adjustment happens in either of the two scenarios:
1. Adding a predefined phase shift of $\Delta\Theta = \pi$ when the atomic oscillation frequency, $f_{atom}$, and the external driving, $f_{drive}$, fulfill $f_{drive} = n \times f_{atom}$, where $n \epsilon N$.
2. Setting $\Delta\Theta = 0$ when $f_{drive} = (2n + 1) \times f_{atom}/2$.
The bad phase adjustment results in large and broad bunching peaks in the correlation with $g^{(2)}(0)$ as large as 16 (see Figure 4.6 a)). In contrast a good phase-adjustment is achieved for:
1. $\Delta\Theta = 0$, when $f_{drive} = n \times f_{atom}$
2. $\Delta\Theta = \pi$ when $f_{drive} = (2n + 1) \times f_{atom}/2$.
All examples for a well adjusted phase show an oscillation in $g^{(2)}(\tau)$ during the total recording time. Comparing the oscillation period for different driving frequencies at large correlation time, Figure 4.6 b) indicates that a slow driving frequency changes the atomic motion towards a slower oscillation frequency. For example, the fourth maximum of the oscillation in $g^{(2)}(\tau)$ is at $\tau \approx 0.95$ ms for a driving period of 645 $\mu$s and at $\tau \approx 0.85$ ms for a driving period of 430 $\mu$s. Another purpose of this technique would be to cool the atom. As the bandwidth of the locking technique, which is $\Delta BW \sim 1/\Delta t$, is limited by the observation time, $\Delta t$, the protocol should only enable a narrow-band cooling with a bandwidth of a few hundred Hz depending on the recording time.

## 4.5 Conclusion

In addition to the characterization of the atomic motion in the intracavity dipole trap, we have demonstrated here that it is possible to manipulate the atomic motion. We have individually influenced the radial and the axial oscillation frequency of the atom. This opens new control possibilities to engineer the atomic motion. Furthermore, we have controlled the oscillation properties of the atom, like the coherence time. Therefore we drove the atomic oscillation by modulating of the trap depth periodically in time with the phase of the driving locked to the atomic motion. The ultimate goal of this work is to control the atomic trajectory at will, steering the atom on any chosen orbit. However, a full control over the atomic motion is limited by the bandwidth of the locking protocol. This is in particular a limit for the purpose of cooling the atom. In contrast to high Q, harmonic oscillators, like an ion in a Paul trap

[Bus06], where a cooling scheme with a narrow bandwidth is sufficient to cool the ion a broad bandwidth cooling technique is necessary to cool the anharmonic, low Q oscillation of the atom. An extension of this work could be to measure the phase in parallel with the phase adjustment and the probing. This allows for a short observation time, $\Delta t$, and therefore for a broad bandwidth. However, this is not possible with the AdwinProII-technology used here due to the limited computational power. An improved performance is achievable by changing to very fast computational devices like field programmable gate arrays (FPGA).

# 5 Real-time feedback control of the atomic motion

The content of this chapter has partially been published in
A. Kubanek, M. Koch, C. Sames , A. Ourjoumtsev, P. W. H. Pinkse, K. Murr, and G. Rempe,
"Photon by photon feedback control of a single-atom trajectory,"
Nature 462, 898-901 (2009).

## 5.1 Motivation

As discussed in Sec. 4.4, a fast feedback is required to control the atomic motion inside the trapping potential when this motion is to a large extent chaotic, where the oscillation is perturbed by forces with random character like spontaneous emission. Moreover, to control the motion of a single atom in an anharmonic potential (as is the case here), where the oscillation period depends on the oscillation amplitude, an actuator operated at a fixed frequency is insufficient. A narrow-bandwidth locking technique, as used in Sec. 4.4, is not sufficient to cool such a low Q oscillator.
In a continuation of the previous chapter, we use the knowledge of the atomic position to manipulate the atomic trajectory. Realtime feedback is discussed where all 3 major steps, namely observation, processing and actuation, are done faster than the oscillation period. Previous work [Fis02] demonstrated an influence of feedback on the atomic storage time by using one and the same laser to probe the system as well as to act on it. However, as a change of the probe field also changes the forces on the atom, the achieved increase in storage time (from $300\,\mu s$ to $400\,\mu s$) could not conclusively manifest feedback control and cooling.
In [Lyn05] the probing and trapping was realized by two independent lasers. Simulations predict a good control over the atomic trajectory, e.g. forcing the atom on a circular orbit. However, the experimental implementation is difficult. The main reasons are the technological challenges of reacting faster than the decoherence of the system, while the photon flux is extremely low. This typically results in a low signal-to-noise ratio.
In this chapter a feedback circuit that acts $\approx 70$ times faster than the typical oscillation period reacts on the detection of single photons. This not only al-

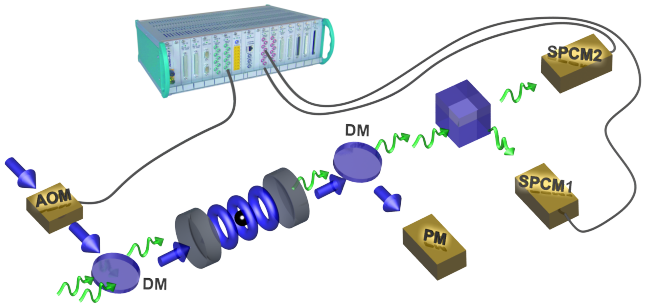


**Figure 5.1:** Overview of the feedback setup. The transmission of the near-resonant probe light (green arrows) through the coupled atom-cavity system is detected with two single-photon counting modules (SPCM1, SPCM2). A real-time processor estimates the atomic position from the number of photon clicks on both detectors. Based on this estimate the power of the toroidal trap is switched using an acousto-optic modulator (AOM). The dipole trap beam is superimposed with the probe light using a dichroic mirror (DM) and is detected behind the cavity using a photomultiplier (PM).

lows us to control the atom, but also proves the correctness of the information on the atomic trajectory discussed in the previous chapter. After demonstrating the experimental realization in Sec. 5.2, the feedback is optimized towards maximal storage times in Sec. 5.3. Numerical simulations complete the understanding of the systems dynamics in Sec. 5.4. In Sec. 5.5 the influence of feedback on the localization of the atom is investigated and Sec. 5.6 proves that the feedback cools the atomic motion. Section 5.7 summarizes the chapter and outlines future prospects.

## 5.2 Experimental realization

As discussed in Chap. 4, the atomic oscillation in the trap is rather erratic, indicated by a coherence time of $\approx 200\,\mu s$ for the radial oscillation. Therefore the main challenge for a successful feedback strategy is that it needs to work in real time, where real time means being faster than the decoherence time. The feedback circuit can be divided in three main steps: First, the atomic motion is continuously monitored by observing the probe beam transmission. Second, from the number of detected probe photons the position of the atom inside the cavity is deduced and, based on this information, a decision is made. Third, the motion of the atom is actuated by changing the dipole trap potential. A simple schematic of the experimental realization is depicted in Fig. 5.1. In

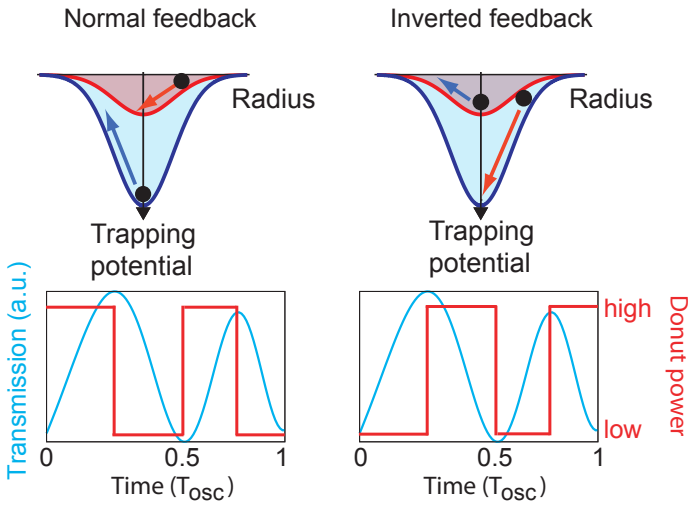


**Figure 5.2:** Two different feedback strategies. The normal feedback (left column) switches the trapping potential to a deep value when the atom moves away from the cavity axis, and to a low value otherwise. For the inverted feedback (right column) the switching process is inverted.

the following each individual step of the feedback loop is discussed in detail beginning with a short description of the parameter regime.

### 5.2.1 Parameter regime for feedback

As in Chap. 4 we work with the detunings $\Delta_c/2\pi = 100$ kHz and $\Delta_a/2\pi = 20$ MHz. Here, the overall photon flux is the highest and the contrast between well and badly coupled atoms is the best for atoms with an intermediate coupling strength between $0.2 < g/g_{max} < 0.6$ (see Fig. 2.2). For a probe power of 1 pW a well coupled atom induces a drop in transmission of the probe beam from 1 photon/$\mu$s (for an empty cavity) to values as low as 0.03 photons/$\mu$s. Very well coupled atoms do only marginally modulate the transmission. For those detunings cooling is efficient in the axial direction, and with the relatively high probe power of 1 pW the radial losses are dominant. Besides the slower, radial oscillation frequency this is the reason why the feedback is implemented for the radial direction of the atomic motion. Another advantage of the chosen parameters is that fluctuations in the effective detuning, e.g. due to a change of the Stark shift, do not critically influence the axial cavity cooling.

### 5.2.2 Different feedback strategies

We have implemented two different strategies to realize feedback on the radial motion of the atom which are both illustrated in Fig. 5.2. Both strategies change the power of the trapping potential when the atom is registered at a

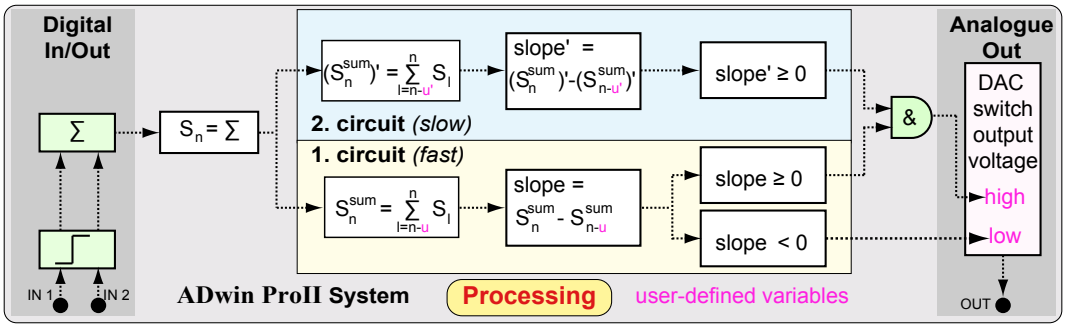


**Figure 5.3:** Principle of the real-time processing in the feedback loop.

turning point. The most intuitive way to reduce the kinetic energy of the atom is so-called normal feedback. The atom is accelerated by the potential when moving towards the cavity center. To minimize the energy gain, the potential is kept low. The kinetic energy is reduced whenever the atom moves away from the center. To maximize the cooling, the trapping potential is increased to its maximum. The difference of the two potential depths is proportional to the amount of kinetic energy removed from the atom in each cycle. In the so-called inverted feedback, the sense of switching is inverted, increasing the kinetic energy of the atom to expel it from the cavity. We apply in both schemes a "bang-bang" strategy [Ste04], [Ste06] which implies a rapid switching between two extreme values of the actuator potential.

### 5.2.3 Real-time processing

The high contrast of the probe beam transmission for a well and a badly coupled atom allows a fast estimation of the atom's radial position. To apply feedback we need to know whether the atom is moving towards the cavity axis or away from it. The real-time computer system (see Sec. 3.3) estimates which of the two situations applies by counting the number of photons detected during two consecutive time windows of equal duration $T$, called exposure time in the following. The two situations are distinguished by the difference of the number of photons registered in the first interval, $n_1$, to the number of photons in the second interval, $n_2$. An increasing flux of photons, $n_1 < n_2$, indicates that the atom moves outwards radially from the cavity axis, while a decreasing flux, $n_1 > n_2$, indicates that the atom moves inwards to the cavity axis. The potential is then switched according to the applied feedback strategy.
Here, a more detailed description follows. A sketch of the processing is given in Fig. 5.3. The digital pulses from the SPCMs are fed into a digital input/output board (DIO, module ProII-DIO32-TiCo RevE03). On this DIO board a field programmable gate array (FPGA) performs an edge detection and counts the number of events $\Sigma$ since the last query from the host processor (T11 module with ADSP-TS101S TigerSHARC processor). The host processor continuously

runs a main loop, which is treating the received data. The repetition time $\tau$ at which this loop is executed depends on its complexity and is a multiple of the inverse clock rate (1/300 MHz). Every time the loop is executed the index $n$ enumerating the iteration number is incremented. The $n$-th iteration of the loop starts by querying the number of clicks $S_n = \Sigma$ counted since the last loop from the DIO board. In order to increase the signal-to-noise ratio a number $u$ of successive values of $S_n$ are summed. The result will be denoted as $S_n^{sum}$. This variable hence reflects a signal which has been integrated over an interval with a length of $T = u \cdot \tau$. In the following the exposure time, $T$, is typically on the order of a few microseconds. By choosing the exposure time shorter than the radial oscillation but longer than the axial one the obtained information is only sensitive to the radial motion. From the integrated number of photon detections $S_n^{sum}$ we subtract the one delayed by $u$ loop cycles $S_{n-u}^{sum}$. The difference between these two values yields the change in the count rate, which is called *slope*. Depending on whether the *slope* is positive, negative or zero, a digital to analogue converter (DAC) sets the output voltage of an analogue output channel to a predefined high or low value.
The probe beam transmission for atoms close to the cavity axis is extremely low. Therefore, it would be optimal to continuously adapt the exposure time to the available photon flux. As a first step in this direction, we accounted for the changing photon flux by adding a second decision circuit. The first circuit has a short exposure time $T_{fast}$ and allows for a fast reaction when the photon flux is high. The second circuit has a longer exposure time $T_{slow}$ for the purpose of increasing the signal-to-noise ratio when the photon flux is low. This is the case for a well coupled atom in the centre of the cavity. For example, the first circuit is responsible for switching the torus trap to low power when the atom is returning towards the cavity, and the trap is switched back to high power only if both circuits register a positive slope.
The repetition time $\tau$ of the main loop depends on the complexity of the chosen algorithm. If only one circuit is determining the switching process the repetition time amounts to $\tau = 1.7\ \mu$s, corresponding to a maximal bandwidth of $\approx$ 590 kHz. This is much faster than the radial oscillation, which has a period of $360\,\mu$s, so feedback occurs in real time. If both circuits are in use it increases to $\tau = 2.0\ \mu$s. In that case typical values for $u$ are 5 for the fast and 20 for the slow circuit.

### 5.2.4 Actuator

As discussed in Chap. 4, the blue-detuned, toroidal dipole trap is an ideal tool to actuate the atomic motion in the radial direction. The repulsive force pushes the atom towards regions of low light intensity, i.e. to the center of the cavity. This has four benefits:
1. The dipole laser induces hardly any Stark shift when the atom is close to

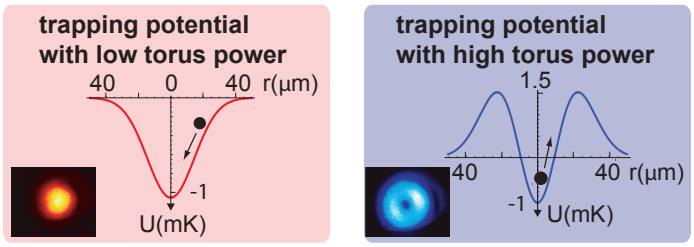


**Figure 5.4:** Trapping potential for high and low power of the torus trap. The trapping potential is plotted as a function of the radial distance from the cavity center, r, for low power (red box) and high power (blue box).

the cavity axis. Therefore, observing and acting are largely independent of each other.
2. The dipole laser controls the motion perpendicular to the cavity axis, which is the typical escape direction for a trapped atom in the chosen parameter regime.
3. The two perpendicular radial directions can be individually addressed by changing the intensity-ratio between the $TEM_{10}$- and $TEM_{01}$-mode.
4. It leaves the atomic motion along the cavity axis almost unperturbed and does not interfere with cavity cooling along this direction.
The blue torus trap is switched using an AOM between predefined levels with 50 nW corresponding to the "low" level and 800 nW to the high level. Together with the red trap the low level corresponds to a trap depth of 1 mK and the high level to a trap depth of 2.5 mK. The resulting trapping potentials are shown in Fig. 5.4.

### 5.2.5 Feedback reaction

A relevant factor in the experiment is the time needed to process the data. The feedback response is delayed by the exposure time $T$ plus a fixed delay of the switching process. An example of the switching process is shown in Fig. 5.5 for two different exposure times, $T = 10.2\,\mu$s (upper panel) and $T = 85\,\mu$s (lower panel). For $T = 10.2\,\mu$s most exposure intervals contain zero clicks. Nevertheless, the normal feedback strategy keeps the photon rate low, indicating good confinement of the atom. In contrast, the inverted feedback strategy leads to an increasing photon flux. For a longer exposure time, $T = 85\,\mu$s, the integrated signal becomes a smooth function (blue line), resulting in smoother switching. Concurrently, a large exposure time also delays the feedback, which can be seen by comparing the raw photon clicks (black data) with the integrated signal (blue data). To understand the influence of the exposure time on the performance of the feedback is one of the key features to understand the feedback mechanism. Qualitatively we observe that normal feedback keeps the atom well coupled for reasonably short exposure times, whereas it repels the

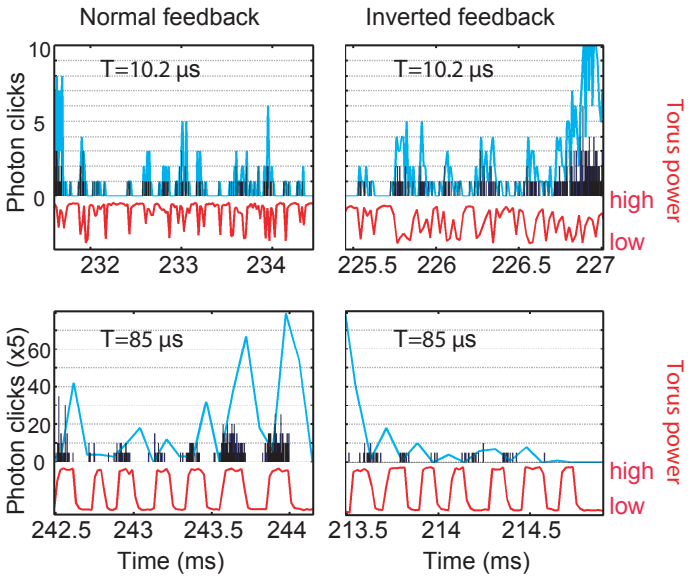


**Figure 5.5:** The two different Feedback strategies implemented in the experiment. For short exposure times, $T = 10.2\mu$s (upper panel), normal feedback (left column) keeps the photon flux low while inverted feedback increases the photon flux (right panel). This feature is reversed when the exposure time is increased, $T = 85\mu$s (lower panel). It can be explained by the delay of the integrated signal (blue line) compare with the raw photon clicks (black bars), which also delays the switching response (red line).

atom for longer exposure times. Inverted feedback shows the opposite characteristics.
Due to the limited photon flux, the amount of information obtained in one exposure interval strongly depends on the exposure time, $T$, especially when $T$ is short. In contrast to the idealized scenario in Fig. 5.2, the signal-to-noise ratio (SNR) at short exposure times can be extremely small. Assuming Poissonian distributed noise results in a noise power of $P_{noise} \approx \sqrt{P_{signal}}$. Therefore, counting the number of photons, $N$, per exposure interval gives a SNR of $N/\sqrt{N}$. With this definition the SNR drops below one for short exposure times and well coupled atoms, but still allows for a successful implementation of feedback. This low average SNR is possible as the photon flux increases whenever the atom attempts to leave the cavity. The minimum exposure time needed for a successful feedback is determined in Sec. 5.2.7.

### 5.2.6 Atomic storage probability

The atomic storage time is a good quantity for analyzing the performance of the feedback strategies. The average storage time, $ST$, is deduced by fitting an exponential decay, $f(t) = a \times \exp(-t/ST)$, to the atomic storage probability.

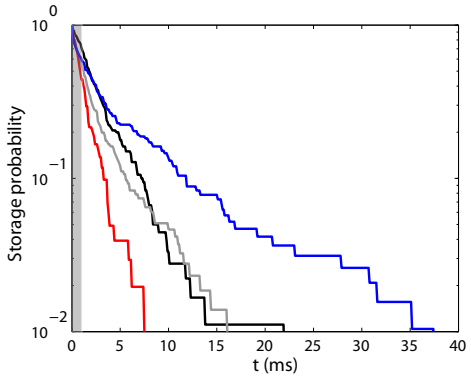


**Figure 5.6:** Atomic storage probability as a function of trapping times t. The experimental atom-loss dynamics without feedback (black line for torus power high and grey line for torus power low) is changed when feedback is applied. Whereas the slope of the exponential decay is less steep for normal feedback (blue line), a more rapid loss is present for inverted feedback (red line). The exposure time is chosen to be very short ($T = 10.2\,\mu$s).

The atomic storage probability is obtained by including all single-atom trapping events to determine the fraction of atoms which are still trapped after a time $t$, (trapped atoms at $t$/total trapping events). This is shown in Fig. 5.6. In the following the error bars for the average storage time are obtained from the fit including Poissonian distributed statistics (shot noise). At very short times there is a rapid loss of atoms, which are presumably those that are not injected in one of the central antinodes of the probe beam, but into a region where probe and trapping laser do not perfectly overlap. Therefore, the first millisecond of data is disregarded (grey shaded area), with 55 % of remaining atoms. Figure 5.6 confirms the qualitative observation of the previous section. The black and grey line demonstrate the characteristic exponential decay when the torus potential is constantly at high (600 nW) or low power (50 nW), respectively. Applying normal feedback (blue line) with a short exposure time of 10.2 $\mu$s leads to an increase in the storage time, while inverted feedback (red line) causes a reduction.

### 5.2.7 Phase dependence

Fig. 5.7 shows the average storage time as a function of the exposure time, $T$, ranging from a few microseconds to $T < 140\,\mu$s, or, in other words, from a small fraction of the oscillation period to about three-eighths of it. The experiment is repeated between 50 (for short average storage times) and 220 times (for long average storage times) for each data point. The dashed black and grey lines are the storage times without feedback where the torus trap is at low and high power, respectively. When $T$ is less than 7 $\mu$s the noise dominates

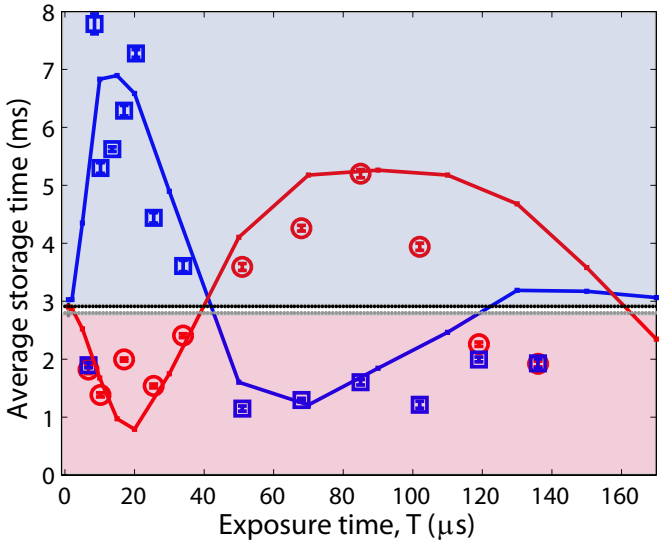


**Figure 5.7:** Average storage time plotted as a function of exposure time. The solid lines show the results of Monte Carlo simulations for the inverted (red) and normal (blue) feedback strategies. The corresponding experimental data points are plotted in the same colors. The dotted black and grey lines show the experimental storage time without feedback for high and, respectively, low toroidal-trap power, setting the boundary between feedback cooling (blue shaded area) and feedback heating (red shaded area).

the signal. This results in a heating of the atom and a decrease in the storage time shorter than the value without feedback (red shaded area), for both normal (blue data) and inverted (red data) feedback. Increasing the exposure time, however, increases the storage time, with a maximum at $T \approx 15\,\mu$s for normal feedback. This is remarkable, given that only a few photons have been detected. In contrast, applying inverted feedback with this exposure time leads to a storage time shorter than the value obtained without feedback. Here the atom is heated. Furthermore, inverted feedback turns into a cooling mechanism for longer exposure times, reaching a maximum at $T \approx 90\,\mu$s. The maximum storage time for inverted feedback is less than that obtained for normal feedback, although the switching process is less noisy here. This directly shows that it is important to apply the feedback before the atomic motion becomes unpredictable.

The experimental results are compared with Monte-Carlo simulations as described in [Sch08b, Fuh08]. To match the experiment we had to include an additional loss rate of $1/7$ ms$^{-1}$. The storage times are thus only well reproduced if a loss mechanism other than cavity-induced heating is added. We found out that the main reason for this loss is the off-resonant pumping of the atom into the dark hyperfine state, $F = 2$. This is confirmed by the in-

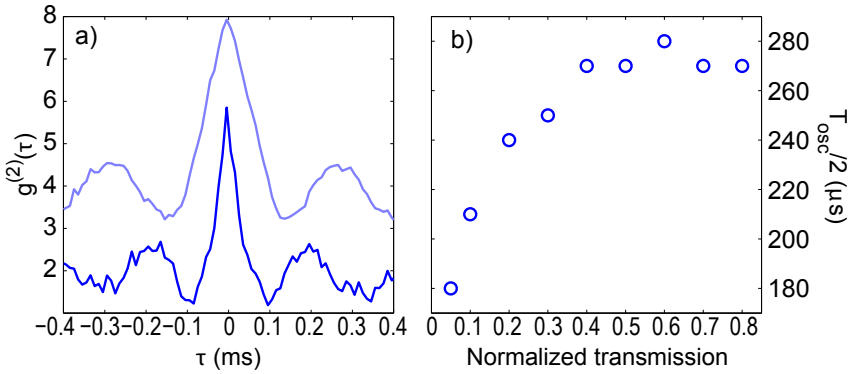


**Figure 5.8:** Intensity correlations of the probe beam transmission for atoms exposed to normal feedback. a) The photon correlation function, $g^{(2)}(\tau)$, is shown as function of the correlation time, $\tau$, for strongly coupled atoms (dark blue line) and weakly coupled atoms (light blue line). From the correlation function the oscillation period of the atom in the trap as well as the decoherence time of its oscillation ($\approx 200\,\mu$s) can be determined. The error bars (not shown) of the $g^{(2)}(\tau)$ data are typically less than 0.15. b) The dependence of the oscillation period on the normalized transmission characterizes the anharmonicity of the trapping potential.

crease of the storage time when adding a repumping laser perpendicular to the cavity axis. From the increase in the storage time without feedback, the additional loss rate is estimated to be between 1/5.5 ms$^{-1}$ and 1/14 ms$^{-1}$. A more detailed description follows in Sec. 5.3.1.

### 5.2.8 Comparison with intensity correlations

As was shown in Sec. 4.3, the oscillation period of the atom can be determined from photon-photon correlation measurements. Figure 5.8 a) shows the normalized photon correlation function when feedback is applied. The transmission is restricted to less than 0.05 of the empty cavity transmission. Then, the oscillation period is $2 \times 180\,\mu$s (dark blue line). For weakly coupled atoms, corresponding to a transmission of up to 0.6 times the empty cavity transmission, the correlation function shows an oscillation period of $2 \times 260\,\mu$s (light blue line). The dependence of the oscillation period on the localization is shown in Fig. 5.8 b). A harmonic potential would result in a horizontal line where the atomic oscillation frequency is independent of its amplitude or the coupling strength, respectively. Therefore it directly shows the anharmonicity of the trapping potential.
A comparison with Fig. 5.7 shows that the maximum average storage time of inverted feedback is at $90\,\mu$s corresponding to one quarter of the oscillation period for a well coupled atom. The transition of the normal feedback from cooling to heating (or for the inverted feedback from heating to cooling) happens with a characteristic time of $T \approx 45\,\mu$s when the reaction is delayed with

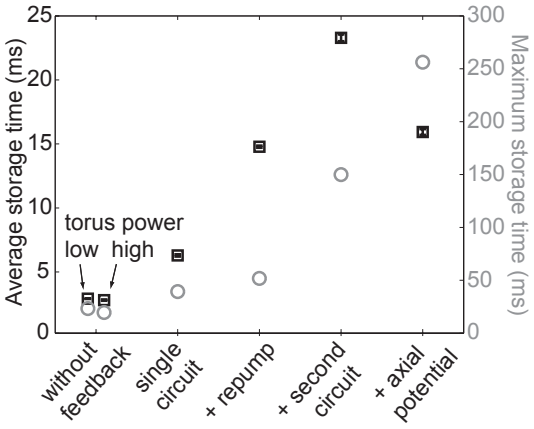


**Figure 5.9:** Experimental improvements. The observed storage time increases by successively adding different experimental techniques. For each step the average storage time (black squares) is plotted on the left and the storage time of the longest trace (gray circles) on the right. As references, measurements without feedback with constant low or high torus potential are shown. Normal feedback with one decision circuit results already in a clear improvement. Further improvements are achieved by adding a repumping laser, a second decision circuit and an additional axial confinement.

respect to the atomic oscillation by one eighth of the oscillation period for a well coupled atom. Therefore, the dependence of the system's response on $T$ when feedback is applied proves the consistency of the inferred information on the trajectory. By comparing the characteristic times the results also suggest that the feedback reacts already on small oscillation amplitudes keeping the atom well coupled. In addition, the random character of the atomic motion is visible in the damping of the correlation function, indicating a decoherence time of $\approx 200\,\mu$s. This also explains the reduced storage time when reacting with a delay of one quarter of an oscillation.

## 5.3 Optimizing the feedback protocol

This section reports how the feedback loop is optimized experimentally using a number of improvement steps, all aiming to further increase the storage time. All experiments operate at relatively high probe powers of 1 pW as this is a promising regime, e.g., to observe quantum nonlinear effects (see Chap. 6 and Chap. 7). So far these experiments suffered from short storage times as increasing probe powers lead to an enhanced heating.
Fig. 5.9 shows a progression of different improvements in terms of the average (black squares, left axis) and maximum storage time (grey circles, right axis). As a reference the first data points on the left correspond to a trapping potential kept constant at a high or low level without applying feedback. The

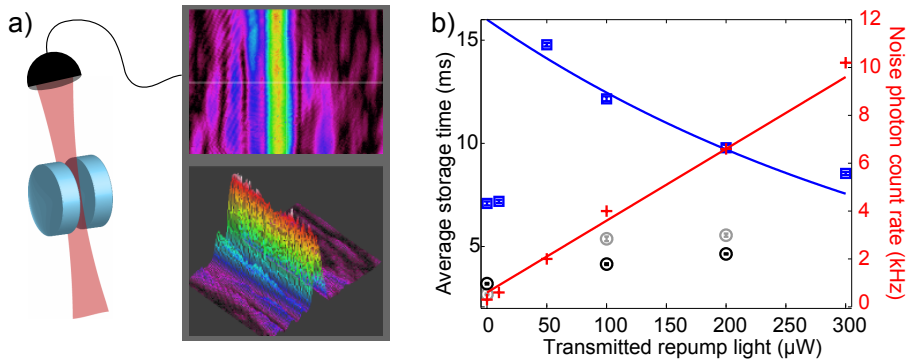


**Figure 5.10:** Influence of a repumping laser. a) CCD image of the transmitted repump light through the side of the cavity. The clipping of the beam is clearly visible. b) Influence of a repumping laser on the storage time. The storage time without feedback increases by about a factor of two in the presence of the repumping light, saturating for powers above 100 $\mu$W (black and grey circles for high and low torus potential, respectively). When normal feedback is applied (blue squares), an increase of the storage time is followed by a decrease for repumping powers above 50 $\mu$W due to an enhanced noise-photon rate on the detectors (red crosses and red line, right vertical axis).

average storage time in both cases is below 3 ms with a maximum storage time of 23 ms, limited by the radial losses. Activating the real-time control of the atom with one decision circuit and an exposure time of $T \approx 15\,\mu$s significantly increases the storage time by more than a factor of two. The longest trace observed reaches 40 ms. From comparison with simulations the main additional loss mechanism turns out to be off-resonant pumping of the atom to the 'dark' hyperfine state $5S_{1/2}, F = 2$. Therefore an additional repumping laser, aligned perpendicular to the cavity axis, is used to bring these atoms back to $5S_{1/2}, F = 3$. The feedback protocol can be improved further by dynamically adjusting the exposure time to the available flux of photons depending on the coupling strength. As a last experimental test an additional axial confinement reduces atom losses in the axial direction. In summary, the average storage time improved to almost 25 ms, with the longest trace of about a quarter of a second, exceeding the limit without feedback by more than a factor of 5. In the following each optimization step is discussed in more detail.

### 5.3.1 Compensating for off-resonant pumping

An important loss mechanism of the atom from the cavity is off-resonant optical pumping of the atom into the hyperfine state $5S_{1/2}, F = 2$ which is not coupled to the cavity probe field. Imperfect circular polarization can off-resonantly excite the atom to $5P_{3/2}, F' = 3$ from where it can decay into $5S_{1/2}, F = 2$. As feedback operates at moderately high probe power, this loss

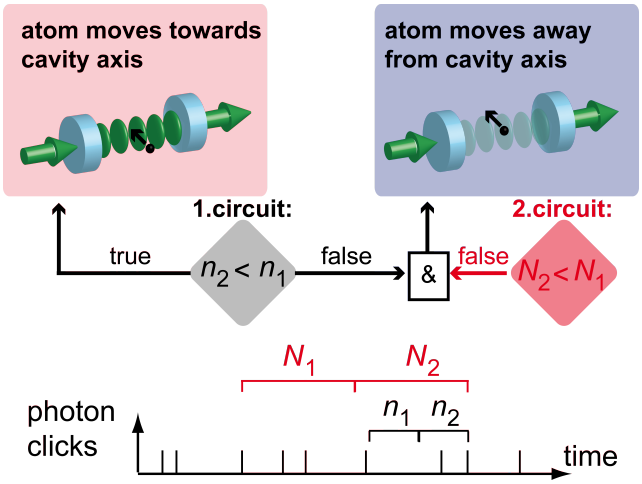


**Figure 5.11:** Double-circuit feedback. The exposure time is adjusted to the variable photon flux by adding a second circuit. It allows for an advanced estimation of the atomic position when the atom is well coupled. Here, the photon flux is low and the signal-to-noise for the decision when the atom starts to move away from the cavity axis is increased by the second circuit.

mechanism becomes more and more important for increasing storage times. It is compensated by an additional repumping laser which resonantly excites the atom from $5S_{1/2}, F = 2$ back to $5P_{3/2}, F = 3$. This repumping laser is aligned perpendicular to the cavity axis and is focused between the mirrors. Clipping of the beam off the edges of the cavity mirrors is unavoidable due to the geometry of the cavity setup. The laser is focussed from a distance of about 20 cm outside the vacuum chamber through the side of the cavity, which forms a tight slit of 60 $\mu$m when viewed from the side. The profile of the transmitted repumping beam shows a diffraction pattern as depicted in Fig. 5.10, a). The clipping leads to light scattering into the cavity mode and consequently to an increased noise photon rate on the detectors. The photon count rate as a function of the repumping laser power is shown in Fig. 5.10 b) (red crosses, right axis). The count rate of noise photons ($CNP$) on the SPCMs increases linearly with increasing repumping power ($P_{repump}$), $CNP = 0.03$ [kHz/$\mu$W] $\times P_{repump} + 0.6$ [$\mu$W] (red line).
In Fig. 5.10 b) the average storage time as a function of the repumping power is shown on the left vertical axis. When no feedback is applied (black and grey circles, for torus power high and low, respectively) the storage time increases by roughly a factor of two. Already a repumping intensity of 100 $\mu$W, corresponding to a power density at the atoms location of $\approx 8$ mW/cm$^2$, is sufficient to saturate the repumping transition. From the increase in the storage time without feedback, we can estimate that the additional loss rate due to off-resonant pumping into the $5S_{1/2}, F = 2$ hyperfine ground state is between 70 Hz and 180 Hz without the repumping laser. Simulations suggest a rate of

140 Hz, matching the experimental observations.
Testing the effect of a repumping laser in combination with feedback is more complex since there are two competing mechanisms. On one hand, the storage time increases with increasing repumping power, saturating at a certain intensity. On the other hand, increasing the repumping power raises the noise-photon rate which leads to false decisions in the feedback loop. These counteracting effects are observed in the experiment as shown in the data (blue squares) in Fig. 5.10 b). A maximum of the average storage time is found for a repumping power of 50 $\mu$W. When increasing the repumping power further the storage time starts decreasing since the position estimation of the feedback loop is perturbed more and more by noise photons from scattered repumping light. An exponential function (blue line) reproduces the additional loss. This implies that if it would be possible to reduce the noise photons we could still gain in average storage time.

### 5.3.2 Double-circuit feedback

The optimal exposure time $T$ depends on the available photon flux corresponding to the actual atom-cavity coupling strength. The feedback protocol would improve further by dynamically adjusting $T$. The main problem arises when the atom is well coupled and the flux of information is extremely low. Therefore, as a first step, the dynamics of the changing photon flux are compensated by a second circuit for the position estimation (see Sec. 5.2.3). A simplified scheme of the idea is shown in Fig. 5.11. The exposure time of the fast circuit is $T_{fast} = 10\,\mu$s and of the slow circuit $T_{slow} = 40\,\mu$s. To switch the torus trap to low power the outcome of only the fast circuit is sufficient ($n_1 > n_2$). But for switching to high power both circuits need to register ($n_1 \leq n_2$). Here, the atom is likely to be close to the cavity axis and therefore the photon flux is low. The average storage time increases to about 24 ms and the longest trapping times exceed 150 ms. The overall improvement factor of the storage time with feedback (24 ms) relative to that without feedback (6 ms) is four.

### 5.3.3 Axial confinement

Once the radial losses are reduced by feedback control, losses along the axial directions should start to play a role. In order to minimize them, an additional axial confinement is provided by the blue detuned $\mathrm{TEM}_{00}$-mode at 772 nm. The nodes of the 772 nm mode coincide with the antinodes of the 780 nm probe beam at the center of the cavity (see Fig. 3.5). But for increasing distance from the cavity center along the axis, the different wavelengths cause a mismatch. In these regions feedback does not work properly and pushes the atom out of the probe beam, resulting in a reduced average storage time of about 16 ms, as shown in Fig. 5.9. However, it also results in an increase of the maximal

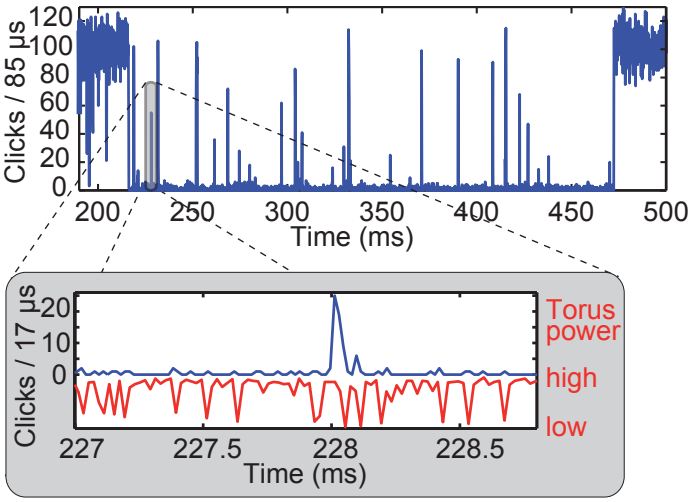


**Figure 5.12:** Example of a long trace, where the atom is trapped for about a quarter of a second. This is achieved using all steps of improvement, namely a feedback algorithm with two circuits, a repumping laser as well as an additional axial confinement.

storage time to about a quarter of a second since atoms entering the cavity close to the center are additionally confined. An example trace of an atom stored for a quarter of a second is shown in Fig. 5.12.

## 5.4 Monte Carlo simulation

To optimize the performance of the feedback and to understand its limitations, we performed Monte-Carlo simulations (see [Sch08b, Fuh08]). In this section we investigate the storage time under the influence of different parameters like the switching condition, the symmetry of the torus trap, the detection efficiency and the count rate of noise photons. All simulations include only one decision circuit.

### 5.4.1 Feedback strategies

Figure 5.13 shows the simulated average storage time as a function of the exposure time $T$ for three different normal feedback strategies. In the first case (blue, solid line), the torus trap is switched to a high potential under the condition $slope \geq 0$ and to a low potential under the condition $slope < 0$. In the second case (grey, dotted line) the condition for switching to the high (low) potential is $slope > 0$ ($slope < 0$). And finally, in the third case (black, dashed line), the torus potential is switched high for $slope > 0$ and low for $slope \leq 0$. Even though the difference between these algorithms lies only in handling the case $slope = 0$ and seems rather small, the effect on the storage time is dra-

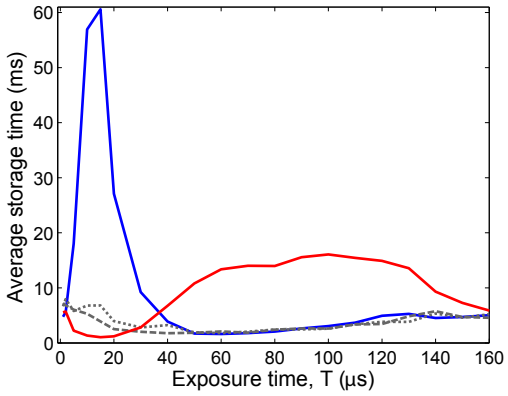


**Figure 5.13:** Influence of the switching condition on the feedback efficiency. The three different normal feedback strategies discussed in the text lead to different storage times. Here, we assumed an overall detection efficiency $\eta = 0.05$ and a total dark count rate of 0.5 kHz. A significant increase in the storage time is observed only for switching to a high (low) torus potential for $slope \geq 0$ ($slope < 0$)(blue line). Inverted feedback (red line) shows an increased storage time for longer exposure times. The storage time does not significantly increase for the other two normal feedback strategies, like switching to high (low) torus potential for $slope > 0$ ($slope < 0$) (grey dotted line) or for $slope > 0$ ($slope \leq 0$) (black dashed line).

matic for short exposure times where the decision process is based on only very few detected photons. We observe that only the first feedback strategy leads to a significant increase of the storage time. Our explanation for this behaviour is that atoms which start to move away from the cavity axis (the condition under which we have to increase the radial potential) produce only a very weak signal (see Fig. 2.2). In this case and for short exposure times, $T$, the zero-photon events are the most likely for atoms near the cavity axis. Hence, if $n_1 = n_2 = 0$ the atom could already be moving away from the axis, in which case it is prudent to switch the torus trap to high power. Therefore, it is favorable to switch on the high torus potential already when the transmission drops to zero that is under the condition $slope = 0$. For longer exposure times, a sufficiently large number of photons is detected per interval, thus eliminating the difference between the three feedback strategies. For completeness the red line shows simulations when inverted feedback is applied.
It is also obvious from Fig. 5.13 that the storage time crucially depends on $T$ (blue line), as discussed in Sec. 5.2.7. The simulation shows maximal storage times for normal feedback of almost 60 ms at an exposure time of approximately 15 $\mu$s which will be used in the following. Inverted feedback achieves almost 20 ms at 90 $\mu$s.
The used parameters are adjusted to the experiment with a detection efficiency of $\eta = 0.05$ and a count rate of noise photons of 0.5 kHz. The difference to the experiment is that we assumed no losses due to off-resonant pumping.

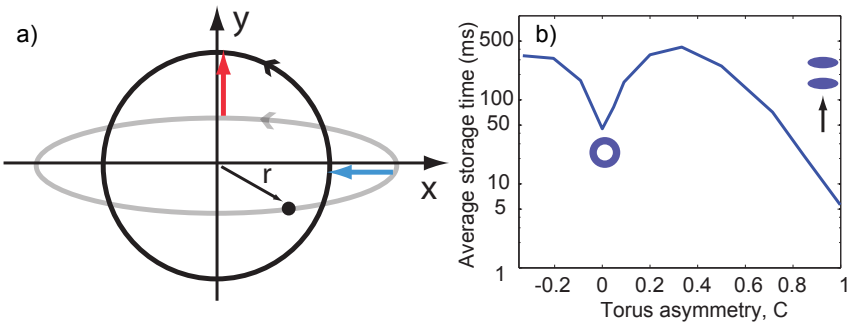


**Figure 5.14:** Influence of the torus asymmetry on the storage time. a) Schematic description of cooling an elliptical trajectory with a radial symmetric probe and actuator. While the motion is cooled along the large major axis, x, it is heated along the small major axis, y. This results in a circular orbit. b) The storage time improves from $\approx 5$ ms for a $TEM_{01}$-mode ($C = 1$) by a factor of 10 for a perfectly symmetric torus ($C = 0$). A further increase by another factor of 10 is achieved when the symmetry is broken for $C \approx 0.2$, ($\eta = 0.05$, dark count rate 0.5 kHz).

### 5.4.2 Radial symmetry

Since the $TEM_{00}$-mode which is used to probe the atomic motion is radially symmetric, the probing is only sensitive to the radial position of the atom and not to its azimuthal component. In addition, the simulations presented above have assumed a radially symmetric torus potential, i.e. a balanced superposition of the $TEM_{01}$ and the $TEM_{10}$-mode, which preserves the angular momentum of the atomic motion. This suggests that our feedback tends to force the atoms on circular trajectories which cause a constant transmission through the cavity and, hence, are no longer affected by the feedback. Figure 5.14 a) illustrates this fact. Only the large major axis, $x$, of an ellipsoidal motion (grey line) is cooled, while the atom is heated in the perpendicular direction, $y$. The reason is that an increasing radius, $r$, coincides with an increasing distance along the x-direction, but also with a decreasing distance in the y-direction. As the coupling strength and with it the transmitted photon flux changes with $r$, a perfectly adjusted feedback only works in the x-direction (blue arrow) while it is inverted in the y-direction (red arrow).
This unwanted effect can be overcome by unbalancing the intensities of the $TEM_{01}$- and $TEM_{10}$-modes, thus breaking the rotational symmetry of the torus potential. An alternative way would be to resolve the atomic motion with higher-order, non-symmetric probe modes. Figure 5.14 b) shows the average storage time as a function of the symmetry of the torus potential defined by the contrast $C = (I_{01} - I_{10})/(I_{01} + I_{10})$, where $I_{XY}$ is the intensity of the respective $TEM_{XY}$-mode. A value of 0 corresponds to a perfectly symmetric potential, 1 to a $TEM_{01}$-mode. With an overall photon detection efficiency $\eta = 0.03$, a count rate for the noise photons of 0.5 kHz and an exposure time

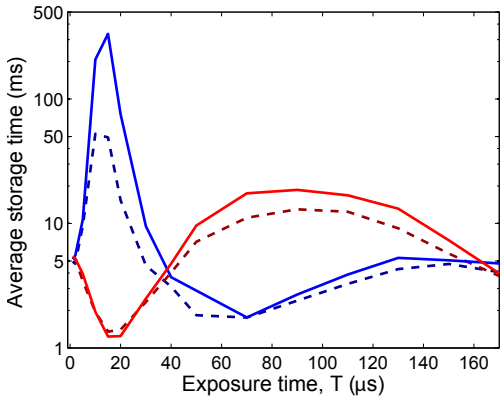


**Figure 5.15:** Influence of the noise photon count rate. Including the noise count rate of approximately 7.5 kHz from our experiment (dark blue, dashed line), we observe a decrease of the storage time by almost a factor of 10 compared to the case when only detector dark counts (0.5 kHz) are accounted for (light blue, solid line). When inverted feedback is applied the storage time also decreases for an enhanced count rate of noise photons (red lines).

of 15 $\mu$s we observe a storage time of 50 ms for $C = 0$. For $0 < C < 0.6$ an increase of the storage time compared to the symmetric potential is observed with a maximum of about 400 ms. Therefore, the experiments are performed with an asymmetric torus potential with a contrast of $C = 0.2$ corresponding to a $TEM_{01}$-mode 50 % stronger than the $TEM_{10}$-mode.
Simulations are also performed for $C < 0$ where $-1$ corresponds to a $TEM_{10}$-mode. It shows a similar behavior with a slightly reduced storage time for the asymmetric potential. The difference comes from the orientation of the asymmetric potential with respect to the direction of injection of the atoms (indicated as black arrow). Best results are obtained when the $TEM_{01}$-mode which is aligned with the atomic injection is more intense.

### 5.4.3 Signal-to-noise issue

A major issue is the signal-to-noise ratio of the detected photon flux. As the experimentally observed photon flux is as low as 0.03 photons per microsecond for a well coupled atom, it is not only the unavoidable shot noise but also stray light and detector dark counts that influence the performance of the feedback. In Fig. 5.15 the average storage time is plotted against the exposure time using an asymmetric torus potential of $C = 0.2$ as used in the experiment (blue, solid line). As in the previous simulations the only noise source (apart from shot noise) is the total dark count rate of the detectors of 0.5 kHz. However, in order to compensate for pumping to a dark hyperfine state, we have to add a repumping laser perpendicular to the cavity axis which will cause an increase of noise photons on the detector. The dark blue, dashed line in Fig. 5.15

shows the average storage time with the same parameters as before but with an increased noise level of 7.5 kHz. Then, the average storage time decreases by almost one order of magnitude. The corresponding results for inverted feedback are shown in red colors. In conclusion it is crucial to minimize the noise level on the detectors for a good performance of the feedback.

## 5.5 Atomic localization

So far, the only way to quantify the effect of feedback was the storage time of the atom. Another important piece of information is the atomic localization. Especially for the purpose of spectroscopy [Boc04, Mau05b, Sch08c], a good atomic localization is important to guarantee a strong atom-cavity coupling with small fluctuations of the coupling strength. In this section we quantify the effect of feedback on the atomic localization by correlation and transmission measurements. Localization and temperature is extracted by comparison with simulations.

### 5.5.1 Localization encoded in the transmission

The effect of feedback on the atomic localization is inferred from the average transmission in the probe intervals in switching measurements (see Sec. 3.1.9). Figure 5.16 a) shows the transmitted light as a function of the coupling strength, $g$. $g$ is encoded in the transmission during the qualification intervals and normalized to the transmission of the empty cavity (see Sec. 3.1.9). As expected for measurements on resonance with the empty cavity, the transmission increases with decreasing coupling strength. The black and grey data show the results without feedback for low (50 nW) and high (250 nW) torus power, respectively. In the following the effect of normal (blue data) and inverted feedback (red data) is investigated with one (diamonds) and two (squares) decision circuits. The single circuit strategies perform at $T = 17\,\mu$s, the two circuit strategies at $T_{fast} = 10\,\mu$s and $T_{slow} = 40\,\mu$s. Normal feedback with one and two decision loops both decreases the transmission significantly for all coupling strengths compared to the cases without feedback. Therefore the atomic localization improves. In contrast, when inverted feedback is applied the transmission increases and the atomic localization spreads out.
The grey line corresponds to simulations at low torus power without feedback. The general agreement with the experiment is good but the transmission is too high. The simulation for normal feedback (blue line) agrees well with the experiment. The experimental data deviate from the simulation only for a normalized transmission above 0.7. Differences between simulation and experiment include:
1. While the experiment runs for a predefined sequence length, the simulation

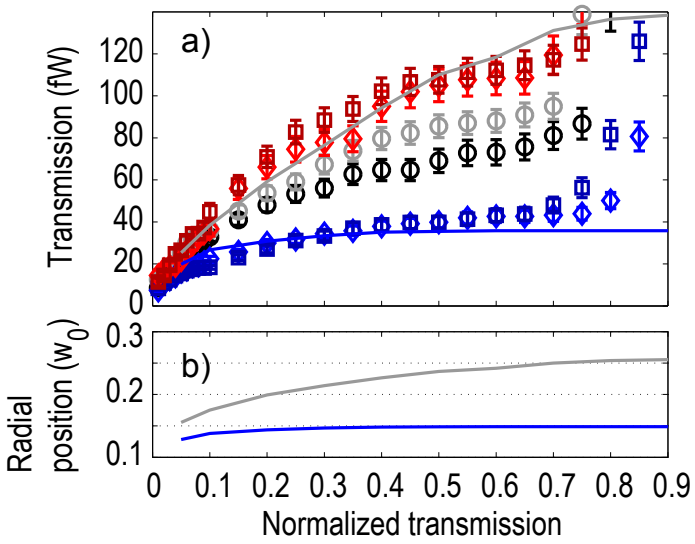


**Figure 5.16:** Effect of feedback on the atomic localization encoded in the transmission. a) The transmission in the probe intervals is plotted as a function of the normalized transmission in the qualification intervals (see text). For all measurements the transmission drops with decreasing normalized transmission. The transmission without feedback is shown as black and grey data for high and low torus potential. Applying normal feedback (dark blue squares with one exposure circuit and light blue diamonds with two circuits) reduces the transmission for all coupling strengths while inverted feedback enhances the transmission (dark red squares with one exposure circuit and light red diamonds with two circuits). The simulation for low torus power (grey line) shows a higher transmission than the experiment and the simulation of normal feedback with one exposure circuit (blue line) agrees well with the experiment. b) As the simulation includes the full atomic trajectory the radial position of the atom is plotted in units of the waist $w_0$ depending on the coupling strength. It shows a localization that is almost two times better when feedback is applied compared to no feedback.

always stops immediately when the atom is lost.
2. In the experiment the qualification of the coupling strength is determined in the two neighboring qualification intervals (see Sec. 3.1.9), in the simulation it is done in the probe interval itself.
As the full atomic trajectories are known in the simulations, the obtained transmission can be translated into a radial localization. Figure 5.16 b) demonstrates that feedback helps to keep the atom close to the cavity axis, with an average excursion of less than 4.5 $\mu$m (blue line). This is a factor of almost 2 better than without feedback (grey line).
Comparing the average atomic localization with the trapping potential (Sec. 3.1.8) at a radial position of 4.5 $\mu$m and 7.8 $\mu$m discloses upper limits for the temperature of the atom. Without feedback an excursion of 7.8 $\mu$m corresponds to 780 $\mu$K and normal feedback reduces this limit to 280 $\mu$K.

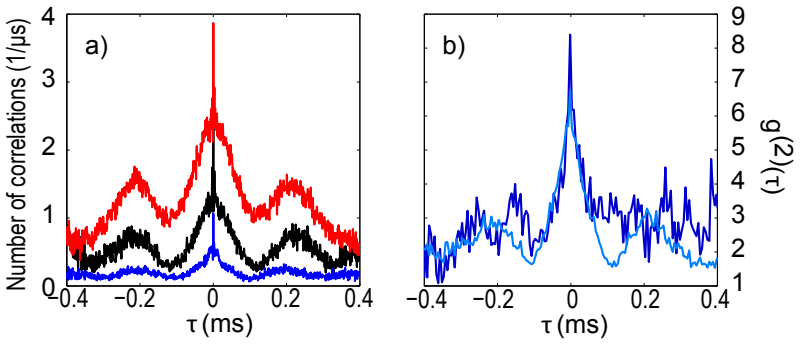


**Figure 5.17:** Atomic localization encoded in photon-photon correlations. a) The number of coincidences is plotted as function of the correlation time $\tau$. The overall number of coincidences drop when normal feedback is applied (blue data) with respect to no feedback (black data) whereas inverted feedback increases the number (red data). The oscillation frequency remains almost unchanged oscillating at $\approx 4.5$ kHz. b) Normalized $g^{(2)}(\tau)$ for a single long trace (dark blue data) compared to the average over $\approx 100$ traces (light blue data). The small contribution of well coupled atoms, which is hidden in the ensemble average, is visible for a single trace characterized by a faster oscillation frequency.

### 5.5.2 Localization encoded in correlations

Additional information about the effect of feedback on the atomic localization is obtained from photon-photon correlations. The reduced transmission due to a better localized atom when normal feedback is applied is directly visible in the reduced number of coincidences. Figure 5.17 a) shows the number of coincidences as a function of the correlation time $\tau$ and confirms the discussion of the previous section. The overall number of coincidences is lowered when normal feedback is applied (blue data) and enhanced for inverted feedback (red data) with respect to a measurement without feedback (black data). Here, two circuit strategies with $T_{fast} = 10\,\mu$s and $T_{slow} = 40\,\mu$s switch the torus potential from 50 nW to 250 nW.
The correlation function also reveals the oscillation frequency of the atom in the trap. A better localization should lead to a faster oscillation of the atom. Surprisingly, the oscillation frequency of $\approx 4.5$ kHz depends only marginally on the feedback strategy ($\approx 4.8$ kHz for normal feedback). The absence of the expected higher oscillation frequency in Fig. 5.17 a) when normal feedback is applied can be attributed to the data evaluation. Each measurement accumulated data over $\approx 100$ traces to gather enough statistics. The normalized transmission of 0.1 in the qualification intervals ensures a strong coupling strength which therefore determines the oscillation frequency. The main effect of the feedback could be an enhancement of very well coupled atoms. As the data is averaged over a hundred traces, the correlations are dominated by badly coupled atoms (still fulfilling the postselection criterion) which leads to a

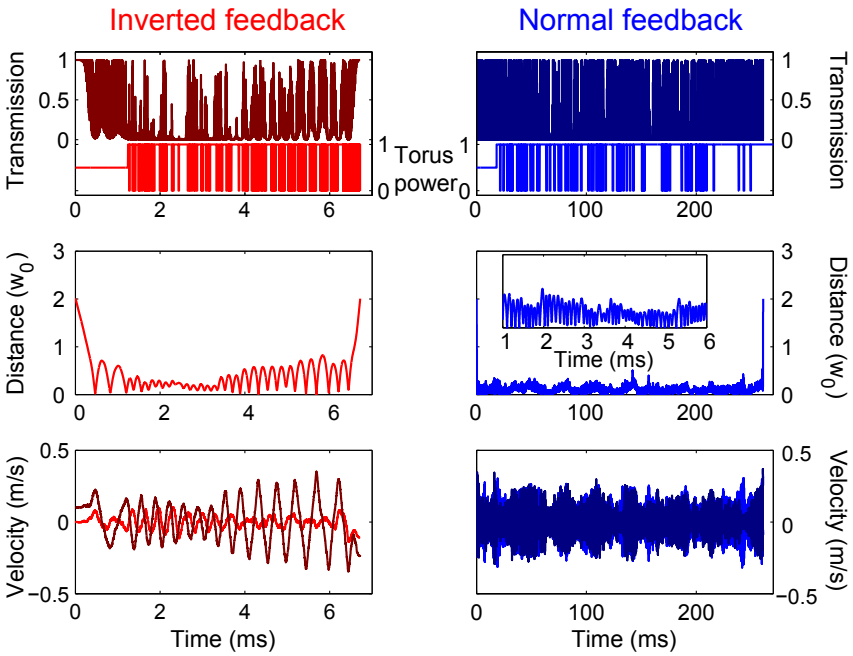


**Figure 5.18:** Two example traces of simulated atomic trajectories. The left panel (red) corresponds to inverted feedback the right panel to normal feedback. In the upper graphs the probe beam transmission (dark color) and the corresponding switching (light color) is shown. The radial oscillation (central panel) shows an oscillation with a large amplitude ($\leq w_0$) at a slow frequency ($\approx 2$ oscillations per ms) when inverted feedback is applied and with a smaller amplitude ($\approx w_0/4$) and a higher frequency ($\approx 5$ oscillations per ms) when normal feedback is applied. The lowest panel shows the velocity of the atom in two perpendicular, radial directions. It shows how the atom is heated in one direction (dark red curve) when inverted feedback is applied.

higher photon flux. In order to observe the improvement in the localization via the oscillation frequency a single long trace is evaluated. Due to the fact that feedback enables long storage times it is possible to compare the correlations of a single long trace (storage time of $\approx 250$ ms) with the ensemble average. Therefore, $g^{(2)}(\tau)$ with a larger binning of $5\,\mu$s is appropriate to guarantee a reasonably good signal-to-noise ratio already for a single trace. The normalized transmission is 0.1. Figure 5.17 b) shows that the oscillation frequency increases from $\approx 4.7$ kHz for the ensemble average (light blue data) to $\geq 7$ kHz for a single trace (dark blue data).
As an additional remark, the results for inverted feedback in Fig. 5.17 a) show an enhanced number of coincidences at the first minima at $\tau \approx \pm 0.1$ ms with respect to the second minima at $\tau \approx \pm 0.37$ ms. We interpret this effect as heating of the atom, as discussed in Sec. 4.4.
The obtained results are summarized by two simulated example traces in Fig. 5.18 (top row). The transmission (dark colored) and corresponding switch-

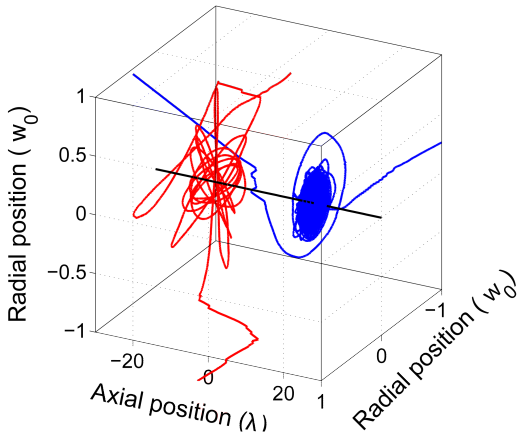


**Figure 5.19:** Three-dimensional atomic trajectories reconstructed from simulations. The x-axis corresponds to the cavity axis indicated as black line. Two trajectories are shown, one when normal feedback is applied (blue) and one for inverted feedback (red). It is striking that while the atomic excursion in the radial direction is large for the red trace it is rather small for the blue one. In addition the blue trajectory shows a higher line density corresponding to a longer storage time.

ing (light colored) is shown when inverted (left panel, red) and normal feedback (right panel, blue) are applied. The corresponding radial distance of the atom from the cavity axis (central panel) shows the characteristic oscillation, with a frequency depending on the amplitude. When inverted feedback is applied, the amplitude, $A$, of the oscillation is as large as the mode waist $w_0$, the frequency $f$ is $\approx 2$/ms and the storage time $ST$ is $\approx 6$ ms. For normal feedback the corresponding numbers are $A \approx 0.2 \times w_0$, $f \approx 5$/ms and $ST \approx 280$ ms. The lowest row displays the velocity in two orthogonal, radial directions. When normal feedback is applied the velocities oscillate in both radial directions for more than 200 ms with a dynamical decrease and increase of its envelope. For inverted feedback the velocity in one direction increases rapidly within a few ms until the atom is lost.
The discussed dynamics can be viewed in a three-dimensional reconstruction of the atomic trajectory, as depicted in Fig. 5.19. The axial position corresponds to different antinodes of the trapping potential for each trace. The radial excursion of the atom strongly depends on the applied feedback protocol, where red corresponds to inverted feedback and blue to normal feedback.

## 5.6 Feedback cooling

Real-time feedback results in an enhanced storage time as well as an improved localization. This is only possible by continuous cooling. However, a proof that feedback indeed reduces the atomic temperature is missing so far. A

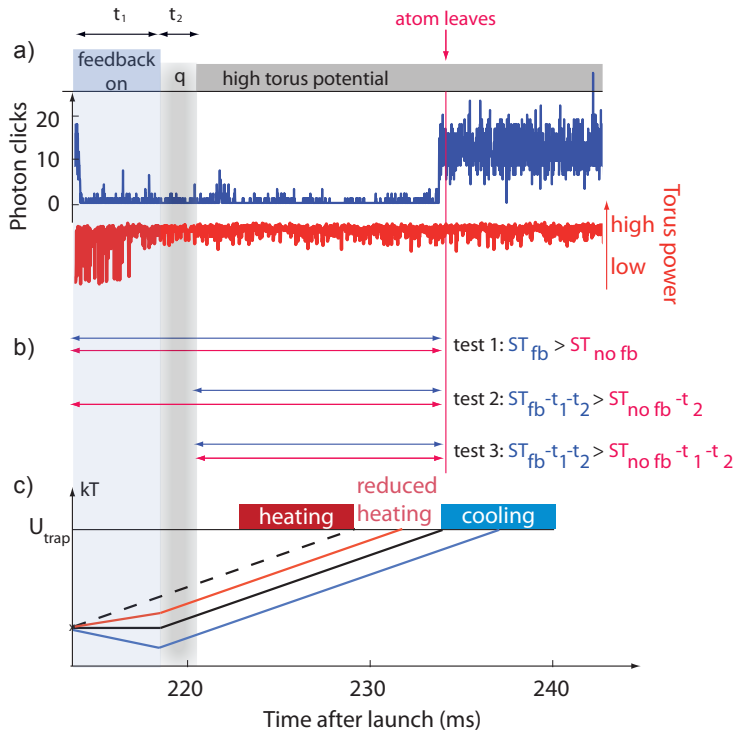


**Figure 5.20:** Schemes to prove feedback cooling. a) The measurement sequence starts with a feedback interval of length $t_1$ and a qualification interval, q, of length $t_2$. Subsequently, the trapping potential is switched to 600 nW. b) The storage time, $ST$, is obtained for an ensemble of traces. Three tests prove feedback cooling by comparing different storage times (see text). c) The energy diagram demonstrates the connection between the atomic temperature and the storage time, where feedback cooling results in an enhanced storage time by more than $t_1$.

straightforward attempt is to apply feedback only for a certain time, $t_1$, and observe the average storage time depending on $t_1$. The measurement sequence starts with a short feedback interval and continues with a constantly high torus potential of 600 nW, as depicted in Fig. 5.20 a). The data in the so-called qualification interval, q, of length $t_2$ is neglected in order to compensate for initially badly coupled atoms, or atoms which are affected by the rapid end of the feedback interval. Only atoms which stay longer than $t_2$ are used in the evaluation. Feedback with two exposure loops is the most promising candidate with $T_{fast} = 10\,\mu$s and $T_{slow} = 40\,\mu$s switching the torus potential from 50 nW to 600 nW. In the following we discuss three different tests to prove feedback cooling.

Test 1: A first test investigates the dependence of the average storage time on $t_1$. Feedback is applied for 0, 1, 2 and 3 ms. Figure 5.21 a) shows that the storage time indeed increases the longer feedback is applied. $t_2$ is chosen to be 0.1 ms. This result is further evidence of feedback cooling. However, a

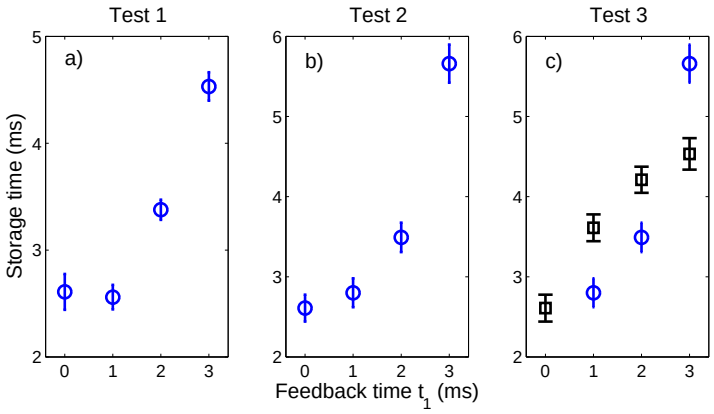


**Figure 5.21:** Three tests of feedback cooling. Test 1 investigates the dependence of the average storage time on $t_1$, neglecting the first 0.1 ms in all cases. It shows an increasing storage time for increasing $t_1$, which at least demonstrates that feedback results in less heating than no feedback. Test 2 proves that after applying the feedback interval an atom stays longer than without this feedback interval. However, test 3 suggests that any atom which stays longer than up to 2 ms stays in addition on average even longer than the overall average storage time. A feedback interval of 3 ms still significantly enhances the storage time.

confident proof of cooling would show that the atomic temperature after the feedback interval is below its initial value. Figure 5.20 c) shows a simplified schematic of the atomic temperature as a function of the measurement time. The goal is to prove that the temperature decreases during the feedback interval (blue line). Without going into details of heating processes in cavity QED (a detailed discussion can be found in [Mur03, Mur06a]) we assume a constant heating rate, indicated by parallel lines, as soon as the feedback is turned off. At the end the discrimination between feedback cooling and heating boils down to a comparison of the average storage times $ST$. Therefore, feedback cooling would correspond to a storage time which is longer than without feedback by more than the duration of the feedback interval. One reason why this criterion is not fulfilled is that the torus trap potential is rapidly switched to high power after the feedback interval and is therefore likely to heat the atom.
Test 2: To prove cooling of the atom below its initial temperature, the storage time without feedback should be shorter than the storage time after the feedback interval was applied. Therefore, the evaluation of the storage time starts after a time $t_1 + t_2$, neglecting atoms which are lost before. Figure 5.21 b) suggests that feedback applied for at least 2 ms indeed cools the atom below its initial temperature. In order not to artificially shorten the storage time without feedback due to losses of initially bad coupled atoms, $t_2$ is set to 1 ms here. However, one remaining question is if the postselection of long traces favors longer average storage times. In other words, if an atom which already stayed longer than 3 ms is likely to remain trapped longer than average.

Test 3: Test 3 should prove that this postselection is not responsible for the longer storage times in test 2 which we interpreted as feedback cooling. The evaluation of the storage time without feedback is done now in the same way as with the feedback interval, omitting $t_1 + t_2$. For example, when feedback is applied for 3 ms and $t_2$ is set to 1 ms, the first 4 ms are omitted in the data evaluation of the storage time for both with the feedback interval and without. It turns out that only feedback which is applied for 3 ms fulfills this condition. In summary, all proofs for feedback cooling are fulfilled when feedback is applied for 3 ms. This feedback cools the atom below its initial temperature. In the future, one goal is to directly observe a decreasing atomic temperature.

## 5.7 Summary and outlook

Beside the fascinating physics of tracking and steering the trajectory of a single atom in real time when moving in an optical dipole trap, this work opens new control possibilities. It demonstrates that feedback can be used to control the atomic motion in the transverse direction of the beam propagation. Therefore no side-access is needed to control an atom in all three dimensions. This enables experiments in cavity QED with arbitrarily small mirror spacing and thus to explore new regimes of strong coupling. Ideally, one could think about a "closed box" geometry, with an atom sitting in the center. Improved storage times of the atom when real-time feedback is applied already demonstrate the power of this technique to control the atom. However, to compete with state-of-the-art laser cooling techniques storage times on the order of a second are desired. Predicted average storage times of about 400 ms in simulations with realistic parameters brings this goal into reach even for relatively large probe power of 1 pW.
In an extension of this work, feedback could be applied on resonance with one of the normal modes. In this regime the transmission is more sensitive to very well coupled atoms and it should be possible to improve the localization of the atom further. Then, the algorithm has to be inverted as the presence of an atom now causes an increase in the transmission. The reduced photon flux could be compensated by increasing the probe power. On resonance with the empty cavity the transmission has its maximum without an atom present, so that a high probe power comes with the danger of exposing too much light on the single-photon detectors when the atom has left. In contrast, on resonance with the normal modes the transmission has its maximum in presence of the atom. However, on resonance with the normal modes a Stark shift would result in axial heating of the atom. The blue-detuned torus trap is an ideal actuator to avoid this problem due to the small Stark shift.
An extension of classical feedback into the quantum domain is desirable. There is no unambiguous definition of quantum feedback in the literature. For a pure

quantum feedback all steps, namely detection, decision and action, would be "quantum", but so far in most concepts only one of the steps involves quantum mechanics. Although in the presented work all three steps are classical, the atom-cavity system has characteristics which cannot be described classically. One simple approach to involve quantum mechanics would be to use a pure quantum resonance [Sch08c, Kub08], as described in the next chapter, to discriminate between badly and well coupled atoms. But still the feedback would remain to a large extent classical. In the following two examples of ongoing research are discussed and compared to this work.

At low temperatures the atomic states of motion are quantized. It can be argued that one employs quantum feedback when the atom is cooled to its ground state. A theoretical prediction of this scenario can be found in [Ste04]. *The observer estimates the atomic state in an atom-cavity system with the use of a conditioned homodyne measurement. In this context the estimation of the atomic state means the integration of the stochastic master equation in real time. Besides the reduction of the mean effective energy, below the initial energy, simulations demonstrate how the lowest bands of the optical potential can be populated. Quantum feedback can lead to a steady-state population of almost* 50 % *in the lowest band.*

Quantum feedback will also lead to new tools, like the protection of a system against decoherence. *In [Dot09] Monte Carlo simulations show the efficient, on-demand production of Fock states stored in a high-quality superconducting microwave cavity and their protection against coherence via quantum feedback. The feedback can again be separated in three main steps. First, the information of the photon-number state is extracted via the light shift of single circular Rydberg atoms while dispersively interacting with the cavity field. Second, the cavity field is estimated and third, the injection of a coherent pulse corrects the field state.* A prerequisite for this experiment is a weak quantum measurement together with correction in real time. In this context our work realizes a fast real-time feedback that is fundamentally limited by the single-photon character at extremely low photon flux. Individual probe photons carrying information about the atomic position activate a dipole laser that steers the atom on timescales 70 times shorter than the atom's oscillation period in the trap.

# 6 Two-photon spectroscopy and nonlinear intensity response

The content of this chapter has partially been published in
I. Schuster, A. Kubanek, A. Fuhrmanek, T. Puppe, P. W. H. Pinkse, K. Murr, and G. Rempe,
"Nonlinear spectroscopy of photons bound to one atom,"
Nature Physics. 4, 382 (2008).

## 6.1 Introduction

A long-standing goal in quantum optics is to induce nonlinearities on the level of a few quanta. Towards this goal we investigate the higher-order dressed states. A probe laser resonant with the atom can selectively populate in a two-photon process a state of the coupled atom-cavity system containing two energy quanta. In this way a single atom is dressed by a pair of photons. In contrast to the normal modes the multi-photon resonances do not have any classical analogue and are pure quantum effects. In the microwave domain, these higher excited Jaynes-Cummings states have been featured in numerous publications for several decades ([Rem87, Bru96, Sch07, Fin08, Hof08]). In the optical domain they have escaped an experimental observation until recently ([Sch08c]).
This chapter presents the spectroscopy of higher-order dressed states. The vicinity of the normal modes make the spectroscopy very sensitive to variations of the experimental parameters. In Sec. 6.2, two different strategies to observe the two-photon resonance are presented. A new scan technique which is only sensitive to the higher-order dressed states allows the two-photon resonance to be isolated from the normal modes. In addition to the experiments described in [Sch08b] that were done in the red-detuned dipole trap, new measurements were performed in a combination of both, a red- and blue-detuned dipole trap. In Sec. 6.3 the nonlinear intensity response of the system is demonstrated when addressing the two-photon resonance. A short conclusion in Sec. 6.4 brings the chapter to an end.

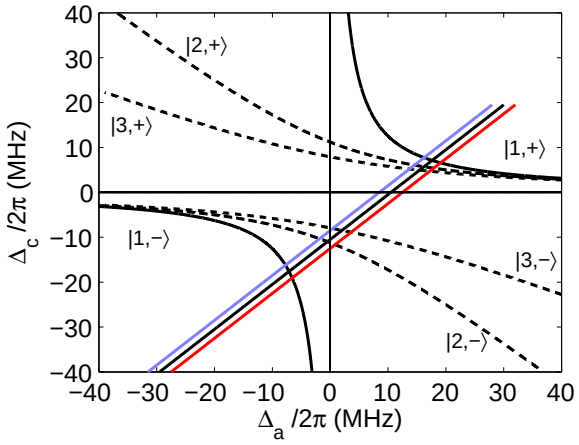


**Figure 6.1:** Parameter space representing the calculated eigenstates of the coupled atom-cavity system. Three different scans (colored diagonal lines) excite single- and multi-photon resonances of the coupled system. All scans are performed by changing the frequency of the probe laser, while all other parameters are fixed. As depicted in Tab. 6.1 the only difference between the scans are different trapping potentials, resulting in a different overall Stark shift. The calculations are done for an effective coupling strength of $g/2\pi = 11.2$ MHz.

## 6.2 Spectroscopy of the two-photon resonance

Transmission spectroscopy of a two-photon resonance is performed with two different strategies to scan the parameter space. With the first method we scan the probe laser frequency while all other parameters are fixed. With the second method we scan the cavity resonance while the probe laser is always on resonance with the bare atom.

### 6.2.1 Exciting single- and multi-photon resonances

In a first experiment we scan the probe laser frequency across the resonances of the coupled system using a switching measurement as described in Sec. 3.1.9. Figure 6.1 shows the calculated eigenstates of the coupled atom-cavity system with respect to the detuning between the probe laser and the bare atom, $\Delta_a$, or the bare cavity, $\Delta_c$, respectively. Three different scans are marked with colored lines and are discussed in the following. For calculating the eigenstates of the dressed states in Fig. 6.1 we use an effective coupling strength of $g/2\pi = 11.2$ MHz which is adapted to the experiment.
Fig. 6.2 shows the measured spectrum for a red dipole trap of 155 nW superimposed with a blue-detuned, torus trap of 250 nW and an effective coupling strength of $g/2\pi = 12$ MHz. The spectrum is dominated by the two normal modes, $|1,-\rangle$ and $|1,+\rangle$, but due to the relatively high probe power of 1.5 pW

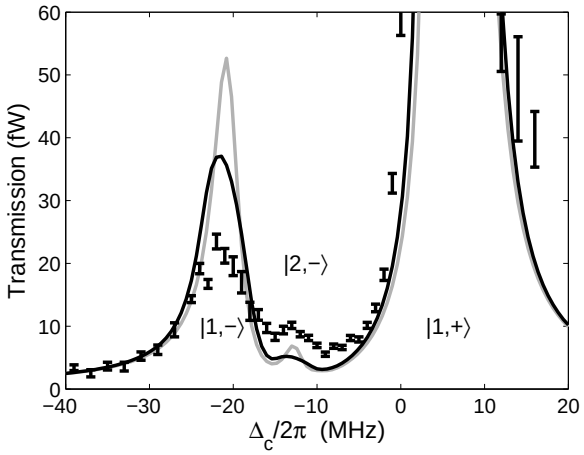


**Figure 6.2:** Spectroscopy of the two-photon resonance in a blue-detuned dipole trap with the parameter set (iii) (see Tab. 6.1). The two-photon resonance appears as a small peak in the transmission spectrum. Two theory curves predict the appearance at the right frequency position. The grey line corresponds to a fixed-atom theory, where the coupling strength is constantly 0.75 of the maximal coupling. The black line accounts for a fluctuating coupling strength between 0.6 and 0.9 of $g_{max}$ due to the atomic motion. It results in a broadening of the resonance peaks.

an additional resonance besides the normal modes is visible, the two-photon resonance $|2,-\rangle$. Theoretical calculations of the spectrum, solving the master equation introduced in Sec. 2.3.2 with $N = 7$ Fock states, agree well with the expected frequencies of the resonance peaks (grey line). A further increase of the size of the Hilbert space for the intracavity field does not change the result. However, the atomic motion leads to a broadening of the resonances with a reduction of the height and an increase of the width of the resonance peaks. Therefore including a varying coupling strength between 0.6 and 0.9 of $g_{max}/2\pi = 16$ MHz with a Gaussian distribution around the average coupling strength of $0.75\, g_{max}$ improves the agreement with experiment (black line). The atomic motion also leads to a changing Stark shift, $S$, that also effects the transmission spectrum. Here, we only account for an average Stark shift and not for a fluctuation of it. From these fits the averaged parameters of the Stark shift and the effective coupling strength, as shown in Tab. 6.1 (iii), are obtained.
The corresponding parameters for all other scans are obtained in the same way. An overview of all measurements performed in this section is shown in Tab. 6.1. Remarkably, the overall Stark shift increases from $S/2\pi = 24.5$ MHz to $S/2\pi = 26.5$ MHz ((i) compared with (vi)) when a blue-detuned trapping potential of 250 nW is added (see Sec. 3.1.9). Although a blue-detuned dipole trap, in principle, induces a negative Stark shift the improved localization of the atom to regions with a strong red-detuned dipole trap results in an overall

| Parameter set | (i) | (ii) | (iii) | (vi) |
|---|---|---|---|---|
| dipole trap (red (nW) / torus (nW)) | 170 / 0 | 140 / 250 | 155 / 250 | 170 / 250 |
| overall Stark shift ($S/2\pi$ MHz) | 24.5 | 22.5 | 24.5 | 26.5 |
| bare atom detuning ($\Delta_{a,0}/2\pi$ MHz) | 35 | 35 | 35 | 35 |
| effective coupling strength ($g/2\pi$ MHz) | 11.2 | 11.2 | 12 | 11.2 |
| probe power (pW) | 1.5 | 1.5 | 1.5 | 1.5 |

**Table 6.1:** Parameters of four different transmission measurements. The effective coupling strength and the overall Stark shift is determined by a fit of the fixed-atom theory to the spectrum, as depicted in Fig. 6.1. Measurements using (i) have been reported in [Sch08b].

increase of $S$.
Figure 6.3 a) shows the same scan performed for different parameters. The black data is a reference measurement in a pure red dipole trap (i) from [Sch08b]. The red (ii) and blue (vi) data are obtained in a combination of a red- and blue-detuned dipole trap. The difference in the trapping potential causes a small change in the Stark shift which differs by only $2\pi \times 2$ MHz between each data set. However, the two-photon resonance is only visible when the right parameter window is matched within roughly 1 MHz. If the Stark shift is too large, as in data set (vi), then $|2,-\rangle$ and $|1,-\rangle$ are too close to each other. The normal mode dominates and the two-photon resonance is hidden as a shoulder on the right side of $|1,-\rangle$. If the Stark shift is too small (ii), the resonances are well separated, but the transition strength to $|2,-\rangle$ is weaker and the peak height decreases. The peak position of the resonances agrees well with the theory of Fig. 6.1.
The experimental transmission spectra are well reproduced when the atomic motion is taken into account by Monte Carlo simulations (see Sec. 2.3.3). The results are shown in Fig. 6.3 a) as solid lines. The model used is a full quantum mechanical description of the system, where the cavity field as well as the atomic dipole is quantized. To illustrate that a full quantum theory is necessary to explain the higher-order dressed states, we compare this model with a classical calculation. In Fig. 6.3 b) the result of Monte Carlo simulations based on a classical model are shown as dashed lines. Here, neither the atomic dipole nor the light field are quantized resulting in a reproduction of the normal modes but in an absence of the two-photon resonance. Hence, to

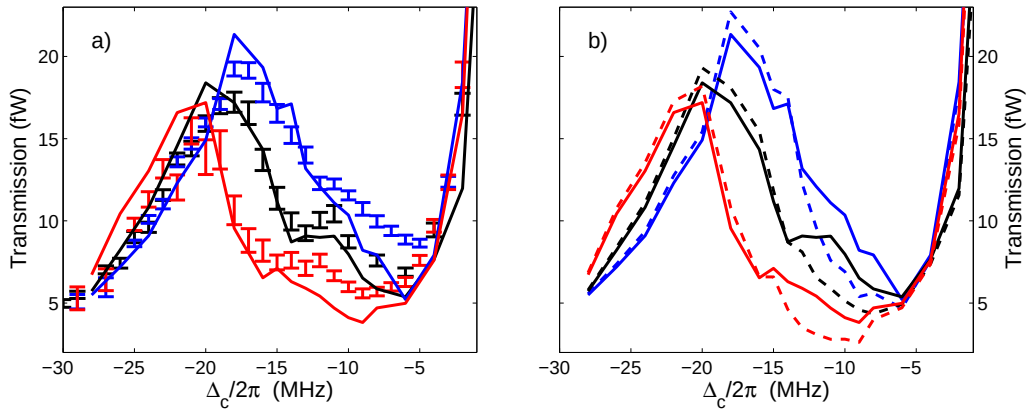


**Figure 6.3:** Transmission spectrum for different trapping potentials. a) A pronounced two-photon peak in a red dipole trap of 170 nW (black data) turns into a shoulder when a blue torus potential of 250 nW is superimposed (blue data). Lowering the red trapping power to 155 nW enhances the separation between the two-photon resonance and the normal mode, but also decreases the excitation strength (red data). Monte Carlo simulations (solid lines) show a nice agreement with the experiment, reproducing the height as well as the width of the resonances. b) Comparing simulations based on a quantum mechanical model (solid lines) with simulations based on a classical model (dashed lines) shows that the two-photon resonance is only reproduced when both the atom and the light field are quantized.

describe the two-photon resonance the quantization of both the atom and the light field is crucial, see [Sch08b] for details.

### 6.2.2 Exclusively exciting multi-photon resonances

The vicinity of the normal modes makes it hard to locate the higher-order dressed states. An elegant way to make the measurements less sensitive to the chosen parameters is to decouple the transmission spectrum from the normal modes. The strategy is to keep the probe beam frequency fixed on the atomic transition and scan the cavity frequency. In this case, the two-photon doublet $|2,\pm\rangle$ is directly excited for a suitable cavity frequency, whereas the single-photon doublet $|1,\pm\rangle$ is completely avoided because the energy level structure is strongly anharmonic.
This can be seen by inserting the resonance condition for single-photon absorption, $E_1 = \hbar\omega$, into Eq. (2.18). The normal modes are excited when $\Delta_a\Delta_c = g^2$. Two photon absorption, $E_2 = 2 \times \hbar\omega$, is fulfilled for $\Delta_c^2 + \Delta_a\Delta_c = g^2$. Therefore, as long as the system is excited on resonance with the atom, $\Delta_a = 0$, the normal modes are never excited. When the cavity frequency is scanned, the splitting between the two-photon resonances is given by $\Delta_c = \pm g$. Figure 6.4 shows the applied scan in the $\Delta_a\Delta_c$-diagram. In the experiment one has to

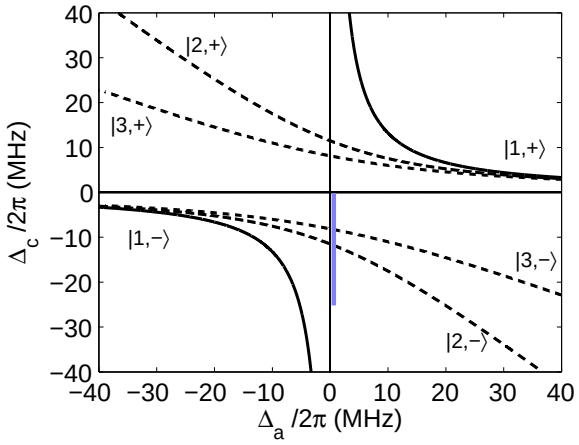


**Figure 6.4:** Scanning technique that excites exclusively the higher-order resonances while avoiding the normal modes. The blue line characterizes the direction of the scan and shows that it never crosses the resonance frequency of the normal modes. The calculations are done for an effective coupling strength of $g/2\pi = 11.2$ MHz.

account for the linewidth of the normal modes, as well as for motional-induced fluctuations in measurement parameters such as the Stark shift and the coupling strength. This leads to a residual contribution of the normal modes.
Figure 6.5 shows the scan for different probe powers. The experimental parameters correspond to those from Tab. 6.1 (i), but now with $\Delta_a/2\pi = 1$ MHz and with an initial atom detuning of $\Delta_{a,0}/2\pi = 21$ MHz. For probe powers as low as 0.5 pW (Fig. 6.5 d)) the coherent light beam contains almost no photon pairs. Therefore, a flat background is present in the transmission spectrum for all detunings. Increasing the probe power to 1.5 (Fig. 6.5 c)), 2.5 (Fig. 6.5 b)) and 3.5 pW (Fig. 6.5 a)) enhances the probability for photon pairs in the probe beam and therefore the probability to excite the two-photon resonance. Monte-Carlo simulations using the quantum mechanical model (solid line) nicely agree with the data. A contribution from higher-order resonances can be identified through a deviation of the data from the simulation around $\Delta_c/2\pi = -8$ MHz. The simulations only include the two-photon contribution and neglect higher-order contributions (see [Sch08b] for details). Simulations using classical equations (dashed line) agree well with the experiment for large detunings $\Delta_c < -20$ MHz, where the signal comes from a residual contribution of the normal modes. Multi-photon resonances can not be reproduced by this theory.

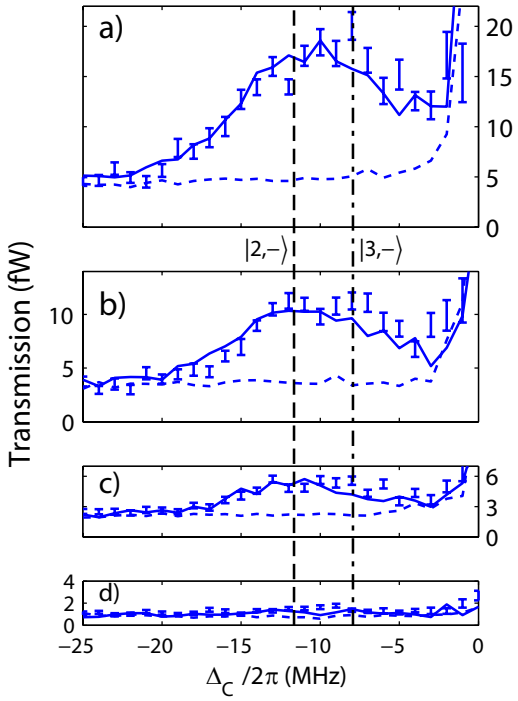


**Figure 6.5:** Exclusively exciting higher-order resonances with parameter set (i). The probe power is increased from d) to a) from 0.5, 1.5, 2.5 to 3.5 pW. The two-photon resonance becomes visible only for sufficiently high probe powers. While classical simulation (dashed line) do not reproduce the two-photon resonance, quantum mechanically treated simulation do nicely agree with the experiment (solid line). The predicted peak position of the resonances from the fixed-atom theory are marked with dashed lines (see Fig. 6.4). The measurements have also been reported in [Sch08b].

## 6.3 Nonlinear intensity response

Due to the multi-photon nature of the higher-order resonances, the intensity response of the system is expected to have nonlinear components. While single-photon contributions scale linearly, photon-pair contributions scale quadratic with intensity, three-photon contribution scale cubed and so on. When exciting the two-photon resonance, we therefore expect a quadratic behavior of the intensity response. However, there is always a small offset of the linear contribution from the normal modes, as discussed in the previous section. Therefore, we group the transmission between $-15$ MHz $\leq \Delta_c/2\pi < -10$ MHz for the two-photon contribution and subtract the single-photon contribution due to the normal modes, obtained by the average transmission between $-25$ MHz $\leq \Delta_c/2\pi < -20$ MHz. Figure 6.6 shows the nonlinear intensity response of the system. A fit of the data (blue line) to the function $I_{out} \sim \alpha_1 I_{in} + \alpha_2 I_{in}^2 + \alpha_3 I_{in}^3 + ...$ yields that only $\alpha_2 = 1$ while all other $\alpha_i = 0$.

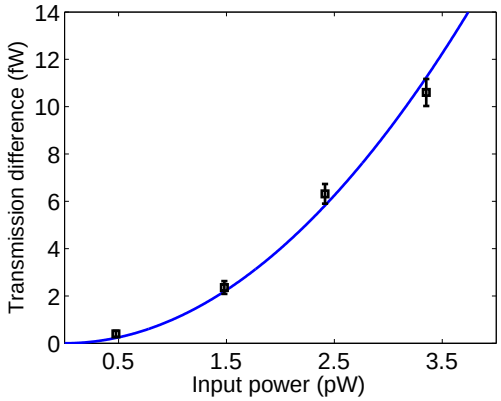


**Figure 6.6:** Nonlinear intensity response. The transmission on resonance with the two-photon resonance shows a quadratic intensity response, when the linear contribution from the normal modes is subtracted. $I_{out}$ is plotted (blue line) where only $\alpha_2 = 1$. The measurements have also been reported in [Sch08b].

This shows the quadratic dependence of the output intensity on the input intensity in transmission spectroscopy on resonance with the two-photon state.

## 6.4 Conclusion

In this chapter we have demonstrated different techniques to perform spectroscopy of the two-photon resonance in a strongly coupled atom-cavity system. The output intensity scales quadratically with the input intensity. It is this nonlinearity on the level of a few quanta that is the main ingredient for possible applications like the development of optical switches or 'transistors' that work on the level of a few photons. Here, the idea is that a gate field of a single photon is sufficient to control a signal field ([Ber06, Cha07]). Another promising application is its implementation in the field of quantum information processing, where this effect could be used to implement quantum gate operations with a single trapped atom ([Wer99]), ([Reb99]).
An extension to this work could imply two probe lasers with different frequencies. The first one excites one of the normal modes and the second one is resonant with the transition from the normal mode to one of the second-order dressed states. Thus, the first laser controls the transmission of the second one. In the ideal case, a single photon in the first beam is sufficient to switch from full reflectivity to a transmission of single photons in the second beam. With the success of exciting the two-photon resonance and with the obtained understanding of the system two-color spectroscopy should be feasible.

# 7 Two-photon gateway

The content of this chapter has partially been published in
A. Kubanek, A. Ourjoumtsev, I. Schuster, M. Koch, P. W. H. Pinkse, K. Murr, and G. Rempe,
"Two-photon gateway in one-atom cavity quantum electrodynamics,"
Physical Review Letters 101, 2036602 (2008).

## 7.1 Introduction

An interaction between photons usually involves sufficiently high powers and is mediated via matter. In order to make photons interact one by one three major requirements need to be fulfilled:
1. low photon losses,
2. a tight confinement,
3. a strong nonlinearity.

The first two requirements result in a long interaction time which can be fast if the nonlinear response of the medium to the optical excitation is strong enough. The medium needs to have a low absorption and light must be coupled efficiently into this medium.
The strongly coupled atom-cavity system fulfills all these requirements. The first two are guaranteed by the high-finesse cavity, which enhances the strength of light-matter interaction allowing for multiple photon effects at extremely low light intensities. The fourth is ensured by the atom, which induces an optical nonlinearity on the level of a few photons and mediates an effective interaction between the photons.
In this chapter we address the question whether one atom can strongly interact with two resonant and uncorrelated photons such that the emitted photons come out in pairs. This phenomenon has been predicted [Car96] but never observed. A cornerstone of this chapter is the study of photon statistics of the light resonantly scattered by a single atom. Photon antibunching is by now a well-established phenomenon, confirming Einsteins view that energy is radiated quantum by quantum. For strong coupling between light and matter, novel photon statistics have been predicted and observed for many intracavity atoms [Rem91, Fos00b, Fos00a]. For a single atom in the cavity, photon antibunching has been demonstrated [Kuh02, McK04, Kel04].
The origin of our investigation is the two-photon resonance. Its spectroscopy

was discussed in the previous chapter. In this chapter we investigate the enhanced emission of two correlated photons due to the excitation of the two-photon state. The increased rate of photon pairs leaving the cavity through the output mirror results in a novel photon bunching phenomenon. Photon bunching has been proposed [Car96, Sch08a] as a means to detect the higher excited Jaynes-Cummings states [Jay63]. We introduce a new correlation function which is very sensitive to multi-photon resonances and allows to detect the two-photon resonance in a way that is robust to fluctuations in the experimental parameters.
The chapter is structured in the following way. Section 7.2 theoretically investigates the time-dependent state population when continuously exciting the two-photon resonance. An analytical model gives insight in the dynamics of the state population during the decay of the system into the ground state. Second-order correlations enable a connection between theory and experiment. Therefore, in Sec. 7.3 the $g^{(2)}(\tau)$-function demonstrates the expected photon bunching effect and also resolves a quantum beat of superposition states. Section 7.4 explores the multi-photon nature of the coupled system. A new correlation function $C^{(2)}$, which reveals the transition from photon antibunching to photon bunching, is introduced in Sec. 7.4.1 and compared with the $g^{(2)}$-function. In Sec. 7.4.2 the corresponding experiments are presented. The chapter ends with a short summary in Sec. 7.5.

## 7.2 Analytical four-level model

Based on the introduction in Sec. 2.3.2 we follow the guidance of [Sha10] to derive an analytical model describing the excitation and decay process of the two-photon resonance. We generalize the model, extend the work into the optical domain and to lower coupling strength. The model is only valid in a small but interesting parameter range since some of the assumptions break down, e.g., for large detunings.
We start by truncating the Jaynes-Cummings ladder after the first four states ($|0\rangle \equiv |0\rangle$, $|1\rangle \equiv |1,-\rangle$, $|2\rangle \equiv |1,+\rangle$ and $|3\rangle \equiv |2,-\rangle$) introducing a 4-level model as depicted in Fig. 7.1. The general master equation reads

$$\begin{aligned}\frac{d\rho}{dt} = \frac{1}{i\hbar}[H,\rho] &+ \frac{\Gamma_{32}}{2}(2|2\rangle\langle 3|\rho|3\rangle\langle 2| - |3\rangle\langle 3|\rho - \rho|3\rangle\langle 3|) \\ &+ \frac{\Gamma_{31}}{2}(2|1\rangle\langle 3|\rho|3\rangle\langle 1| - |3\rangle\langle 3|\rho - \rho|3\rangle\langle 3|) \\ &+ \frac{\Gamma_{20}}{2}(2|0\rangle\langle 2|\rho|2\rangle\langle 0| - |2\rangle\langle 2|\rho - \rho|2\rangle\langle 2|) \\ &+ \frac{\Gamma_{10}}{2}(2|0\rangle\langle 1|\rho|1\rangle\langle 0| - |1\rangle\langle 1|\rho - \rho|1\rangle\langle 1|)\end{aligned} \tag{7.1}$$

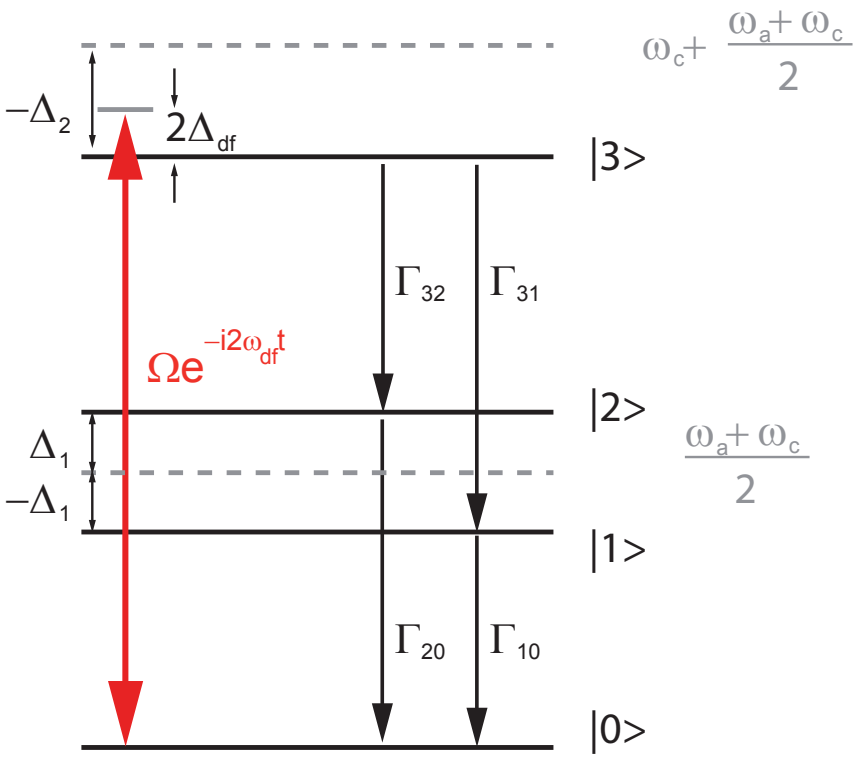


**Figure 7.1:** Four-level model for the analytical description of the excitation and decay of the two-photon resonance.

with the Hamiltonian

$$\begin{aligned} H \;= & -\hbar 2\Delta_{df}|3\rangle\langle 3| - \hbar(\Delta_{df} - \Delta_1 - \frac{\Delta_2}{2})|2\rangle\langle 2| - \hbar(\Delta_{df} + \Delta_1 - \frac{\Delta_2}{2})|1\rangle\langle 1| \\ & - \hbar\varepsilon[A(|0\rangle\langle 1| + |1\rangle\langle 0|) + B(|0\rangle\langle 2| + |2\rangle\langle 0|) \\ & + C(|1\rangle\langle 3| + |3\rangle\langle 1|) + D(|2\rangle\langle 3| + |3\rangle\langle 2|)] \end{aligned} \tag{7.2}$$

and the frequency splittings of the dressed states

$$\Delta_1 \;=\; \sqrt{(\frac{\omega_a - \omega_c}{2})^2 + g^2} \tag{7.3}$$

$$\Delta_2 \;=\; \sqrt{(\frac{\omega_a - \omega_c}{2})^2 + 2g^2}\,. \tag{7.4}$$

In contrast to [Sha10] we include a detuning of the atomic and cavity frequency, as well as a detuning of the driving frequency $\Delta_{df}$:

$$\omega_{df} \;=\; \frac{\omega_a + 3\omega_c}{4} - \frac{\Delta_2}{2} + \Delta_{df} \tag{7.5}$$

Note that here the levels $|1\rangle$ and $|2\rangle$ are shifted by $-\hbar\omega_l$, and level $|3\rangle$ is shifted by $-2\hbar\omega_l$. We have used the expansions for the field annihilation operator $a$ as well as for the atomic lowering operator $\sigma_-$ in a very general form

$$a = A|0\rangle\langle 1| + B|0\rangle\langle 2| + C|1\rangle\langle 3| + D|2\rangle\langle 3| \tag{7.6}$$

$$\sigma_- = E|0\rangle\langle 1| + F|0\rangle\langle 2| + G|1\rangle\langle 3| + H|2\rangle\langle 3|\,. \tag{7.7}$$

The corresponding loss channels are

$$\Gamma_{32} = \gamma H^2 + 2\kappa D^2 \tag{7.8}$$

$$\Gamma_{31} = \gamma G^2 + 2\kappa C^2 \tag{7.9}$$

$$\Gamma_{20} = \gamma F^2 + 2\kappa B^2 \tag{7.10}$$

$$\Gamma_{10} = \gamma E^2 + 2\kappa A^2 \tag{7.11}$$

where $\kappa$ and $\gamma$ are the decay rate of the cavity field and the atomic polarization decay rate. The eight remaining parameters $A$,$B$,$C$,$D$, and $E$,$F$,$G$,$H$ are determined by the bare Jaynes-Cummings energy eigenstates and depend only on $g$ and $(\omega_a - \omega_c)$

$$A = \cos\Theta_1 \tag{7.12}$$

$$B = \sin\Theta_1 \tag{7.13}$$

$$C = \sqrt{2}\cos\Theta_1\cos\Theta_2 + \sin\Theta_1\sin\Theta_2 \tag{7.14}$$

$$D = \sqrt{2}\sin\Theta_1\cos\Theta_2 - \cos\Theta_1\sin\Theta_2 \tag{7.15}$$

$$E = -\sin\Theta_1 \tag{7.16}$$

$$F = \cos\Theta_1 \tag{7.17}$$

$$G = -\cos\Theta_1\sin\Theta_2 \tag{7.18}$$

$$H = -\sin\Theta_1\sin\Theta_2\,, \tag{7.19}$$

with $\sin\Theta_n$ and $\cos\Theta_n$ from Eq. (2.16) and Eq. (2.17). With a detuning between the probe laser frequency and $|1\rangle$ or $|2\rangle$ of typically a few times the

linewidth of the normal modes we assume an excitation of $|3\rangle$ which is off-resonant with $|1\rangle$ and $|2\rangle$. This assumption breaks down for large atom-, cavity- or probe detunings. After elimination of the intermediate states $|1\rangle$ and $|2\rangle$ for the excitation process, where perturbative level shifts as well as the decay terms are neglected, the new Hamiltonian is

$$\begin{aligned} H \; =& -\hbar 2\Delta_{df}|3\rangle\langle 3| - \hbar(\Delta_{df} - \Delta_1 - \frac{\Delta_2}{2})|2\rangle\langle 2| - \hbar(\Delta_{df} + \Delta_1 - \frac{\Delta_2}{2})|1\rangle\langle 1| \\ &+ i\hbar\Omega(e^{-i2\omega_{df}t}|3\rangle\langle 0| - e^{i2\omega_{df}t}|0\rangle\langle 3|) \end{aligned} \tag{7.20}$$

where

$$\Omega \; = \; \varepsilon^2(\frac{AC}{\Delta_{df} + \Delta_1 - \frac{\Delta_2}{2}} + \frac{BD}{\Delta_{df} - \Delta_1 - \frac{\Delta_2}{2}}) \tag{7.21}$$

The ground state $|0\rangle$ and $|3\rangle$ are directly coupled via $\Omega$, whereas the intermediate states $|1\rangle$ and $|2\rangle$ are only populated via the decay channels $\Gamma$. The steady state solutions of the density matrix elements are

$$\rho_{11} \; = \; \frac{\Gamma_{31}}{\Gamma_{10}}\rho_{33} \tag{7.22}$$

$$\rho_{22} \; = \; \frac{\Gamma_{32}}{\Gamma_{20}}\rho_{33} \tag{7.23}$$

$$\rho_{33} \; = \; [1 + \frac{4\Delta_{df}^2 + \frac{1}{4}(\Gamma_{31} + \Gamma_{32})^2}{\Omega^2}]^{-1}\rho_{00} \tag{7.24}$$

and from normalization it follows that

$$\rho_{00} \; = \; [1 + \frac{\Omega^2}{\Omega^2 + \frac{1}{4}(\Gamma_{31} + \Gamma_{32})^2 + 4\Delta_{df}^2}(\frac{\Gamma_{31}}{\Gamma_{10}} + \frac{\Gamma_{32}}{\Gamma_{20}} + 1)]^{-1} \tag{7.25}$$

The coherence terms are

$$\rho_{03} \; = \; \frac{\Omega}{i2\Delta_{df} + \frac{\Gamma_{31}+\Gamma_{32}}{2}}(\rho_{00} - \rho_{33}) \tag{7.26}$$

$$\rho_{30} \; = \; \frac{-\Omega}{i2\Delta_{df} - \frac{\Gamma_{31}+\Gamma_{32}}{2}}(\rho_{00} - \rho_{33}) \tag{7.27}$$

while all other density matrix elements are 0 in steady state. The mean photon number inside the cavity in steady state is

$$\langle a^+ a\rangle_{SS} \; = \; (A^2\frac{\Gamma_{31}}{\Gamma_{10}} + B^2\frac{\Gamma_{32}}{\Gamma_{20}} + C^2 + D^2)\rho_{33} \tag{7.28}$$

The solution of the coupled equations of motion are obtained numerically while the coherence terms $\rho_{12}$ and $\rho_{21}$ do not couple to any other equation of motion and have the analytical solution

$$\rho_{12}(t) \;=\; e^{i2\Delta_1 t} e^{-\frac{\Gamma_{10}+\Gamma_{20}}{2}t} \rho_{12}(0)\,, \tag{7.29}$$

and

$$\rho_{21}(t) \;=\; e^{-i2\Delta_1 t} e^{-\frac{\Gamma_{10}+\Gamma_{20}}{2}t} \rho_{21}(0)\,. \tag{7.30}$$

After the emission of the first photon the system is prepared in a superposition state of $|1\rangle$ and $|2\rangle$ with the coherence described by $\rho_{12}(0)$ and $\rho_{21}(0)$. The first term in Eq. (7.29) and Eq. (7.30) describes an oscillation with a frequency proportional to the detuning $\Delta_1$. The second term describes the decoherence where the oscillation is damped on a timescale $\frac{\Gamma_{10}+\Gamma_{20}}{2}$. It determines the lifetime of the superposition state.

The time-dependent state population is obtained from the solution of the coupled equations of motion. For simplicity the system is at first driven on resonance with $|3\rangle$ and without an atom-cavity detuning $(\omega_c, \omega_a, \Delta_{df})/2\pi = (0, 0, 0)$ MHz. The parameters are adapted to the experiment, $(\kappa, \gamma, g) = 2\pi(1.25, 2.99, 12.8)$ MHz, with a driving field set to $\varepsilon \approx 1.3 \times \kappa$. Fig. 7.2 shows the time evolution of the state population (squared density matrix elements). The main population is in $|0\rangle$ and $|1\rangle$ (see Fig. 7.2 a), black solid and dashed line). After the emission of a first photon at $\tau = 0$, the population of $|0\rangle$ increases to a steady state population of above 96% within $2\kappa$. At the same time the population of $|1\rangle$, which is in this model only populated via the decay of $|3\rangle$, drops from initially $\approx 58\%$ to well below 3%. A qualitatively similar behavior can be observed for $|2\rangle$ and $|3\rangle$ but for a one hundred times lower occupation (see Fig. 7.2 c)). The population of $|3\rangle$ (grey solid line) builds up after emission of a photon reaching a steady state value of about $1.1 \times 10^{-2}$, while the population of $|2\rangle$ (grey dashed line) drops from about $1.1 \times 10^{-2}$ at $\tau = 0$ to $\approx 0.2 \times 10^{-2}$ within $2\kappa$. Of particular interest are the coherence terms $\rho_{21}$ and $\rho_{12}$. Initially unpopulated, the emission of a first photon projects the system into a superposition of the states $|1\rangle$ and $|2\rangle$, which induces the coherence. $\rho_{21}$ and $\rho_{12}$ oscillate with a frequency of $\approx 2\Delta_1$ with an exponential decay of $\approx \frac{\Gamma_{10}+\Gamma_{20}}{2}$ (see Fig. 7.2 b) red line). The coherence terms $\rho_{30}$ and $\rho_{03}$ are displayed as blue, dashed lines.

There are two main timescales involved in the dynamics. The increase of the population of $|0\rangle$ and $|3\rangle$ and the corresponding decrease of $|1\rangle$ and $|2\rangle$ happens on a timescale of $1/2\kappa$. The oscillation in the coherence terms $\rho_{21}^2$ and $\rho_{12}^2$ occur on a timescale of $1/2\Delta_1$. As the decay channel from $|3\rangle$ to $|1\rangle$ is dominant, the population of $|1\rangle$ exceeds that of $|2\rangle$.

To compare the theory with the experiment we derive $g^{(2)}(\tau)$ from the analytical model. A very general formula for $g^{(2)}(\tau)$ is given by

$$g^{(2)}(\tau) \;=\; \frac{A^2\rho_{11} + AB(\rho_{12}+\rho_{21}) + B^2\rho_{22} + (C^2+D^2)\rho_{33}}{\langle a^+ a\rangle_{SS}}\,. \tag{7.31}$$

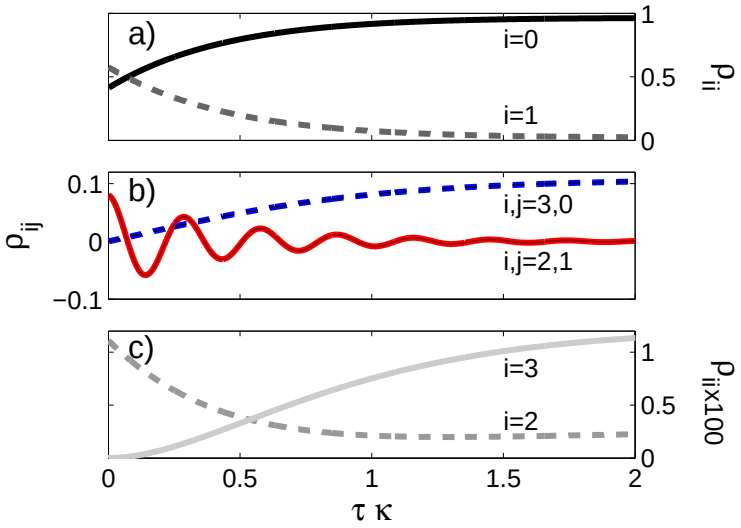


**Figure 7.2:** Time evolution of the state population $\rho_{ii}$ and the coherence terms $\rho_{ij}$. a) After the emission of a first photon the population of the state $|0\rangle$ (black line) is projected to a minimum value slowly recovering until the steady state population of $> 0.96$ is reached. The population of $|1\rangle$ (black dashed line) has its maximum of $\approx 0.58$ at $\tau = 0$ which drops to the steady state after $\tau \approx 2\kappa$. b) The population of the coherence terms $\rho_{21}$ and $\rho_{12}$ (red line) oscillate at a frequency of $\approx 2\Delta_1$ and with an exponential damping. The coherence terms $\rho_{03}$ and $\rho_{30}$ (blue, dashed line) recover after the emission of a photon up to a steady state value of $\approx 0.1$. c) The occupation of $|2\rangle$ (grey dashed line) and $|3\rangle$ (grey solid line) show a complementary behavior as in a) but with a one hundred times lower occupation than $|0\rangle$ and $|1\rangle$.

The results are plotted in Fig. 7.3 (red line). Photon bunching and super-Poissonian light statistics are observed on the timescale of $1/2\kappa$. Here, the main contribution comes from $\rho_{11}$. In addition, the oscillation of the coherence terms $\rho_{12}$ and $\rho_{21}$ leads to an oscillation of $g^{(2)}(\tau)$, on a timescale given by $1/2\Delta_1$. To demonstrate the effect of the quantum beat, the red dashed line shows $g^{(2)}(\tau)$ when the coherence terms $\rho_{12}(\tau)$ and $\rho_{21}(\tau)$ are neglected. Here, $g^{(2)}(\tau)$ still shows photon bunching as before, but without fast oscillations.
To prove the accuracy of the derived model the results for $g^{(2)}(\tau)$ are compared with the numerical solution of the master equation (black line). In order to compensate for the perturbative frequency shift, which is not included in the theory, the driving field strength is adjusted via

$$\varepsilon' = \sqrt{\varepsilon^2 + \frac{g}{3}\Delta\Omega_1 + \frac{g}{3}\Delta\Omega_2}\,. \tag{7.32}$$

Here, for a detuning of $\Delta_{df} = 5$ MHz from the two-photon resonance, the agreement is good. However, a further detuning leads to a decreased visibility

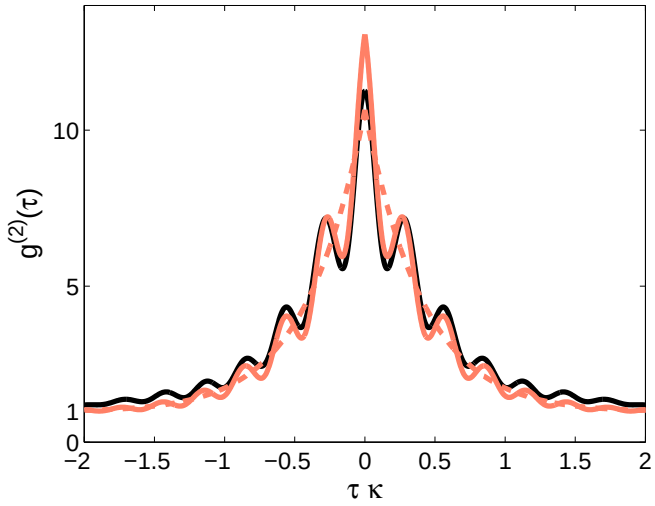


**Figure 7.3:** Comparison of the analytical model with the numerical solution. $g^{(2)}(\tau)$ obtained from the analytical description (red solid line) shows good agreement with the numerical solution (black line) when $\Delta_{ac}$ is sufficiently small (here $\Delta_{ac}/2\pi = 5$ MHz). All other parameters are $(\kappa, \gamma, g, \Delta_{a0}, S)/2\pi = (1.25, 2.99, 13.3, 35, 30)$ MHz and $\varepsilon_{df} = \sqrt{1.5/0.9}\kappa$, matching the experiment. The driving field is adjusted to compensate for the level shifts, see text. In addition, a scaling of the driving field by 0.9 includes further level shifts deviating from those found in [Sha10]. The quantum beat due to the superposition of $|1\rangle$ and $|2\rangle$ is switched off in the red dashed line to demonstrate the effect. As predicted by Eq. (7.31), $g^{(2)}(\tau)$ oscillates twice as fast as the coherence term $\rho_{21}$.

of the beat oscillation in the analytical model deviating from the numerical solution.

In summary, the analytical result agrees with the numerical calculations for a sufficiently low atom-cavity detuning of a few MHz. A large detuning causes a decrease of the product $A * B$ in Eq. (7.31) leading to a drop of the visibility of the interference fringes for the analytical model. We have proven that the analytical formula delivers good results within a few MHz of detuning of the driving laser, from the 2-photon resonance. If the detuning is too large the change of the perturbative frequency shifts becomes significant. Here the frequency shifts are fixed to the case of beeing on resonance with the 2-photon state. In the following we compare the experimental results, which are obtained for a large atom-cavity detuning, with the exact numerical solution.

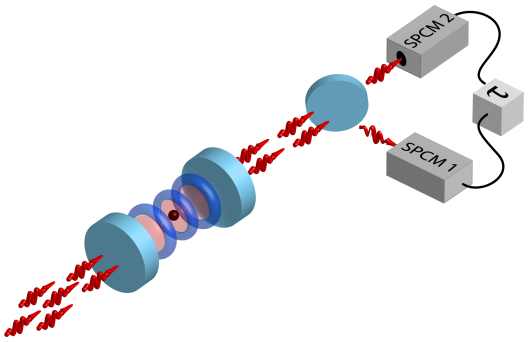


**Figure 7.4:** Hanbury Brown and Twiss Setup to measure second-order intensity correlations. The transmission of the near-resonant probe light (red arrows) through the coupled atom-cavity system is detected with two single-photon counting modules (SPCM1, SPCM2) in Hanbury Brown and Twiss configuration.

## 7.3 Two-photon gateway and quantum beat of superposition states

To get experimental access to the discussed phenomena of the previous section we perform second-order intensity correlations (see Sec. 3.2.2). The Hanbury Brown and Twiss setup is sketched in Fig. 7.4. Two measurements are performed with the parameters given in Tab. 7.1. The moderate atom-cavity detuning allows the two-photon resonance to be well separated from the normal modes, while still keeping the excitation of the two-photon resonance strong. In addition, the detuning increases the splitting between $|1\rangle$ and $|2\rangle$ and thus the frequency of the quantum beat. Therefore we operate in a promising regime to explore not only enhanced photon-pair emission but also the quantum beat. The system is continuously driven on resonance with $|3\rangle$ and the resonance condition

$$(n+1)\Delta_c = \frac{1}{2}(\Delta_c - \Delta_a) \pm \frac{1}{2}\sqrt{4g^2(n+1) + (\Delta_a - \Delta_c)^2} \tag{7.33}$$

is fulfilled within 1 MHz, corresponding to the fluctuations of the system. The main difference between the two measurements is the improved detection efficiency in parameter set (ii) due to the changed detection scheme as described in Sec. 3.1.5. The experimental photon coinidence rate is mainly limited by the atomic storage times and by the overall photon detection efficiency.
First, in Sec. 7.3.1 photon bunching is explored before the quantum beat of the superposition state of $|1\rangle$ and $|2\rangle$ is investigated in Sec. 7.3.2. To adapt the theoretically derived $g^{(2)}(\tau)$ to the experiment it is integrated within a given time window $\Delta\tau$ like in the experiment. For the experimental coincidence count rate we account for mirror transmission, losses, and detection efficiency.

| Parameter set | (i) | (ii) |
|---|---|---|
| overall photon detection efficiency | 6.7% | 14% |
| dipole trap (red (nW) / torus (nW)) | 170 nW / 250 nW | 170 nW |
| $g/2\pi$ (MHz) | 11.5 | 13.28 |
| $\Delta_{ac}/2\pi$ (MHz) | $-8.5$ | $-12.5$ |
| $\Delta_c/2\pi$ (MHz) (on resonance with $\|2,-\rangle$) | 10 | 12 |
| length of probing interval | $100\,\mu$s | $200\,\mu$s |

**Table 7.1:** Parameters for two different correlation measurements. (i) The first measurements were obtained with a lower detection efficiency. (ii) After improving the detection efficiency the measurements were repeated. The effective coupling strength as well as the effective atom-cavity detuning relies on the limits imposed by the postselection.

### 7.3.1 Photon bunching and the two-photon gateway

To obtain good statistics, we evaluate $g^{(2)}(\tau)$ for both measurements with a long time binning of $\Delta\tau = 170$ ns, which is equivalent to $\kappa$. Figure 7.5 a), shows two measurements of $g^{(2)}(\tau)$ on resonance with the two-photon state. The dark blue data is obtained with parameter set (i) and the blue data with set (ii). The blue data shows an improved signal-to-noise not only due to the enhanced detection efficiency, but also due to a longer probing interval ($200\,\mu$s instead of $100\,\mu$s). The bunching peak reaches in both cases $g^{(2)}(0) \approx 15$. This directly shows that photon bunching is insensitive to the detection efficiency. Both data sets are restricted to 0.04 of the empty cavity transmission to ensure strong coupling.
The numerical solution of the master equation (black line) with a coupling strength of $0.83 \times g_0$ shows very good agreement with the experiment, as depicted in Fig. 7.5 b). Here, no free fit parameter is used.

### 7.3.2 Quantum beat of superposition states

To be able to resolve the fast oscillations of the quantum beat we evaluate the data set (ii) with a reduced time binning. The fast changes in the coincidence rate require a time binning of only $\Delta\tau = 10$ ns. Considering low count rates, which are typically 0.013 photons/$\mu$s for very well coupled atoms, results in very long measurement times. However, Fig. 7.6 a) indicates oscillations of the number of coincidences on top of the photon bunching peak on timescales of $\approx 15$ ns. The number of recorded coincidences are shown for different coupling

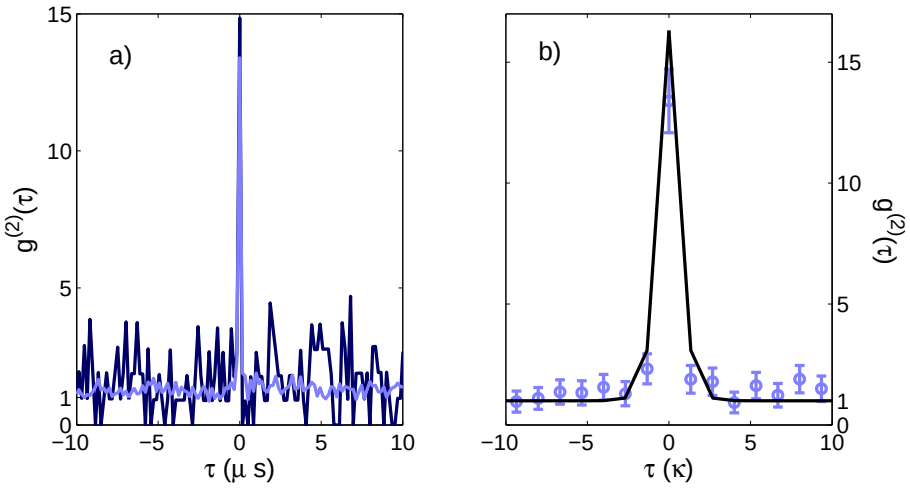


**Figure 7.5:** Photon bunching on the two-photon resonance. a) Two measurements with similar parameters, but different trapping schemes and detection efficiencies show the same photon bunching. It demonstrates the insensitivity of $g^{(2)}(\tau)$ to the detection efficiency as well as to slight changes in the experimental parameters. b) The numerical solution of the master equation (black line) shows good agreement with the experiment for a fixed coupling strength of $0.83 \times g_0$, which is justified due to the restrictive postselection in the measurement. The binning of the theory curve is done in the same way as in the experiment.

strengths. From dark to light blue the normalized transmission increases from 0.01, 0.02, 0.03 to 0.04.
Fig. 7.6 b) compares the experimentally obtained $g^2(\tau)$ (blue data) with the numerical solution (black curve).
The major results are:
1. The beat fringes from the quantum superposition of $|1\rangle$ and $|2\rangle$ are resolved. The frequency as well as the visibility of the oscillations agree with the numerical solution. Again, there are no free fitting parameters. The parameters are determined by the transmission spectrum (not shown).
2. Two photons emitted by the atom-cavity system are correlated within a time $\tau \leq 150$ ns with a HWHM $\approx$ 30 - 60 ns. This is compatible with the lifetime $\Gamma_-^{-1} \approx 33$ ns of state $|1,-\rangle$.
Comparing Fig. 7.5 and Fig. 7.6 shows that $g^2(0)$ depends on the chosen time binning. This effect is investigated in Fig. 7.7 a). The numerical simulations are binned with 10 ns (black, solid line) as well as 170 ns (grey, dashed line), corresponding to the two examples above. Due to the averaging over a large time window the bunching peak decreases from $g^2(0) = 44$ to $g^2(0) = 16$. Therefore the experiment underestimates the amount of photon bunching. A second effect under investigation is the atomic motion. In Fig. 7.7 b) the coupling strength is fixed to $0.83 \times g_0$ (black, dotted line). For the dark-grey,

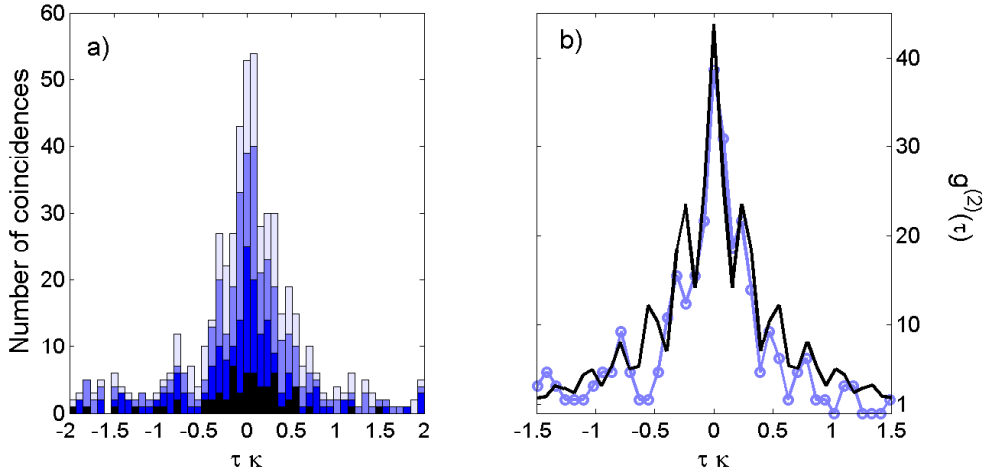


**Figure 7.6:** Quantum beat resolved in photon-photon correlation. a) The number of coincidences oscillates in time as a consequence of the quantum beat. Here, $g$ is restricted to 0.01, 0.02, 0.03 and 0.04 (from dark to light blue) of the empty cavity transmission. b) $g^{(2)}(\tau)$ obtained from the experiment (blue data) with a qualification of 0.02 of the empty cavity is compared with the result from numerical calculations with a fixed coupling strength of $0.83 \times g_0$ (black line). The parameters used are $\Delta_{a,0}/2\pi = 35$ MHz with a Stark shift of $S/2\pi = 22.5$ MHz and $E_{df} = 1.5/0.9\,\kappa$ with a probing on resonance with the 2-photon resonance. The increased Stark shift and localization compared to the fit for the transmission spectrum is justified by the stronger qualification. The numerical calculations are binned with 10 ns as in the experiment. Compared to Fig. 7.5 the bunching peak is higher due to the smaller time binning.

dashed line the coupling strength is distributed around the average coupling of $0.83 \times g_0$ with a Gaussian distribution between $0.7 \times g_0$ and $0.9 \times g_0$. For the light-grey, dotted line the coupling strength is distributed between 0.6 and $1 \times g_0$. A moving atom causes a reduced visibility of the beat fringes as well as a slight enhancement of the bunching peak.

## 7.4 Multiphotonic nature of the coupled system

Chapter 6 has disclosed the difficulties to observe higher-order resonances in transmission spectroscopy. Large experimental effort was necessary to isolate the two-photon resonances from the normal modes. Here, we investigate the possibility to use photon statistics to detect higher-order resonances. In particular, a new second-order correlation function, $C^{(2)}$, which is introduced in Sec. 7.4.1, allows to detect a two-photon resonances. The performed experiments in Sec. 7.4.2 measure the photon statistics depending on the probe frequency. Using $C^{(2)}$ the two-photon resonance is localized and the multi-

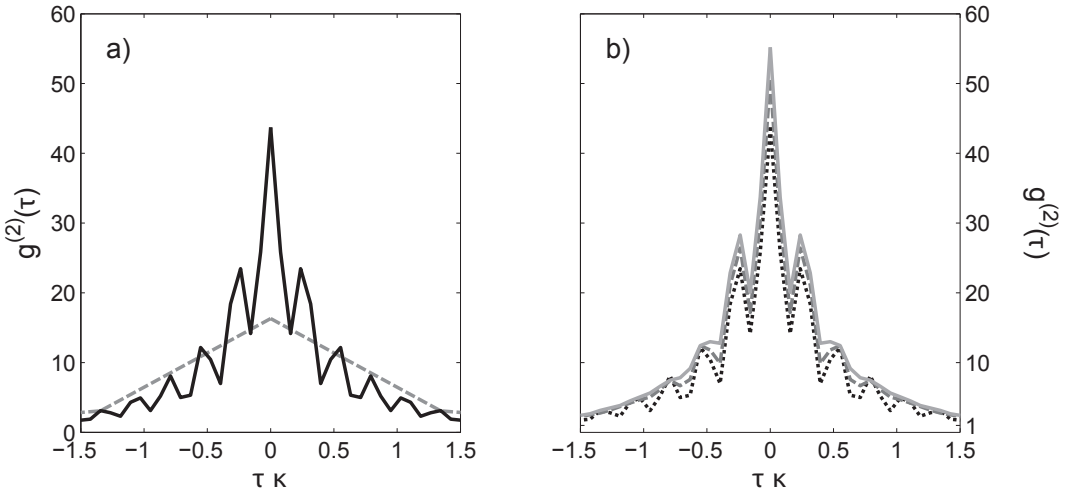


**Figure 7.7:** Effects of time binning and atomic motion on second-order correlations. a) A larger time binning leads to a reduced photon bunching at $\tau = 0$ due to the averaging. Here, $g^{(2)}(0)$ reduces from 44, for a binning of 10 ns (black, solid line) to 16 for a binning of 170 ns (grey, dashed line). b) The motion of the atom leads to a reduced visibility of the beat fringes. The black, dotted line is obtained for a fixed coupling of $0.83 \times g_0$, the dark-grey, dashed line for an coupling strength varying between $0.7 \times g_0$ and $0.9 \times g_0$ with a Gaussian distribution around $0.83 \times g_0$. The light-grey, solid line includes a coupling strength between $0.6 \times g_0$ and $1 \times g_0$ around $0.83 \times g_0$. Although the effective coupling strength remains unchanged the visibility of the fringes clearly disappears especially for longer correlation times.

photon nature of the atom-cavity system is demonstrated.

### 7.4.1 Theory of correlation functions

Second-order correlations should not be sensitive to single-photon events and therefore be a good detector for multi-photon processes. In principle, $g^{(2)}(\tau)$ allows one to localize multi-photon resonances, as these should present strong photon-photon correlations. However, a more appropriate choice for our purpose is the differential correlation function, $C^{(2)}(\tau)$, which at $\tau = 0$ reads

$$C^{(2)}(0) = \langle a^{\dagger 2} a^2 \rangle - \langle a^\dagger a \rangle^2 . \tag{7.34}$$

In the limit of weak input fields $C^{(2)}(\tau)$ scales as the square of the input intensity. The analogy between $C^{(2)}(0)$ and $g^{(2)}(0)$ is given in Tab. 7.2. The advantage of $C^{(2)}(\tau)$ is the reduced sensitivity to single-photon excitations compared to $g^{(2)}(\tau)$. Therefore, $C^{(2)}(\tau)$ provides a clearer measure of the probability to create two photons at once in the cavity.
To illustrate this point, Fig. 7.8 shows both correlation functions depending on

| | $C^{(2)}(0)$ | $g^{(2)}(0)$ |
|---|---|---|
| coherent intracavity field | 0 | 1 |
| maximally sub-Poissonian light | minimum negative value $-\langle a^\dagger a\rangle^2$ | 0 |
| super-Poissonian emission | $> 0$ | $> 1$ |

**Table 7.2:** Analogy between $C^{(2)}(0)$ and $g^{(2)}(0)$.

the detuning $\Delta_c$. We assume the atomic frequency to be equal to the cavity frequency, i.e., $\omega_a = \omega_c$. All other parameters are adapted to the experiment. As a result, the transmission (black line) shows two symmetric narrow peaks at the frequency of the normal modes, $|1, \mp\rangle$. Small shoulders indicate the two-photon states, $|2, \mp\rangle$, that only marginally contribute to the photon number for these frequency parameters and weak input intensity. In this regime, the mean photon number squared gives the probability of preparing two single photons independently, $\langle a^\dagger a\rangle^2 = [P(g,1)]^2$, where $P(g,1)$ is the probability of having one photon in the cavity and the atom in its internal ground state $|g\rangle$. For the same parameters, the normalized correlation function $g^{(2)}(0)$ (red line) presents tiny shoulders near the frequencies of the second dressed states. Here, the probability $P(g,2)$ to be in state $|g,2\rangle$ is maximized. However, as there is a much higher maximum at the center [Car91], $\Delta_c = 0$, precisely where the occupation probability $P(g,2)$ has a minimum, these shoulders are only visible in an enlarged version (red dashed line). This happens because for $\Delta_c = 0$ the probability of having uncorrelated photons is also small and, in fact, much smaller than $P(g,2)$. The height of this central peak, scaling as $g^4/\gamma^4$ for $g \gg 2\gamma$, dominates the frequency dependence of $g^{(2)}(0)$ and could overlap with the second dressed-state resonances, which can be washed out by extra broadening mechanisms.
The situation is more favorable when using the differential correlation function (blue line), which at weak fields reads $C^{(2)}(0) \approx 2P(g,2) - [P(g,1)]^2$. The maxima appear clearly at the detunings $\Delta_c = \mp g/\sqrt{2}$ of the second dressed states $|2, \pm\rangle$, owing to $2P(g,2) \gg [P(g,1)]^2$, whereas $C^{(2)}(0)$ has a minimum for $\Delta_c = 0$ because it is the difference of small probabilities. Away from these resonances, one finds two minima on the normal modes $|1, \pm\rangle$ where the negative values of $C^{(2)}$ correspond to sub-Poissonian emission. This is also visible by a negative value of $g^{(2)}(0) - 1$, which can be seen in the dashed, red line.
The advantage of $C^{(2)}(0)$ becomes more pronounced when we include the motion of the atom by averaging over different $g$-values, noted as $g_{var}$. We normalize by $C^{(2)}(0) = \sum p_i C_i / \sum p_i$ and $g^{(2)}(0) - 1 = \sum p_i C_i / \sum p_i \langle a^\dagger a\rangle^2$, where

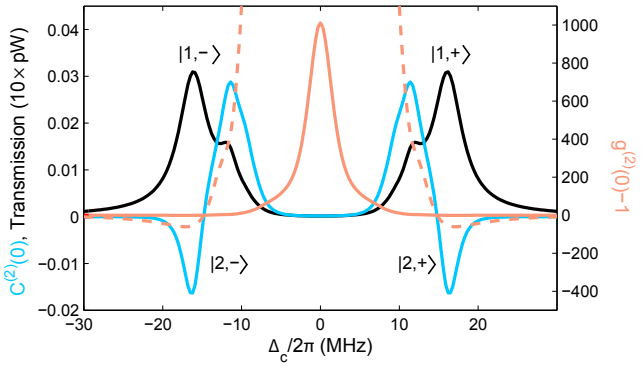


**Figure 7.8:** $C^{(2)}(0)$, $g^{(2)}(0)$ and the tranismission depending on the probe-cavity detuning. To see a pronounced effect everything is on resonance, $\omega_a = \omega_c$, and the coupling strength is assumed to be maximal for our setup $g/2\pi = g_0/2\pi = 16$ MHz. All other parameters are matched to the experiment. The black line is the transmitted photon rate (scaled by a factor of 10). It peaks when the highest photon flux is reached, namely on resonance with the normal modes $|1, \mp\rangle$ and a shoulder is visible on the two-photon resonance. $g^{(2)}(0)$ (red line) shows a large bunching peak at 0 due to the normalization to the photon flux. In a zoomed version (factor 100, red, dashed line) small shoulders on the two-photon resonance are visible. A more appropriate function is $C^{(2)}(0)$. As a differential correlation function it is not sensitive to the photon flux and therefore peaks on the two-photon resonance. It also shows a strong pronounced antibunching on the normal modes.

$p_i = e^{-(g_{var}-g_{eff})^2/\Delta g^2}$ follows from a Gaussian distribution, with $g_{eff}$ the effective coupling strength and $\Delta g$ the variation of $g$. Figure 7.9 a) shows that a small variation in g, namely from $0.8 \times g_0$ to $g_0$ with an effective coupling of $0.9 \times g_0$, is sufficient to make the two-photon peak vanish in the transmission signal as it is blurred by the normal mode. In contrast, it is still nicely visible in $C^{(2)}(0)$. Even for large variations from $0.4 \times g_0$ to $g_0$ it is still pronounced in $C^{(2)}(0)$, while the two-photon resonance moves towards smaller detunings due to the reduced average coupling strength of $0.7 \times g_0$ (see Figure 7.9 b)).

### 7.4.2 Correlations depending on the probe frequency

Fig. 7.10 shows the experimentally obtained $C^{(2)}(\tau)$ as a function of the delay time $\tau$ and for different probe-cavity detunings. We determine $C^{(2)}(\tau)$ in the same way as $g^{(2)}(\tau)$ but instead of normalizing to the intensity we subtract the averaged coincidence counts obtained for very long time delays ($\tau \gg 10\kappa^{-1}$) when the photons are uncorrelated. The size of the coincidence window is set to $\Delta\tau = 170$ ns $\approx 2\kappa^{-1}$.
On the cavity resonance, $\Delta_c = 0$, (Fig. 7.10 a)) the photon statistics are dominated by the effect of the atomic motion, where we observe a large bunching with long-period oscillations at the characteristic axial trapping period of $2.2\mu$s

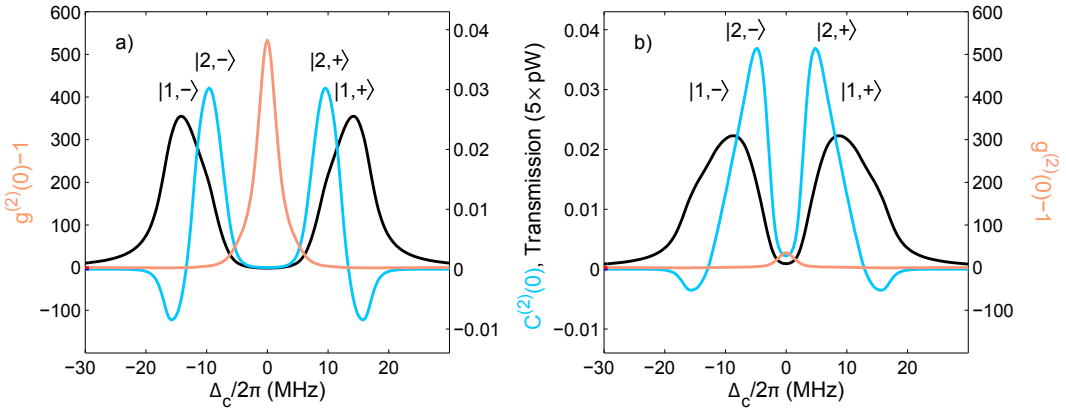


**Figure 7.9:** $C^{(2)}(0)$, $g^{(2)}(0)$ and the transmission depending on the probe-cavity detuning for different variations in the coupling strength. a) Only a small variation in the coupling strength, from $0.8 \times g_0$ to $g_0$ with an effective coupling of $0.9 \times g_0$, is sufficient to blur the two-photon peak in transmission. However, $C^{(2)}(0)$ still nicely resolves the resonance. b) Even for very large fluctuations from $0.4 \times g_0$ to $g_0$ the two-photon resonance is resolved with $C^{(2)}(0)$. Here, the peak moved towards a lower average coupling strength of $0.7 \times g_0$.

(see Chap. 4). This phenomenon rapidly disappears when the probe frequency is detuned with respect to the cavity frequency. In this case small variations in the coupling have little effect on the emitted light. This is already largely the case at $\Delta_c/2\pi = -3$ MHz, (Fig. 7.10 b)), where we observe no oscillations for times greater than $\kappa^{-1}$. Here we find small values of $C^{(2)}(0)$, which is expected from quantum theory as one is away from any resonance of the coupled atom-cavity system. As we sweep the laser frequency further away from the cavity, however, we find bunching and super-Poissonian statistics (Fig. 7.10 c)) precisely at the two-photon resonance $|2,-\rangle$. Figure 7.10 d) shows data registered when we excite the dressed state $|1,-\rangle$ on resonance. The photons are now essentially uncorrelated. This is also consistent with theory, which predicts an antibunching [Bir05], [Day08] too small to be observed with our cavity parameters.

Even though classical fields can produce photon bunching, the presented frequency dependence of the photon correlations shows a resonance at the two-photon dressed states, which has no classical analogue [Car96]. We have consequently sampled the spectrum every megahertz across the normal mode $|1,-\rangle$ and across the two-photon dressed state $|2,-\rangle$. For the measurement, about 20000 atoms were trapped in 127 hours of pure measurement time. Each trapped atom starts a measurement sequence including 31 probing intervals. About 7% of these intervals survived the selection procedure, which gives an effective probing time of 4 seconds. Figure 7.11 shows $C^{(2)}(0)$ as a function of the cavity detuning. We observe a resonance over a frequency range $\approx 2\pi \times 6$ MHz with a peak center on the two-photon state. The theoretical $C^{(2)}(\tau)$ is obtained

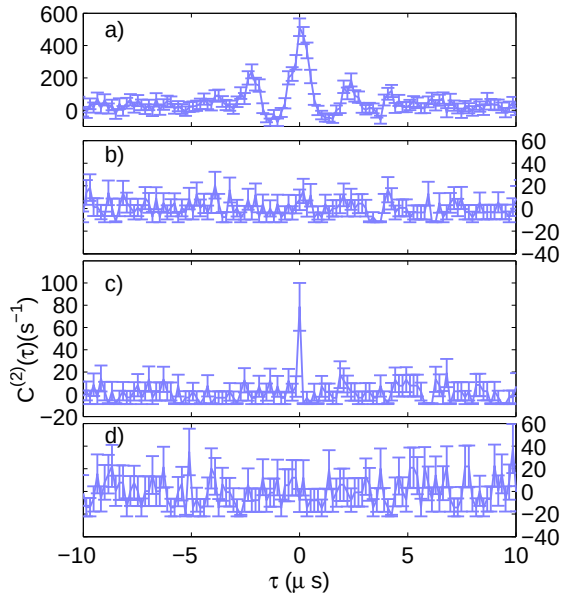


**Figure 7.10:** $C^{(2)}(\tau)$ for different probe-cavity detunings. From a) to d) the detunings change as $\Delta_c/2\pi = (0, -3, -10, -18)$ MHz. On resonance with the empty cavity the effect of the atomic motion is dominant. From b) to d) this effect is suppressed in the correlations. While b) and d) shows mainly uncorrelated photons, c) shows evidence of photon bunching due to the excitation of the two-photon resonance.

for a fixed coupling strength of $0.72 \times g_0$ integrated within a time window $\Delta\tau$ (blue, dashed line). It is then compared to the experimental coincidence count rate after accounting for mirror transmission, losses, and detection efficiency. Experiment and theory show an overall satisfactory agreement with a more pronounced antibunching in theory. The discrepancy can be explained by the atomic motion. When accounting for the atomic motion by a variation in $g$ between $0.62 \times g_0$ and $0.72 \times g_0$ the antibunching decreases and the peak shifts due to the reduced coupling strength (blue, solid line).
A remarkable feature of the atom-cavity system is its ability to react differently depending on whether it is excited by single photons or a pair of photons. This is striking when comparing the rate of coincidences (blue data) to the photon count rate (dashed black line). The photon coincidence rate is higher on the second dressed state $|2, -\rangle$ than on the first one, whereas the photon count rate is highest on $|1, -\rangle$. This asymmetry is a manifestation of the anharmonicity of the system owing to its discrete multi-photon nature.

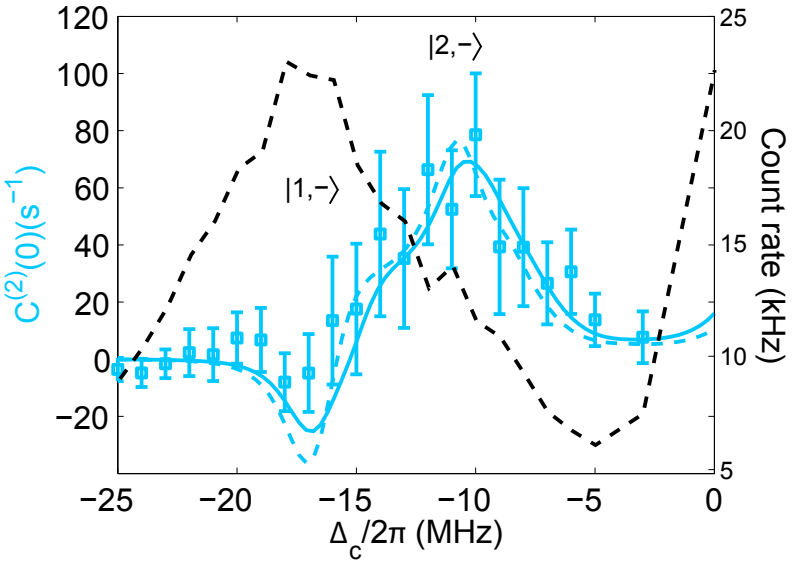


**Figure 7.11:** The multi-photon nature of the coupled atom-cavity system. The black dashed line is the experimentally measured transmitted intensity (corresponding to the right axis) with a peak on the normal mode $|1,-\rangle$. The blue data points are measured $C^{(2)}(0)$ with a peak on the two-photon resonance $|2,-\rangle$. The dashed blue line is obtained from the numerical solution with a fixed coupling strength of $0.72 \times g_0$. Only a minor atomic motion corresponding to a variation in $g$ between $0.62 \times g_0$ and $0.72 \times g_0$ changes $C^{(2)}(0)$ (blue, solid line). The peak broadens and shifts towards $\Delta_c = 0$, but the peak itself remains. The numerical solution is also double-checked with the fixed-atom theory in the weak intensity limit, as discussed in [Bre99, Car91].

## 7.5 Summary

In summary, we addressed the question whether a single atom can simultaneously absorb and emit two resonant photons. Such an effect could allow interactions between two photons mediated by one atom. We investigated the coupled atom-cavity system serving as a two-photon gateway which favors the transmission of photon pairs through the cavity. The fingerprint left by the atom transforms coherent laser light into strongly bunched, super-Poissonian light. The number of coincidences is enhanced in this frequency region, with a coincidence count rate of more than 80 per second of probing time. Compared to a coherent field of the same intensity the number of coincidences is enhanced by a factor of $\approx 40$. The observed feature of photon bunching is very narrow in the time domain, and broad in the frequency domain.
By including more detectors this technique can be extended to higher-order correlation functions. At higher excitation power this should allow one to observe higher-order dressed states. The number of detectors thus corresponds

to the number of resolvable photons.
With a larger atom-cavity coupling, this should open new perspectives for using single atoms in controlled photonic quantum gates and might be exploited for quantum communication.

# 8 Summary and outlook

This thesis reported on the most recent progress in the control of a single atom within an intracavity dipole trap. In particular, a new control scheme based on feedback is established where the dipole potential is altered depending on the atom's current position. The feedback acts in real time, within a fraction of one oscillation period of the atom in the trap. Such a fast reaction facilitates a (quasi-) continuous observation and action on the atomic position where each detected photon gives additional information of the atomic trajectory. In the future, such a feedback technique could allow one to control and steer the atomic trajectory at will. The precision of the control is limited by the discrete photon-character of the probe light and, ultimately, by Heisenberg's uncertainty principle for the position and momentum measurement.
The feedback technique controls the atom in the transverse direction of the beam propagation. It relies on the ability to observe and to actuate on a single particle and is, in principle, applicable to other systems. Possible implementations include the precise positioning of quantum emitters, like neutral atoms, ions, or molecules, in systems with limited optical access. In particular, new types of microcavities are designed to enable a strong coupling of quantum emitters to extremely small mode volumes. Prominent examples are optical fiber cavities on a chip [Geh10], membrane-type structures of planar photonic crystal cavities [Eng10], 'zipper' photonic crystal cavities [Cha09], bottle resonators [Pol09], microtoroidal resonators [Day08] or on-chip superconducting microwave resonators [Sch09]. The cavity could be used as a microscope to localize the quantum emitter within the cavity mode and the feedback could be actuated via optical, electrical or magnetic forces.
In this thesis the feedback technique was also investigated in terms of a new cooling technique with the focus on improving the atomic storage times for reasonably high probe power. Improved storage times, better localization of the atom within the cavity mode and first measurements of feedback cooling already demonstrate the power of this technique to control a single atom. However, the present setup imposes limits on the efficiency of the feedback. Further improvements of the setup and the algorithm could establish feedback as a cooling technique with storage times longer than a second.
In addition to feedback control, this thesis reported on the investigation of a two-photon resonance. The anharmonic energy level structure of the coupled system allows for the selective excitation of higher-order dressed states. The exclusive addressability of the two-photon resonance results in photon statis-

tics of the transmitted light that show photon bunching and super-Poissonian fluctuations, indicating the transmission of photon pairs. The coupled system thereby acts as a gateway for photon pairs. The response of the system with respect to the intensity of the driving laser shows a quantum nonlinearity, introducing nonlinear optics on the single-atom few-photon level.
Such a nonlinearity is an essential component for new investigations. For example, it could lead to quadrature squeezing mediated by a single atom. To observe squeezing a homodyne detection setup needs to be added to the present setup measuring the field emitted by the cavity. Further applications, arising from the two-photon resonance, include single-photon switches or single-photon transistors. The experiments presented in this thesis are first steps towards such applications.
One approach to realize such applications is to imitate atomic systems with solid-state based devices. For example, first cQED experiments are currently performed with nitrogen-vacancy (NV) centers in diamond coupled to the evanescent field of a photonic crystal cavity [Eng10]. Other solid-state based cQED devices, like quantum dots coupled to the mode of a semiconductor cavity, have already reached the strong-coupling regime, demonstrating the normal mode splitting [Rei04, Yos04, Pet05]. Both systems can potentially observe higher-order resonances. The interest in the higher-order dressed states goes beyond the atomic physics community as is demonstrated in [Joh06, Fin08]. Here, the higher-order resonances are observed within the field of circuit QED [Cla08] operating in the microwave domain.
On one hand, the solid-state based experiments are potentially scalable and could be integrated into applications. On the other hand, the solid-state based devices do not provide such a clean system as atomic systems. In these systems the parameters, like the transition frequencies or the coupling strengths between the quantum emitter and the cavity, are determined by the fabrication process of the device and are difficult to control. The coupling to the environment is defined by the surrounding solid state matrix instead of the continuous vacuum modes. In contrast, the atomic transition frequencies are so reproducible in isolation that they serve as atomic clocks. It is the purity of atomic systems which makes them an ideal model system to study matter-light interaction at a fundamental level.

# Bibliography


[Als92] P. Alsing, D.-S. Guo, and H. J. Carmichael. Dynamic Stark effect for the Jaynes-Cummings system. *Phys. Rev. A* **45**, 5135 (1992).

[Ass09] M. Assmann, F. Veit, M. Bayer, M. van der Poel, and J. M. Hvam. Higher-order photon bunching in a semiconductor microcavity. *Science* **325** (2009).

[Ber94] P. R. Berman (Editor) Cavity quantum electrodynamics. Advances in atomic, molecular, and optical physics, New York: Academic Press (1994).

[Ber06] P. Bermel, A. Rodriguez, S. G. Johnson, J. D. Joannopoulos, and M. Soljacic. Single-photon all-optical switching using waveguide-cavity quantum electrodynamics. *Phys. Rev. A* (2006).

[Bir05] K. M. Birnbaum, A. Boca, R. Miller, A. D. Boozer, T. E. Northup, and H. J. Kimble. Photon blockade in an optical cavity with one trapped atom. *Nature* **436**, 87 (2005).

[Boc04] A. Boca, R. Miller, K. M. Birnbaum, A. D. Boozer, J. McKeever, and H. J. Kimble. Observation of the vacuum rabi spectrum for one trapped atom. *Phys. Rev. Lett.* **93**, 233603 (2004).

[Boo06] A. D. Boozer, A. Boca, R. Miller, T. E. Northup, and H. J. Kimble. Cooling to the Ground State of Axial Motion for One Atom Strongly Coupled to an Optical Cavity. *Phys. Rev. Lett.* **97**(4), 083602 (2006).

[Bre99] R. J. Brecha, P. R. Rice, and M. Xiao. $n$ two-level atoms in a driven optical cavity: Quantum dynamics of forward photon scattering for weak incident fields. *Phys. Rev. A* **59**(3), 2392 (1999).

[Bri93] H.-J. Briegel and B.-G. Englert. Quantum optical master equations: The use of damping bases. *Phys. Rev. A* **47**, 3311 (1993).

[Bru96] M. Brune, F. Schmidt-Kaler, A. Maali, J. Dreyer, E. Hagley, J. M. Raimond, and S. Haroche. Quantum rabi oscillation: A direct test of field quantization in a cavity. *Phys. Rev. Lett.* **76**(11), 1800 (1996).

[Bus06] P. Bushev, D. Rotter, A. Wilson, F. Dubin, C. Becher, J. Eschner, R. Blatt, V. Steixner, P. Rabl, and P. Zoller. Feedback Cooling of a Single Trapped Ion. *Phys. Rev. Lett.* **96**(4), 043003 (2006).

[Car91] H. J. Carmichael, R. J. Brecha, and P. R. Rice. Quantum interference and collapse of the wavefunction in cavity QED. *Opt. Comm.* **82**, 73 (1991).

[Car93] H. Carmichael. An Open Systems Approach to Quantum Optics. Springer-Verlag, Berlin (1993).

[Car96] H. J. Carmichael, P. Kochan, and B. C. Sanders. Photon Correlation Spectroscopy. *Phys. Rev. Lett.* **77**, 631 (1996).

[Car99] H. Carmichael. Statistical Methods in Quantum Optics 1: Master Equations and Fokker-Planck Equations. Springer-Verlag, Berlin (1999).

[Cha07] D. E. Chang, A. S. Sørensen, E. A. Demler, and M. D. Lukin. A single-photon transistor using nano-scale surface plasmons. *Nature Phys.* **3**, 807 (2007).

[Cha09] J. Chan, M. Eichenfield, R. Camacho, and O. Painter. Optical and mechanical design of a zipper photonic crystal optomechanical cavity. *Optics Express* **17**(5), 3802 (2009).

[Chi96] J. J. Childs, K. An, M. S. Otteson, R. R. Dasari, and M. S. Feld. Normal-mode line shapes for atoms in standing-wave optical resonators. *Phys. Rev. Lett.* **77**(14), 2901 (1996).

[Chu98] S. Chu. The manipulation of neutral particles. *Rev. Mod. Phys.* **70**, 685 (1998).

[Cla08] J. Clarke and F. K. Wilhelm. Superconducting quantum bits. *Nature* **453**, 1031 (2008).

[CT98] C. Cohen-Tannoudji. Manipulating atoms with photons. *Rev. Mod. Phys.* **70**, 707 (1998).

[Day08] B. Dayan, A. S. Parkins, T. Aoki, E. P. Ostby, K. J. Vahala, and H. J. Kimble. A Photon Turnstile Dynamically Regulated by One Atom. *Science* **319**(5866), 1062 (2008).

[Dot09] I. Dotsenko, M. Mirrahimi, M. Brune, S. Haroche, J. Raimond, and P. Rouchon. Quantum feedback by discrete quantum nondemolition measurements: Towards on-demand generation of photon-number states. *Phys. Rev. A* **80**(1), 013805 (2009).

[Ein05] A. Einstein. Über einen die Erzeugung und Verwandlung des Lichtes betreffenden heuristischen Gesichtspunkt. *Annalen der Physik* **322**, 132 (1905).

[Eng10] D. Englund, B. Shields, K. Rivoire, F. Hatami, J. Vuckovic, H. Park, and M. D. Lukin. Deterministic coupling of a single nitrogen vacancy center to a photonic crystal cavity. *ArXiv e-prints* (2010).

[Fin08] J. M. Fink, M. Göppl, M. Baur, R. Bianchetti, P. J. Leek, A. Blais, and A. Wallraff. Climbing the JaynesCummings ladder and observing its $\sqrt{n}$ nonlinearity in a cavity QED system. *Nature* **454**, 315 (2008).

[Fis02] T. Fischer, P. Maunz, P. W. H. Pinkse, T. Puppe, and G. Rempe. Feedback on the motion of a single atom in an optical cavity. *Phys. Rev. Lett.* **88**, 163002 (2002).

[For07] K. M. Fortier, S. Y. Kim, M. J. Gibbons, P. Ahmadi, and M. S. Chapman. Deterministic loading of individual atoms to a high-finesse optical cavity. *Phys. Rev. Lett.* **98**(23), 233601 (2007).

[Fos00a] G. T. Foster, S. L. Mielke, and L. A. Orozco. Intensity correlations in cavity QED. *Phys. Rev. A* **61**(5), 053821 (2000).

[Fos00b] G. T. Foster, L. A. Orozco, H. M. Castro-Beltran, and H. J. Carmichael. Quantum State Reduction and Conditional Time Evolution of Wave-Particle Correlations in Cavity QED. *Phys. Rev. Lett.* **85**, 3149 (2000).

[Fuh08] A. Fuhrmanek, Multiphoton transitions in a strongly-coupled atom-cavity system, Diplomarbeit, Max-Planck-Institut für Quantenoptik, Garching, and Technische Universität München (2008), unpublished.

[Geh10] R. Gehr, J. Volz, G. Dubois, T. Steinmetz, Y. Colombe, B. L. Lev, R. Long, J. Estve, and J. Reichel. Cavity-based single atom preparation and high-fidelity hyperfine state readout. *Phys. Rev. Lett.* **104**(4), 203602 (2010).

[Gle07] S. Gleyzes, S. Kuhr, C. Guerlin, J. Bernu, S. Deléglise, U. Busk Hoff, M. Brune, J.-M. Raimond, and S. Haroche. Quantum jumps of light recording the birth and death of a photon in a cavity. *Nature* **446**, 297 (2007).

[Got04] H. Goto and K. Ichimura. Expectation-value approach to photon statistics in cavity QED. *Phys. Rev. A* **70**(2), 023815 (2004).

[Gra04] P. Grangier. Focus on single photons on demand. *New J. Phys.* **6**(6) (2004).

[Gri97] J. Gripp, S. L. Mielke, and L. A. Orozco. Evolution of the vacuum Rabi peaks in a detuned atom-cavity system. *Phys. Rev. A* **56**, 3262 (1997).

[Gri99] R. Grimm and M. Weidemueller. Optical dipole traps for neutral atoms. *Elsevier Science* **42**, 95 (1999).

[Gue07] C. Guerlin, J. Bernu, S. Deléglise, C. Sayrin, S. Gleyzes, S. Kuhr, M. Brune, J.-M. Raimond, and S. Haroche. Progressive field-state collapse and quantum non-demolition photon counting. *Nature* **448**, 889 (2007).

[Hän75] T. W. Hänsch and A. L. Schawlow. Cooling of gasses by laser radiation. *Opt. Comm.* **13**, 68 (1975).

[Har06] S. Haroche and J. M. Raimond. Exploring the Quantum, Atoms, Cavities, and Photons. Oxford University Press, New York (2006).

[Hij07] M. Hijlkema, B. Weber, H. P. Specht, S. C. Webster, A. Kuhn, and G. Rempe. A single-photon server with just one atom. *Nature Phys.* **3**, 253 (2007).

[Hof08] M. Hofheinz, E. M. Weig, M. Ansmann, R. C. Bialczak, E. Lucero, M. Neeley, A. D. O'Connell, H. Wang, J. M. Martinis, and A. N. Cleland. Generation of Fock states in a superconducting quantum circuit. *Nature* **454**, 310 (2008).

[Hoo98] C. J. Hood, M. S. Chapman, T. W. Lynn, and H. J. Kimble. Real-Time Cavity QED with Single Atoms. *Phys. Rev. Lett.* **80**, 4157 (1998).

[Hoo00] C. J. Hood, T. W. Lynn, A. C. Doherty, A. S. Parkins, and H. J. Kimble. The atom-cavity microscope: Single atoms bound in orbit by single photons. *Science* **287**, 1447 (2000).

[Jay63] E. T. Jaynes and F. W. Cummings. Comparison of quantum and semiclassical radiation theories with application to the beam maser. *Proc. IEEE* **51**, 89 (1963).

[Joh06] J. Johansson, S. Saito, T. Meno, H. Nakano, M. Ueda, K. Semba, and H. Takayanagi. Vacuum rabi oscillations in a macroscopic superconducting qubit lc oscillator system. *Phys. Rev. Lett.* **96**(4), 127006 (2006).

[Kel04] M. Keller, B. Lange, K. Hayasaka, W. Lange, and H. Walther. Continuous generation of single photons with controlled waveform in an ion-trap cavity system. *Nature* **431**, 1075 (2004).

[Kim77] D. M. Kimble, H. J. and L. Mandel. Photon antibunching in resonance fluorescence. *Phys. Rev. Lett.* **39**, 691695 (1977).

[Kub08] A. Kubanek, A. Ourjoumtsev, I. Schuster, M. Koch, P. W. H. Pinkse, K. Murr, and G. Rempe. Two-photon gateway in one-atom cavity quantum electrodynamics. *Phys. Rev. Lett.* **101**(20), 203602 (2008).

[Kub09] A. Kubanek, M. Koch, C. Sames, A. Ourjoumtsev, P. W. H. Pinkse, K. Murr, and G. Rempe. Photon-by-photon feedback control of a single-atom trajectory. *Nature* **462**, 898 (2009).

[Kuh01] S. Kuhr, W. Alt, D. Schrader, M. Müller, V. Gomer, and D. Meschede. Deterministic Delivery of a Single Atom. *Science* **293**, 278 (2001).

[Kuh02] A. Kuhn, M. Hennrich, and G. Rempe. Deterministic Single-Photon Source for Distributed Quantum Networking. *Phys. Rev. Lett.* **89**(6), 067901 (2002).

[Lam47] W. Lamb and R. Retherford. Fine structure of the hydrogen atom by a microwave method. *Phys. Rev.* **72**, 241 (1947).

[Lyn05] T. W. Lynn, K. Birnbaum, and H. J. Kimble. Strategies for real-time position control of a single atom in cavity QED. *J. Opt. B* **7**, 215 (2005).

[Mai60] T. H. Maiman. Stimulated Optical Radiation in Ruby. *Nature* **187**, 493 (1960).

[Mau04] P. Maunz, T. Puppe, I. Schuster, N. Syassen, P. W. H. Pinkse, and G. Rempe. Cavity cooling of a single atom. *Nature (London)* **428**, 50 (2004).

[Mau05a] P. Maunz, Cavity cooling and spectroscopy of a bound atom-cavity system, Ph.D. thesis, Max-Planck-Institut für Quantenoptik, Garching, and Technische Universität München (2005).

[Mau05b] P. Maunz, T. Puppe, I. Schuster, N. Syassen, P. W. H. Pinkse, and G. Rempe. Normal-mode spectroscopy of a single-bound-atom-cavity system. *Phys. Rev. Lett.* **94**, 033002 (2005).

[McK03] J. McKeever, J. R. Buck, A. D. Boozer, A. Kuzmich, H.-C. Nägerl, D. M. Stamper-Kurn, and H. J. Kimble. State-insensitive cooling and trapping of single atoms in an optical cavity. *Phys. Rev. Lett.* **90**, 133602 (2003).

[McK04] J. McKeever, A. Boca, A. D. Boozer, R. Miller, J. R. Buck, A. Kuzmich, and H. J. Kimble. Deterministic Generation of Single Photons from One Atom Trapped in a Cavity. *Science* **303**, 1992 (2004).

[Mes85] D. Meschede, H. Walther, and G. Müller. One-atom maser. *Phys. Rev. Lett.* **54**(5), 551 (1985).

[MO05] M. M. Oxborrow and A. G. Sinclair. Single-photon sources. *Cont. Phys.* **46**, 173 (2005).

[Mün99a] P. Münstermann, T. Fischer, P. Maunz, P. W. H. Pinkse, and G. Rempe. Dynamics of Single-Atom Motion Observed in a High-Finesse Cavity. *Phys. Rev. Lett.* **82**(19), 3791 (1999).

[Mün99b] P. Münstermann, T. Fischer, P. W. H. Pinkse, and G. Rempe. Single slow atoms from an atomic fountain observed in a high-finesse optical cavity. *Opt. Comm.* **159**, 63 (1999).

[Mur03] K. Murr. On the suppression of the diffusion and the quantum nature of a cavity mode. optical bistability: forces and friction in driven cavities. *J. Phys. B* **36**, 2515 (2003).

[Mur06a] K. Murr. Large velocity capture range and low temperatures with cavities. *Phys. Rev. Lett.* **96**(25), 253001 (2006).

[Mur06b] K. Murr, P. Maunz, P. W. H. Pinkse, T. Puppe, I. Schuster, D. Vitali, and G. Rempe. Momentum diffusion for coupled atom-cavity oscillators. *Phys. Rev. A* **74**(4), 043412 (2006).

[Nog99] G. Nogues, A. Rauschenbeutel, S. Osnaghi, M. Brune, J. M. Raimond, and S. Haroche. Seeing a single photon without destroying it. *Nature* **400**, 239 (1999).

[Nus05] S. Nussmann, K. Murr, M. Hijlkema, B. Weber, A. Kuhn, and G. Rempe. Vacuum-stimulated cooling of single atoms in three dimensions. *Nature Phys.* **1**, 122 (2005).

[Pet05] E. Peter, P. Senellart, D. Martrou, A. Lemaitre, J. Hours, J. M. Gerard, and J. Bloch. Exciton-photon strong-coupling regime for a single quantum dot embedded in a microcavity. *Phys. Rev. Lett.* **95**(17), 067401 (2005).

[Phi98] W. D. Phillips. Laser cooling and trapping of neutral atoms. *Rev. Mod. Phys.* **70**, 721 (1998).

[Pin00] P. W. H. Pinkse, T. Fischer, P. Maunz, and G. Rempe. Trapping an atom with single photons. *Nature (London)* **404**, 365 (2000).

[Pla01] M. Planck. Über das Gesetz der Energieverteilung im Normalspektrum. *Annalen der Physik* **4**, 553 (1901).

[Pol09] M. Pollinger, D. O'Shea, F. Warken, and A. Rauschenbeutel. Ultrahigh-q tunable whispering-gallery-mode microresonator. *Phys. Rev. Lett.* **103**(3), 053901 (2009).

[Pup07a] T. Puppe, I. Schuster, A. Grothe, A. Kubanek, K. Murr, P. W. H. Pinkse, and G. Rempe. Trapping and observing single atoms in a blue-detuned intracavity dipole trap. *Phys. Rev. Lett.* **99**(1), 013002 (2007).

[Pup07b] T. A. Puppe, Trapping and observing single atoms in the dark, Ph.D. thesis, Max-Planck-Institut für Quantenoptik, Garching, and Technische Universität München (2007).

[Pur46] E. M. Purcell. Spontaneous emission probabilities at radio frequencies. *Phys. Rev.* **69**, 681 (1946).

[Rai01] J. M. Raimond, M. Brune, and S. Haroche. Manipulating quantum entanglement with atoms and photons in a cavity. *Rev. Mod. Phys.* **73**(3), 565 (2001).

[Reb99] S. Rebic, S. M. Tan, A. S. Parkins, and D. F. Walls. Large kerr nonlinearity with a single atom. *J. Opt. B: Quantum Semiclass. Opt.* **1**, 490 (1999).

[Rei04] J. P. Reithmaier, G. Sęk, A. Löffler, C. Hofmann, S. Kuhn, S. Reitzenstein, L. V. Keldysh, V. D. Kulakovskii, T. L. Reinecke, and A. Forchel. Strong coupling in a single quantum dot-semiconductor microcavity system. *Nature* **432**, 197 (2004).

[Rem87] G. Rempe, H. Walther, and N. Klein. Observation of quantum collapse and revival in a one-atom maser. *Phys. Rev. Lett.* **58**, 353 (1987).

[Rem91] G. Rempe, R. J. Thompson, R. J. Brecha, W. D. Lee, and H. J. Kimble. Optical bistability and photon statistics in cavity quantum electrodynamics. *Phys. Rev. Lett.* **67**, 1727 (1991).

[Sch52] E. Schrödinger. Are there quantum jumps? *Br. Jl. for Phil. Of Science* **3**, 109 (1952).

[Sch07] D. I. Schuster, A. A. Houck, J. A. Schreier, A. Wallraff, J. M. Gambetta, A. Blais, L. Frunzio, J. Majer, B. Johnson, M. H. Devoret, S. M. Girvin, and R. J. Schoelkopf. Resolving photon number states in a superconducting circuit. *Nature* **445**, 515 (2007).

[Sch08a] L. Schneebeli, M. Kira, and S. W. Koch. Characterization of strong light-matter coupling in semiconductor quantum-dot microcavities via photon-statistics spectroscopy. *Phys. Rev. Lett.* **101**(9), 097401 (2008).

[Sch08b] I. Schuster, Nonlinear spectroscopy of a single-atom-cavity system, Ph.D. thesis, Max-Planck-Institut für Quantenoptik, Garching, and Technische Universität München (2008).

[Sch08c] I. Schuster, A. Kubanek, A. Fuhrmanek, T. Puppe, P. W. H. Pinkse, K. Murr, and G. Rempe. Nonlinear spectroscopy of photons bound to one atom. *Nature Phys.* **4**, 382 (2008).

[Sch09] D. I. Schuster, L. S. Bishop, I. L. Chuang, D. DeMille, and R. J. Schoelkopf. Cavity QED in a molecular ion trap. *ArXiv e-prints* (2009).

[Sha10] S. Shamailov, A. Parkins, M. Collett, and H. Carmichael. Multiphoton blockade and dressing of the dressed states. *Optics Communications* **283**, 766 (2010).

[Ste04] D. A. Steck, K. Jacobs, H. Mabuchi, , T. Bhattacharya, and S. Habib. Quantum feedback control of atomic motion in an optical cavity. *Phys. Rev. Lett.* **92**(22), 223004 (2004).

[Ste06] D. A. Steck, K. Jacobs, H. Mabuchi, S. Habib, and T. Bhattacharya. Feedback cooling of atomic motion in cavity qed. *Phys. Rev. A* **74**(1), 012322 (2006).

[Tho92] R. J. Thompson, G. Rempe, and H. J. Kimble. Observation of normal-mode splitting for an atom in an optical cavity. *Phys. Rev. Lett.* **68**, 1132 (1992).

[Vah03] K. J. Vahala. Optical microcavities. *Nature* **424**, 839 (2003).

[vdM85] S. van der Meer. Stochastic cooling and the accumulation of antiprotons. *Rev. Mod. Phys.* **57**(3), 689 (1985).

[Wal06] H. Walther, B. T. H. Varcoe, B.-G. Englert, and T. Becker. Cavity quantum electrodynamics. *Rep. Prog. Phys.* **69**, 1325 (2006).

[Wer99] M. J. Werner and A. Imamoglu. Photon-photon interactions in cavity electromagnetically induced transparency. *Phys. Rev. A* **61**, 011801 (1999).

[Ye99] J. Ye, D. W. Vernooy, and H. J. Kimble. Trapping of single atoms in cavity qed. *Phys. Rev. Lett.* **83**, 4987 (1999).

[Yos04] T. Yoshie, A. Scherer, J. Hendrickson, G. Khitrova, H. M. Gibbs, G. Rupper, C. Ell, O. B. Shchekin, and D. G. Deppe. Vacuum Rabi splitting with a single quantum dot in a photonic crystal nanocavity. *Nature* **432**, 200 (2004).

[Zhu90] Y. Zhu, D. J. Gauthier, S. E. Morin, Q. Wu, H. J. Carmichael, and T. W. Mossberg. Vacuum Rabi splitting as a feature of linear-dispersion theory: Analysis and experimental observations. *Phys. Rev. Lett.* **64**, 2499 (1990).

# List of Publications

- **Feedback control of a single atom in an optical cavity**.
  A. Kubanek, M. Koch, C. Sames, A. Ourjoumtsev, T. Wilk, P. W. H. Pinkse, G. Rempe. *submitted to Applied Physics B.*

- **Observation of squeezed states of light from one atom excited with two photons**.
  A. Ourjoumtsev, A. Kubanek, M. Koch, C. Sames, P. W. H. Pinkse, G. Rempe and K. Murr. *In preparation.*

- **Feedback cooling of a single neutral atom**.
  M. Koch, C. Sames, A. Kubanek, M. Apel, M. Balbach, A. Ourjoumtsev, P. W. H. Pinkse, and G. Rempe. *Phys. Rev. Lett.* **105**, 173003 (2010).

- **Photon by photon feedback control of a single-atom trajectory**.
  A. Kubanek, M. Koch, C. Sames , A. Ourjoumtsev, P. W. H. Pinkse, K. Murr, and G. Rempe. *Nature* **462**, 898-901 (2009).

- **Two-photon gateway in one-atom cavity quantum electrodynamics**.
  A. Kubanek, A. Ourjoumtsev, I. Schuster, M. Koch, P. W. H. Pinkse, K. Murr, and G. Rempe. *Phys. Rev. Lett.* **101**, 2036602 (2008).

- **Nonlinear spectroscopy of photons bound to one atom**.
  I. Schuster, A. Kubanek, A. Fuhrmanek, T. Puppe, P. W. H. Pinkse, K. Murr, and G. Rempe. *Nature Physics* **4**, 382 (2008).

- **Trapping and observing single atoms in a blue-detuned intracavity dipole trap**.
  T. Puppe, I. Schuster, A. Grothe, A. Kubanek, K. Murr, P. W. H. Pinkse, and G. Rempe. *Phys. Rev. Lett.* **99**, 013002 (2007).

# Acknowledgement

Zum Schluß möchte ich all denjenigen meinen Dank aussprechen, die zum Gelingen dieser Arbeit beigetragen haben. Die Durchführung von Experimenten dieser Komplexität ist nur im Team und mit großem Engagement jedes einzelnen möglich. Ich hatte das Glück in einem Team arbeiten zu dürfen, das nicht nur fachlich außerordentlich kompetent ist, sondern auch ein angenehmes und freundschaftliches Arbeitsklima ermöglicht.
An erster Stelle möchte ich meinem Doktorvater Gerhard Rempe danken der mich in die Arbeitsgruppe aufgenommen hat und mir die Gelegenheit gegeben hat an diesem tollen Experiment mitzuwirken. In allen Phasen meiner Doktorarbeit konnte ich auf seine Unterstützung bauen.
Den Postdoktoranden Karim Murr, Alexei Ourjoumtsev, Pepijn Pinkse und Tatjana Wilk möchte ich für die Unterstützung in der Theorie, am Experiment sowie beim Schreiben dieser Arbeit danken.
Meinen Vorgängerdoktoranden Thomas Puppe und Ingrid Schuster möchte ich für die Einführung in das Experiment danken. Ihnen und meinen nachfolgende Doktoranden Markus Koch und Christian Sames danke ich für die gute Zusammenarbeit und den großen Einsatz.
Vielen Dank auch für das große Engagement der Diplomanden Johannes Almer, Andreas Fuhrmanek, Borys Hagemann, Matthias Apel und Maximilian Balbach.
Den Technikern Sepp Bayerl, Franz Denk, Helmuth Stehbeck und Tom Wiesmeier danke ich für ihre kompetente Hilfe bei technischen Herausforderungen am Experiment.
Einen herzlichen Dank an die gesamte Arbeitsgruppe für die hervorragende Stimmung innerhalb der Gruppe und den freundschaftlichen Umgang miteinander.
Bei QCCC möchte ich Thomas Schulte-Herbrüggen für sein großes Engagement danken und allen Doktoranden für die tolle Gruppendynamik und den gemeinsamen Gedankenaustausch. Vielen Dank an Rob für das Lesen meiner Arbeit. Außerdem möchte ich mich bei QCCC für das Ermöglichen meines Auslandsaufenthaltes in Neuseeland danken.
I would like to thank Howard Carmichael for supervising my research exchange at the University of Auckland. He introduced me to the theory of cavity QED and, in particular, to the analytical description of the two-photon resonance.
Meiner Familie, meiner Frau und meinen Freunden möchte ich für die rückhaltslose Unterstützung während der Doktorarbeit danken und die große Toleranz gegenüber der sehr zeitintensiven Arbeit.